Wide Band Gap Hybrid Lead Halide Perovskites for Tandem Solar Cells

Candidate Number: 1032368
Project Number: CMP31
Supervisors: Benjamin Putland, Dr Harry Sansom, Prof Henry Snaith

ABSTRACT

Metal halide perovskites are highly promising candidates for use as the wide-bandgap absorber in tandem solar cells, in part due to the ability to modify their bandgap energy through partial halide substitution. In this work, the hybrid lead halide perovskite $FA_{(1-x)}Cs_xPb[I_{(1-y)}Br_y]_3$ is investigated. The compositional region of $0.64 \lesssim y \lesssim 0.75$, $0 \lesssim x \lesssim 0.25$ is determined to have a bandgap energy of $E_g = 2.0 \pm 0.04$ eV, which is optimal for use as the wide-bandgap absorber in 2T and 3T tandem configurations. Photoinduced halide segregation, in which the well-mixed phase of $FA_{(1-x)}Cs_xPb[I_{(1-y)}Br_y]_3$ breaks down into I-rich and Br-rich regions, is observed across the 2 eV compositional region, with the rate of segregation observed to be lower for compositions with lower Br and higher Cs contents. Compositions in the 2 eV region are used to fabricate single-junction devices, with the best performing cell achieving a 9.53% power conversion efficiency with a 1.25 V open-circuit voltage and 11.6 mA cm^{-2} short circuit current, demonstrating the high potential of $FA_{(1-x)}Cs_xPb[I_{(1-y)}Br_y]_3$.

1. INTRODUCTION

Solar panels play a key role in the global transition to renewable, low-carbon energy sources. Crystalline silicon (c-Si) photovoltaics (PV) continue to be the dominant technology, with over 95% of the overall global PV market installed in 2020 being single-junction c-Si modules. The c-Si modules sold in 2021 are estimated to have an average power conversion efficiency (PCE) of 20% [1], with the PCE defined as the ratio of total incident solar power to output electrical power of the module. These modules are already heavily optimised and close to their practical maximum PCE [2][3], and so the cost increases significantly for higher efficiency modules due to the need for complex manufacturing methods: the highest efficiency (>22%) modules increase in cost by a factor between 2 to 3 [1]. The cost of solar power typically scales primarily with area rather than power output of the panel [2], so any technology that can surpass the PCE of single-junction c-Si cells has the potential to directly lower solar power production costs, accelerate the global shift towards renewable energy generation, and mitigate the effects of climate change.

1.1 Efficiency limit of single-junction solar cells: The Shockley-Queisser Model

In a single-junction solar cell, such as the ubiquitous c-Si module, an absorbing layer consisting of a semiconductor absorbs incoming photons, producing photogenerated electron-hole pairs. The electron-hole pairs are then separated by an internal electric potential, and the flow of charge carriers creates a current. The internal electric potential occurs due to the semiconductor forming a p-n junction, with one side of the semiconductor interfacing with electron donor atoms (n-junction) and electron acceptor atoms (p-junction). The Shockley-Queisser model [4], based on thermodynamic principles, describes the theoretical upper limit on the PCE of an ideal single-junction p-n solar cell. The calculations by Shockley and Queisser found a limiting efficiency η, known as the "detailed balance limit of efficiency". Three efficiency-limiting factors were considered: spectrum loss; recombination loss; and loss due to a non-rectangular I-V characteristic. Spectrum loss is caused by two competing processes: only photons with frequency $\nu \geq \nu_g = E_g/h$ can be absorbed by the semiconductor in the solar cell, however charge carriers generated by photons with $\nu > \nu_g$ rapidly relax to the band edge through collisions and lose any energy more than E_g; this is known as thermalisation. Here, h is the Planck constant and E_g is the minimum energy difference between the conduction and valence bands of the semiconductor in the solar cell, known as the "bandgap energy". Recombination loss occurs due to the recombination of photogenerated electron-hole pairs with resultant emission of photons, causing a loss of current. The non-rectangular I-V characteristic of a solar cell, which was modelled as an ideal diode by Shockley and Queisser, introduces further loss, as the maximum current density J_{sc} (the short circuit current density) and maximum voltage V_{oc} (the open circuit voltage) cannot be attained simultaneously; the "fill factor" is the ratio of the area of the J-V curve to the rectangular area of $J_{sc}V_{oc}$. A brief account of their derivation of this limit is presented in APPENDIX A.1. Shockley and Queisser approximated the solar spectrum to be that of a black body with surface temperature $T_s = 6000K$, and the PV was assumed to have

cell temperature $T_c = 300K$. The PCE limit for a single-junction c-Si PV, which has a bandgap of 1.1 eV was then found to be approximately 30%. Figure 1 shows the variation of PCE with bandgap, in a subsequent treatment of the Shockley-Queisser model with further refinements. These include the standard cell temperature of $T_c = 298.15$ K, and the standard solar spectrum AM 1.5G which takes into account absorption and scattering of light in the atmosphere. The full Bose-Einstein statistics of the emitted photon flux Q_C is also accounted for, rather than the Boltzmann approximation (Eqn [A.10]) that was used by Shockley and Quiesser. A more detailed treatment by Richter et al accounts for non-radiative recombination pathways such as the Auger effect, which do not vary with voltage according to Eqn [A.15]. For an undoped c-Si cell with thickness 110 μm, the PCE is found to be 29.4% [5]. For single junction c-Si cells in unconcentrated light, the PCE currently stands at 26.1% [3]. This is already near to the theoretical upper limit, and these higher efficiency cells are too expensive to be used commercially. Therefore, novel technologies are required to surpass the efficiencies of today's solar cells.

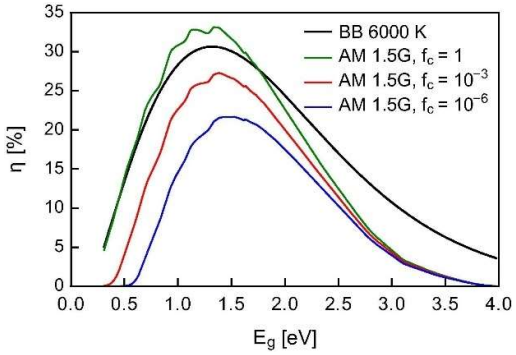


Figure 1: Shockley–Queisser limit. Operating Shockley–Queisser limit for a single-junction solar cell with cell temperature $T_c = 300K$ and blackbody solar spectrum with surface temperature $T_S = 6000K$ (in black) compared to efficiency limits for standard solar cell test conditions with different ratios f_c of non-radiative to radiative combination. Reproduced from REF [6].

1.2 Tandem Solar Cells

Tandem solar cell architectures are a promising technique to increase the efficiency of solar panels. In a tandem structure, light absorbers with increasing bandgap energies are stacked atop each other, so that the solar photons strike the widest bandgap absorber first. In a solar cell with a single absorber layer, the efficiency is limited in part by the spectrum loss described in section *(1.1)*. A tandem structure can mitigate this loss since the highest energy photons are captured by the widest bandgap absorber first with reduced thermalisation loss due to E_g being closer to those higher photon energies. This reduced thermalisation loss results in a higher voltage generated in the top cell. The lower energy photons pass through to the subsequent narrower bandgap absorber layers which capture the rest of the solar spectrum.

De Vos modelled the fundamental performance limit of a tandem structure [7], using the Shockley-Queisser theory to model each individual cell. A brief account of de Vos' model is presented in APPENDIX *A.2*. The original calculations by de Vos assumed a device temperature of $T_c = 300K$ and a solar spectrum equal to the blackbody spectrum at surface temperature $T_s = 6000K$. A maximum double-junction efficiency of $\eta = 42\%$ was predicted for cell bandgaps $E_{g1} = 1.0$ eV, $E_{g2} = 1.9$ eV. For a triple-junction structure, a maximum efficiency of $\eta = 49\%$ was predicted for cell bandgaps $E_{g1} = 0.8$ eV, $E_{g2} = 1.4$ eV, $E_{g3} = 2.3$ eV. The ideal efficiency of a stack with an infinite number of cells was predicted to have a maximum efficiency of $\eta = 68\%$.

Subsequent treatment by Eperon et. al. [2] accounted for the standard working conditions of $T_c = 298.15\,K$, AM 1.5G. They also considered the two possible double junction architectures, namely two-terminal (2T) and four-terminal (4T). Both architectures have benefits and drawbacks. In a 2T tandem architecture, the sub-cells are connected by a tunnel junction or recombination layer which charge carriers may travel across, so that there are only two electrical contacts to carry away the photogenerated current: one above the wide bandgap top sub-cell, and one below the narrow bandgap bottom sub-cell. In a 2T architecture, the sub-cells are thus electronically in series, and must obey Kirchhoff's laws, which means that the photocurrent in each sub-cell is limited by the lower sub-cell current; the currents in all sub-cells must thus be matched to obtain optimal power. The requirement of matching photocurrents at the maximum power point of each sub-cell leads to more stringent bandgap optimisation constraints. In 4T configurations, a transparent insulating gap separates the two sub cells. Each sub cell is separately connected to an external circuit and has its own two electrical contacts, so that the cells effectively work independently. The current-matching condition therefore does not apply to 4T architectures; this causes the efficiency to vary less sharply as a function of E_{g1}, E_{g2} for 4T tandem architectures, as illustrated in FIG 2a,b. The 4T architecture requires semi-transparent electrical contacts between sub-cells which will absorb some photons, reducing real world performance. However, processing the 2T cells is typically more challenging, as the deposition of upper layers can often damage underlying layers. Similar calculations by Eperon et. al. [2] for triple junction cells in three-terminal (3T) architecture predicted maximum PCEs of 47% and 49% using base absorbers with $E_{g1} = 1.22$ eV, 1.1 eV respectively. Therefore, tandem architectures theoretically promise to overcome the Shockley-Queisser efficiency

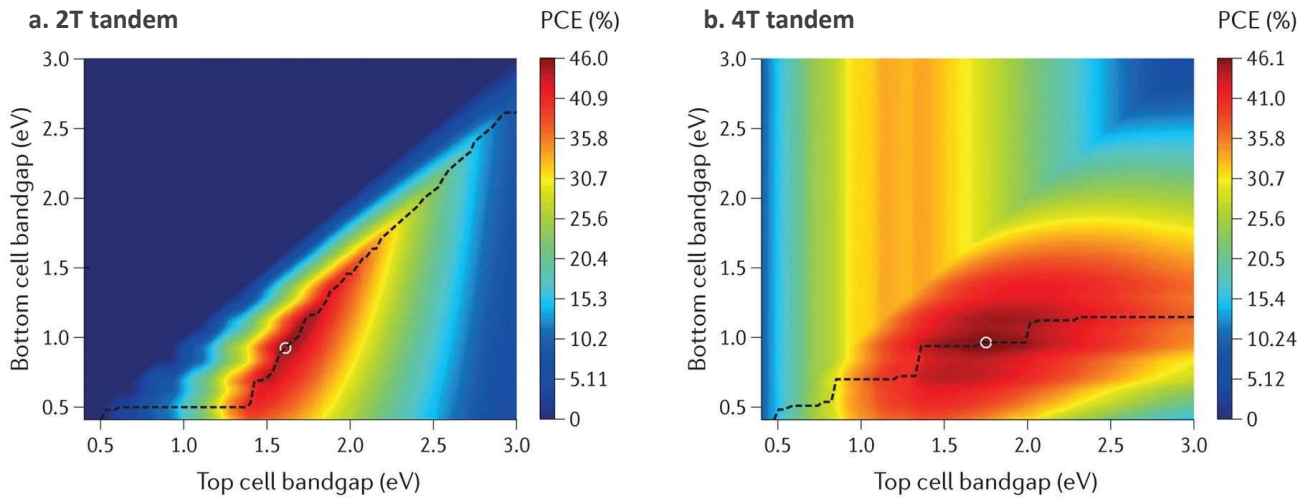


Figure 2: Maximum efficiency limits for tandem structures. Theoretical maximum PCE as a function of top and bottom cell bandgap energy for: (**a**) 2T double junction, (**b**) 4T double junction architectures. The dashed line traces peak efficiency for the displayed range of top and bottom bandgap energies. The white circles indicate maximum PCE. All figures are reproduced from ref [1].

limit on the conventional single-junction c-Si solar cells that currently dominate. The variation of maximum efficiency with E_{g1}, E_{g2} for 3T systems with each of these base absorbers is illustrated in APPENDIX *A*.3. The base absorber bandgaps for those triple junction structures are of interest as they have been attained using a narrow bandgap perovskite $FA_{0.75}C_{0.25}Pb_{0.5}Sn_{0.5}I_3$, as reported by Eperon et al [8], and c-Si, respectively. Therefore, APPENDIX A.3 illustrates the optimal bandgaps for potential all-perovskite and Si-perovskite triple junction solar cells. The use of perovskites in tandem cells is promising for a variety of reasons, which are outlined in the next section.

1.3 Perovskite Solar Cells

Organic-inorganic (hybrid) metal halide perovskites have gained attention in recent years for use as absorber in thin-film photovoltaics (PV). The hybrid metal halide perovskites relevant to PVs have a 3-dimensional ABX3 structure with corner-sharing $[BX_6]^{-4}$ octahedra, as illustrated in FIG 3. The A-site cation with a +1 charge is typically methyl-ammonium (CH_3NH_3) (MA+), caesium (Cs+) or formamidinium $[HC(NH_2)_2]$ (FA+). The B-site metal cation with a +2 charge is typically lead (Pb) or tin (Sn), and the X-site anion with charge -1 is a halide, typically Br– or I–. Hybrid metal halide perovskites have demonstrated high absorption coefficients [9], so that relatively thin films on the order of nanometers can absorb a large fraction of the photons above the bandgap in one pass. Their long carrier diffusion lengths [9] and high radiative efficiencies [10] ensure that photogenerated electrons and holes can travel to the negative and positive electrodes respectively, with minimal current and voltage loss. Hybrid lead halide perovskites have also demonstrated high defect tolerances [11], enabling versatile solution or vapour processing methods. Thin-film perovskites have thus demonstrated the potential for lightweight, flexible and high efficiency cells. Their flexibility and versatility in processing enables the use of roll-to-roll processing to increase production throughput, and their desirable optical properties have the potential to decrease fabrication cost due to less raw material being needed, as compared to c-Si cells which are rigid with typical thicknesses on the order of hundreds of micrometers. These attractive qualities have drawn considerable attention to hybrid metal halide perovskites in recent years, as a promising challenger to c-Si PV technology. They have been the fastest growing solar cell technology in terms of PCE in the last decade, increasing from 3.8% in 2009 [12] to the current certified PCE single-junction record of 25.5%, and thus already approaching to the record PCE of 26.7% for single-junction c-Si [13]. Metal halide perovskites are also well-suited for use in tandem configurations. A key aspect of their suitability is the ability to tune their bandgap through a process called compositional engineering, in which the composition of the alloy perovskite is altered. For hybrid metal halide perovskites, the conduction band minimum and valence band maximum are both determined by the orbital overlaps of the B-site metal and X-site halides, so that subsitution of I^- for Br^- leads to greater bandgap. This is due to Br^- having a smaller ionic radius of 1.96 Å as compared to I^- with radius 2.2 Å [14], leading to a contraction of the lattice and decreased orbital overlab between the X-site cation and B-site anion, ultimately narrowing the bands and widening the bandgap. Exchanging of the A-site cation can also tune the bandgap; although it does not directly affect the density of states at the band edge, using a cation with

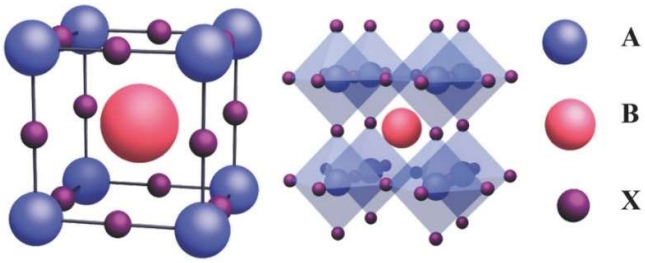


Figure 3: Perovskite structure. Unit cell of an ideal cubic perovskite ABX_3 (left) and the extended crystalline structure connected by corner-sharing octahedra (right). Reproduced from ref [9].

smaller ionic radius such as Cs contracts the lattice and tilts the $[BX_6]^{-4}$ octahedra by increasing the X-B-X bond angle, leading to increased band gap [15] due to increased orbital overlab between the B and X sites. Noh et. al. [14] and Eperon et. al. [16] demonstrated that the bandgap energies of $MAPb[I_{(1-y)}Br_y]_3$ and $FAPb[I_{(1-y)}Br_y]_3$ can be tuned from 1.48 to 2.3 eV by varying y from 0 to 1, using ultraviolet-visible (UV-Vis) spectroscopy to determine the bandgap energies. McMeekin et al. [17] studied the compositional tunability of the $FAPb[I_{(1-y)}Br_y]_3$ perovskite and found that a "yellowing" of films would occur for compositions of y between 0.3 and 0.6, associated with the transition from a trigonal ($y < 0.3$) to cubic ($y > 0.6$) crystal structure. This structural instability decreases open-circuit voltage V_{oc}, due to the material being unable to crystallize near the transition and thus having unexpectedly low absorption. McMeekin et al. found that when a mixture of Cs and FA was used in the A-site, the resulting $FA_{(1-x)}Cs_xPb[I_{(1-y)}Br_y]_3$ perovskite was more thermally stable than $MAPbI_3$, and achieved a continuous and compositionally stable bandgap evolution across a large fraction of the Cs to FA compositional space and the entire I to Br compositional space. A champion composition $FA_{0.83}Cs_{0.17}Pb(I_{0.6}Br_{0.4})_3$, with a near optimal bandgap energy of ~1.74 eV was identified, which was used to fabricate single-junction devices with over 17% efficiency, demonstrating the feasibility of tandem 4T solar cells with over 25% efficiency. Bush et al. [18] demonstrated the viability of wide-bandgap hybrid metal halide perovskites as the top cell in 2T architectures. They fabricated a 23.6% efficient 2T tandem cell using a c-Si base absorber and $FA_{0.83}Cs_{0.17}Pb(I_{0.83}Br_{0.17})_3$ as the top cell, which has a near optimal bandgap of 1.63 eV. The current certified perovskite-Si PCE record attained by Oxford PV stands at 29.5% [13], although the details of the composition used have not been published.

High-efficiency all-perovskite tandem cells were initially not viable due to a lack of low-bandgap perovskites for use as effective base absorbers. Heo and Im [19] demonstrated the first 2T all-perovskite tandem device in 2015 using $MAPbBr_3$ and $MAPbI_3$ as the front and rear cells, but the suboptimal bandgaps of 2.25 eV and 1.55 eV respectively lead to poor tandem device performance of 10.8% PCE. A key breakthrough in the development of all-perovskite tandem cells was the partial substitution of Pb by Sn, which was used to achieve bandgap energies of 1.2-1.3 eV. A PCE of 20.3% was achieved by Eperon et al [8] using a 1.22 eV $FA_{0.75}C_{0.25}Pb_{0.5}Sn_{0.5}I_3$ base absorber with a 1.6 eV $FA_{0.83}Cs_{0.17}Pb(I_{0.5}Br_{0.5})_3$ top cell. The current perovskite-perovskite PCE record stands at 26.4% [20], using a Pb-Sn narrow bandgap perovskite with a mixed Br-I wide-bandgap perovskite, although the details of the precise composition used have not been made publicly available. Thus, all-perovskite tandem cells have the potential outperform today's c-Si solar cells.

A key drawback to the use of metal mixed-halide perovskites in solar cells is the phenomenon of reversible photoinduced halide segregation, referred to hereon as the Hoke effect. Mixed I/Br perovskites had been observed to underperform despite the success of compositional engineering; Noh et al. showed that the increase in bandgap from increasing the ratio of Br to I at the X site did not yield a corresponding increase in open-circuit voltage [14]. Hoke et al. [21] showed that, upon exposure to above-bandgap wavelengths of light, the halides I and Br in $MAPb[I_{(1-y)}Br_y]_3$ migrate to lower-bandgap I-rich and higher-bandgap Br-rich regions, as opposed to being uniformly distributed in the well-mixed phase. Photogenerated carriers then funnel towards the lower-bandgap I-rich regions, which act as non-radiative recombination centres [15], resulting in a loss of voltage and reduced PCE as predicted by Shockley-Queisser theory (Eqn [A.14]). The Hoke effect is also detrimental to the application of perovskites in tandem configurations, as the I-rich regions cause significant sub-bandgap absorption, which disrupts the careful bandgap matching required for optimally efficient tandem cells. Hoke et al. found that this photoinduced halide segregation led to the photoluminescence (PL) spectra of metal halide perovskites developing a new, higher-wavelength peak corresponding to the segregated phase of mixed-halide perovskites, in which significant I-rich regions dominate the PL spectrum. This is because the I-rich regions have lower bandgap, and the photogenerated carriers thermalise to the lowest energy states and thus predominately emit from the lowest bandgap domains. These higher-wavelength peaks were observed to grow in intensity when the perovskites were exposed to constant, 1-sun illumination. Bush et al. [15] found that using higher ratios of Cs at the A-site cation reduces the severity of the Hoke effect and increases open-circuit voltage, making it a favourable technique for compositional tuning of the bandgap. Morphology has also been observed to play a role in the susceptibility of mixed-halide perovskites to the Hoke effect. In amorphous polycrystalline materials such as hybrid metal halide perovskites, the material is composed of many crystallites, or crystal grains, made of varying size and orientation, with each individual grain

being highly ordered according to the symmetry of the crystal lattice. Hu et al. [22] reported that larger grain sizes showed a reduction in both XRD peak-splitting and PL peak red-shifting, with Sutter-Fella et al. [23] observing similar improvements with enhancement in film quality. Slotcavage et al. proposed that these enhancements limit the Hoke effect as ion mobility is higher at grain boundaries, so that having bigger grains, which leads to a smaller total number of grain boundaries, hinders the migration of halides to I-rich and Br-rich regions [24].

In this project, I investigated the compositional space of $FA_{(1-x)}Cs_xPb[I_{(1-y)}Br_y]_3$ to identify compositions suitable for use as the wide bandgap absorber in all-perovskite tandem configurations. A 2 eV bandgap composition was desired; such a composition would have the optimal bandgap energy to be used alongside a 1.56 eV $MAPbI_3$ base absorber in a 2T double tandem cell (FIG 2a). A 2 eV composition would also be optimal for use as the top cell in a Si-perovskite-perovskite triple junction (APPENDIX A.3b). In this project, films were fabricated over a range of Fa-Cs and I-Br ratios, and UV-Vis optical spectroscopy was performed to map out the bandgap variation with composition. Photoluminescence (PL) measurements were performed on compositions with bandgap energies near 2 eV to investigate their susceptibility to the Hoke effect. SEM measurements were carried out on some compositions, to investigate their morphology and examine any relation between their grain size and their susceptibility to the Hoke effect. Champion compositions were then selected, based on proximity to a 2 eV bandgap energy and stability to the Hoke effect, and single-junction devices were fabricated to demonstrate their potential impact in tandem configurations. The details of these experimental methods are outlined in the next section.

2. EXPERIMENTAL METHODS

2.1 Device preparation

The perovskite precursor materials FABr, CsBr, PbI_3 and $PbBr_3$ were mixed in stochiometric ratios in a nitrogen filled glovebox to yield 1M solutions of $FAPb[I_{(1-y)}Br_y]_3$ and $FA_{0.75}Cs_{0.25}Pb[I_{(1-y)}Br_y]_3$ for varying values of y between 0.4 and 0.8. They were stirred in a 4:1 ratio of dimethyl formamide (DMF) to dimethyl sulfoxide (DMSO); these solvents were used to dissolve the precursor materials and form well-mixed solutions. The solutions were then mixed by varying volumes to yield solutions of $FA_{(1-x)}Cs_xPb[I_{(1-y)}Br_y]_3$ with values of x between 0 and 0.25 in 0.05 increments, and then stored in the glovebox.

Glass substrates coated with fluorine-doped tin oxide (FTO) were cleaned using a detergent and toothbrush, and then were placed in an ultrasonic water bath for 15 minutes at a time in a beaker of Decon 90, followed by de-ionised water, then acetone, then isopropanol (IPA). The substrates were then dried using a nitrogen gas spray gun and placed in an O_2 plasma for 10 minutes for further cleaning. Just before deposition, the substrates were placed in an O_3 plasma for 15 minutes to increase the surface energy of the substrates, to increase wettability and improve the smoothness of the film formation. Care was taken when transporting the substrates between steps of the cleaning process, to minimise defects contaminating the substrate and hindering film formation.

The optimised perovskite deposition process used, which had been developed by the research group, was as follows. The entire deposition and annealing process was done in a nitrogen-filled glovebox, as moisture hinders the film formation. A Laurell spin-coater was used to form the perovskite thin film, the mechanics of which are described in APPENDIX B.1a. The spin-coater was programmed to spin for 35s at 6000 rpm with an acceleration and deceleration of 2000 $rpms^{-1}$. 185 μl of perovskite solution was statically deposited onto the FTO-coated side of the substrate, and then 325 μl of ethyl acetate antisolvent was dynamically deposited, to crystallize the solution, 12 seconds after the spin program was started. After spin-coating, the substrate was annealed to evaporate any remaining solvent and form the crystallized film by placing the substrate on a hot plate at 110°C for 30 minutes.

For device fabrication, substrates coated with indium tin oxide (ITO) were used. The device architecture is detailed in APPENDIX B.1b; from bottom to top, the layers were glass, ITO, Me-4PACz, Al_2O_3, perovskite, PCBM, BCP, Au. The same substrate cleaning process as detailed above was used, and deposition of all layers was done in a nitrogen gas filled glovebox to mitigate the impact of moisture on film formation. A self-assembling monolayer of Me-4PACz was spin-coated onto the substrates; this formed the p-junction of the device. The spin program was 3000 rpm for 30s, with a 6000$rpms^{-1}$ acceleration. 100 μl of Me-4PACz was statically deposited onto the substrate immediately before the spin program was started. The substrates were then annealed for 10 minutes at 100°C. Then, a layer of alumina (Al_2O_3) nanoparticles was spin-coated onto the substrates to increase the wettability of the Me-4PACz. Alumina has also been shown to mitigate perovskite absorber degradation in solar cells by hindering migration of halides from the perovskite into the charge transport layer [25]. The spin program was 5000 rpm for 20s with 2000 $rpms^{-1}$ acceleration and deceleration. 40 μl was dynamically deposited 3s after the spin program was started. After this, the perovskite solution was spin-coated onto the substrate using the same process and amounts as detailed earlier. Then, a transport layer of Phenyl-C61-butyric acid methyl ester (PCBM) was spin-coated onto the substrate. PCBM performs a similar role to alumina, in that it immobilizes halide ion migration, allowing for effective photogenerated electron transport from the perovskite absorber to the n-junction layer above it. The PCBM was dissolved in a concentration 20 mg/ml, in a 3:1 ratio of chlorobenzene to dichlorobenzene. It was filtered

through a 0.22 μm pore size syringe of Polytetrafluoroethylene (PTFE) before application. The spin program used was 2000rpm for 20s with an acceleration and deceleration of 2000rpms^{-1}. 80 μl was dynamically deposited 3s after the spin program was started. The substrates were then annealed for 5 minutes at 100°. Finally, a layer of BCP was spin-coated, which formed the n-junction of the device. The BCP was dissolved in a concentration of 0.5 mg/ml in IPA and stirred overnight. The BCP was filtered through a 0.22 μm pore size PTFE syringe. Once all layers were deposited, the substrates were etched to create the collection areas for forming the top electrode, and 80 nm of gold (Au) was deposited onto the collection areas by means of evaporation.

To measure the efficacy of the fabricated devices, a Wavelabs solar simulator was used which exposed the devices to the AM 1.5G spectrum at 1 sun intensity. Light was emitted from a lamp above the devices, and shadow masks were used of to standardise the area of exposure for all devices to one large pixel of area 1 cm^2 and four small pixels of area 0.25 cm^2. The devices were kept at a constant test temperature of 25°C, and a four-point probe was used to minimise the effects of contact resistance. Applied bias voltage sweeps were performed, upon illumination of the devices, from -0.1V to 1.5 V over 4 s, and a Wavelabs IV-Electronics system was used to measure the steady-state J-V characteristics of the cells over 30 s.

2.2 Optical spectroscopy

Ultraviolet-visible (UV-Vis) spectroscopy was carried out to determine the absorbance spectra of perovskite compositions deposited onto FTO-coated substrates. In UV-Vis spectroscopy, a spectrophotometer measures the intensity of light I after passing through the sample and the incident light intensity I_0, in order to calculate the absorbance $A = -log((I_0 - I)/I_0)$. A Cary-300 spectrophotometer was used with a Perkin Elmer Lambda 1050 spectrometer, controlled by the Cary WinUV software. The integrating sphere is a spherical cavity whose inner wall is coated with a highly reflective material, so that light which has passed through the sample undergoes multiple reflections, removing the angular dependence of the detected signal. The spectrophotometer light sources were deuterium and halogen lamps were for the UV, and visible and near-infrared spectral ranges, respectively. A photomultiplier tube and lead sulfide (PbS) detector were used for light detection for the UV and visible, and near-infrared ranges, respectively. Absorbance was measured for a wavelength range of 800 to 350 nm in 1nm intervals at a scan rate of 600 nm/min. Background measurements were taken by placing an opaque block in the sample holder, and empty measurements were taken by leaving the sample holder empty. These measurements were then used by the Cary WinUV software to isolate the signal due to absorbance by the samples.

2.3 PLQE Measurements

Photoluminescence quantum efficiency (PLQE) measurements were carried out to determine the photoluminescence (PL) spectra and radiative efficiencies of perovskite compositions deposited onto glass substrates. FTO-coated substrates were not used, as it was observed that films deposited on glass-only substrates had increased PL intensity, so that PL peaks could be resolved more clearly. In a PL measurement, the perovskites are excited by incoming laser light, and charge carriers are photogenerated. These electrons and holes then undergo momentum relaxation towards the bandgap minimum and recombine with subsequent emission of photons, whose energies are slightly below the bandgap energy due to the Stokes shift between the absorption and emission spectra. Guo et al. [26] showed that the Stokes shift for metal halide perovskites occurs because parts of the crystal lattice may be in an excited state, and absorption excites an electron-hole pair before the lattice can relax from the excited state, whereas lattice relaxation may occur before emission. The spectral emission of photons, known as the photoluminescence spectrum (PL), is then measured, and the external radiative quantum efficiency, defined as the ratio of emitted to absorbed photons, is calculated. A 450 nm ThorLabs L450P1600MM laser was used at 1 sun intensity. The laser was driven by a ThorLabs LDC210C laser diode current controller. The sample was kept at a constant temperature of 25°C using a ThorLabs TED200C temperature controller. An Ocean Optics QEPro High Performance Spectrometer was used to detect the PL emission. PL was measured for a wavelength range of 278nm to 1065 nm in 0.8 nm increments. An integrating sphere was used to remove the angular dependence of the emission, and the emission was distinguished from background signal and the excitation source by utilising the method of de Mello et al. [27], visualised in APPENDIX B.1c. Some fraction of the laser light scattered from the sphere wall is absorbed by the sample, so the "sample out" data sets were therefore appropriately scaled down after subtracting the background signal, and subtracted from the "sample in" data sets in order to remove the laser excitation peaks.

2.4 SEM Measurements

The surface morphology of perovskite films on FTO-coated substrates were observed using a scanning electron microscope (SEM), to determine the typical grain sizes of different compositions. The SEM produces images with high resolutions on the order of micrometres, by scanning the sample surface with a focussed beam of electrons, which excite sample atoms. Those excited atoms then emit secondary electrons, which are detected with a Secondary Electron (SE) detector. A FEI Quanta 600 FEG SEM was used. The instruments were controlled using the xT Microscope Control, to reduce the astigmatism of the

electron beam and adjust the contrast of the image so that image clarity was enhanced.

3. RESULTS AND INTERPRETATIONS

3.1 Optical absorption properties

UV-Vis spectroscopy was carried out on a range of compositions $FA_{(1-x)}Cs_xPb[I_{(1-y)}Br_y]_3$, for values of y between 0.3 and 0.8, and values of x between 0 and 0.25 in 0.05 increments. Multiple samples of each composition on FTO-coated substrates were fabricated. The films were consistently observed to be less specular for samples with $x = 0.2, 0.25$, indicating that the deposition process used was not optimal for high Cs content compositions. An absorption edge was seen between 570 nm and 730 nm, corresponding to the tetragonal perovskite phase, for all compositions apart from those with $(x,\ y)$ = (0,0.3), (0.05,0.3), (0,0.5). These compositions are likely to have been in a non-perovskite phase, as the Cs content was too low, so that the compositions were in the region of structural phase instability reported by McMeekin et al. [17]. The absorption band edge was seen to blue shift with increasing y, as visualised for one composition in FIG 5a, implying that the bandgap energy was increasing with increasing Br content. A much smaller blue shift was seen with increasing Cs content. Absorbance plots for all observed compositions may be found in APPENDIX C.1(i). To infer the bandgap energies from the absorbance spectra, the method of Tauc plots was used, which was first proposed by Tauc et al. [28] and then further developed by Davis and Mott [29]; the details of this method are beyond the scope of this paper. This method assumes the relationship between absorbance A and energy near the optical absorption band edge for an amorphous direct bandgap semiconductor to be:

$$(Ah\omega)^2 = B\left(\hbar\omega - E_g\right) \qquad [1]$$

Here, ω is the frequency of an incident photon that produces a hole-electron pair, and B is a constant. Using this, E_g may be inferred by extrapolating the band edge in a plot of $(Ah\omega)^2$ to the abscissa. For this relation to hold, there must be negligible sub-bandgap absorption. However, non-negligible absorption was observed for some samples, so that directly fitting to Eqn [1] would underestimate the bandgap energy; an example is illustrated in FIG 5b. To increase accuracy, the method by Makuła et al. [30] was used, where the effect of sub-bandgap absorption is mitigated by applying a linear fit to the slope below the absorption edge, and calculating the intersection point between the sub-bandgap slope and the absorption edge slope, as illustrated in FIG 5b. The fitted Tauc plots for all compositions may be found in APPENDIX C.1(ii), and the inferred bandgaps and their estimated uncertainties may be found in APPENDIX C.1(iii). The uncertainties were estimated from the standard deviations of the measured bandgap energies for multiple samples. The inferred bandgap energy variation, illustrated in FIG 5c,d, was found to be linear with y across the entire observed compositional space, in agreement with previous observations of similar compositional spaces of $FA_{(1-x)}Cs_xPb[I_{(1-y)}Br_y]_3$ [17][18]. The optical bandgap was therefore observed to follow Vegard's Law. Vegard's Law is an empirical relation that predicts that the variation of the optical bandgap energy in an alloy semiconductor is approximately linear with composition, plus a quadratic bowing energy that represents the degree of anisotropies in the crystal field [14]. The results of fitting to Vegard's Law are illustrated in APPENDIX C.1(iv); the variation of E_g with y was observed to be highly linear, implying a low bowing energy and thus suggesting that $FA_{(1-x)}Cs_xPb[I_{(1-y)}Br_y]_3$ has good miscibility across the observed compositional space. The bandgap energy was found to vary compositionally at a rate of:

$$\Delta E_g = 7.47 \pm 0.26 \text{ meV / \%Br}$$

This is slightly higher than the 5.7 ± 0.2 meV / %Br rate of increase observed for the $0.05 \leq y \leq 0.3$, $0.15 \leq x \leq 0.4$ compositional space investigated by Bush et al. [18], which had $1.55 \leq E_g \leq 1.75$. This may be due to some degree of bowing occurring across the wider compositional space, which was not severe enough to be detected in the observed compositional space. E_g was also observed to vary approximately linearly with x. For 30% Br compositions, the E_g rate of increase with Cs % was found to be 2.41 ± 0.09 meV / %Cs. This agrees with the rate of increase observed by Bush et al. for 30% Br compositions over the $0.15 \leq x \leq 0.4$ compositional space. The rate of increase with x decreased for higher y, suggesting the method of tuning to higher E_g with increasing Cs% is less effective for higher Br% compositions. Interpolation was performed on the observed bandgaps to map out the E_g compositional space, with bilinear interpolation being used due to the linearity of the variation of E_g across the observed compositional space. The result is shown in APPENDIX C.1(v) and the region near 2eV is illustrated in FIG 5e. The fractional uncertainty in the 2eV contour was estimated by assuming it to be equal to the largest fractional uncertainty of the measured bandgaps. The results suggest a 95% certainty that a composition with $E_g = 2.0 \pm 0.04$ eV may be obtained with values of (x, y) within the dashed lines in FIG 5e: $0.64 \lesssim y \lesssim 0.75$, $0 \lesssim x \lesssim 0.25$.

3.2 PL/PLQE properties

PLQE measurements were performed on samples with $y = 0.65, 0.67, 0.7, 0.72$ and values of x between 0 and 0.25, as the UV-Vis spectroscopy results implied that these compositions would have $E_g \cong 2$ eV. Measurements of the PL spectrum were taken every 5s across a 15-minute interval. For all compositions, an initial peak in the PL spectrum was observed in the 600-650 nm range. Over time, a second peak grew in the 740-800 nm range, and

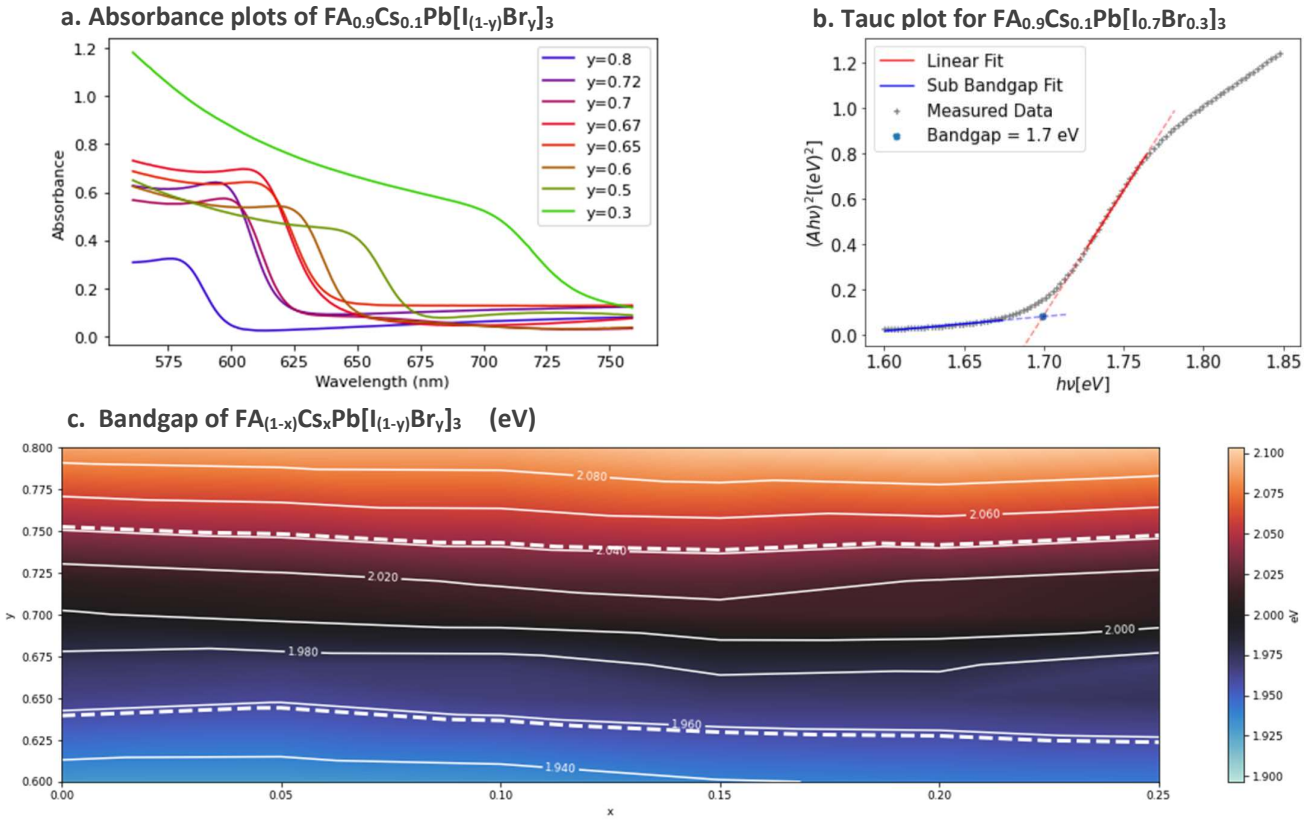


Figure 5: UV-Visible Spectroscopy results. (a) Blue-shifting of absorption band edge with increasing Br content. **(b)** Illustration of Tauc plot method with extrapolation used to calculate bandgap. **(c)** Results of linear interpolation of bandgap energies, cropped to values near 2 eV. Dashed line indicates 3-σ uncertainty in 2 eV contour.

dominated the PL spectra within 50s for most observed compositions. The time evolution of the PL spectrum of each observed composition is illustrated in APPENDIX C.2(i) These observations indicate that $FA_{(1-x)}Cs_xPb[I_{(1-y)}Br_y]_3$ is susceptible to the Hoke effect across the observed compositional space, with the two peaks corresponding to the well-mixed unsegregated phase, and the segregated phase in which I-rich and Br-rich regions develop. The rate at which halide segregation occurred was characterized by fitting the data to the sum of two Voigt functions, and then calculating the time evolution of the ratio of the segregated peak area to total peak area. Voigt functions were used to fit to the peaks, as they were found to fit the data better than Gaussian functions. The time evolutions of the fitted peak area ratios for all compositions may be found in APPENDIX C.2(ii). The time evolutions were fitted to stretched exponentials as the decay curves were slightly skewed for higher Cs content samples, reflected in the lower β-values that were returned by the fitting program. At later times, when the unsegregated phase peak had an intensity exceeding 10^4 counts, the peak was observed to become asymmetric, and the sum of two Voigt functions was found to poorly fit the data for all compositions. An example of this may be found in APPENDIX C.2(iii). Due to this, the stretched exponentials were only fitted to the time period in which the fits were accurate, which was ~300s for most compositions. The time constants for the resulting fits are illustrated in FIG 6*d*. The rate of halide segregation was observed to be lower for compositions with low Br and high Cs content. This agrees with Bush et al.'s [15] observation of the Hoke effect for the compositional space of $FA_{(1-x)}Cs_xPb[I_{(1-y)}Br_y]_3$ with $0.05 \leq y \leq 0.3,\ 0.15 \leq x \leq 0.4$. Therefore, tuning the composition of $FA_{(1-x)}Cs_xPb[I_{(1-y)}Br_y]_3$ to have higher Cs content is a possible method to suppress the Hoke effect and attain better performing devices, in the higher bandgap 2 eV region as well as the $1.55 \leq E_g \leq 1.75$ eV region investigated by Bush et al. [15].

3.3 Device performances

Devices were fabricated for compositions with $y = 0.65$ and $x = 0.1,0.15,0.2,0.25$, to balance proximity to a 2 eV bandgap energy and stability to the Hoke effect. The performances of these devices were tested in a solar simulator; the observed steady-state J-V characteristics may be found in APPENDIX C.3. The best observed PCEs were ~9% for Cs contents of $x = 0.1,0.15$. The devices with higher Cs contents of $x = 0.2,0.25$ were found to perform worse; this may be due to the poorly optimised deposition process hindering film formation for higher Cs% which was consistently observed. There was also considerable variation in the attained performances,

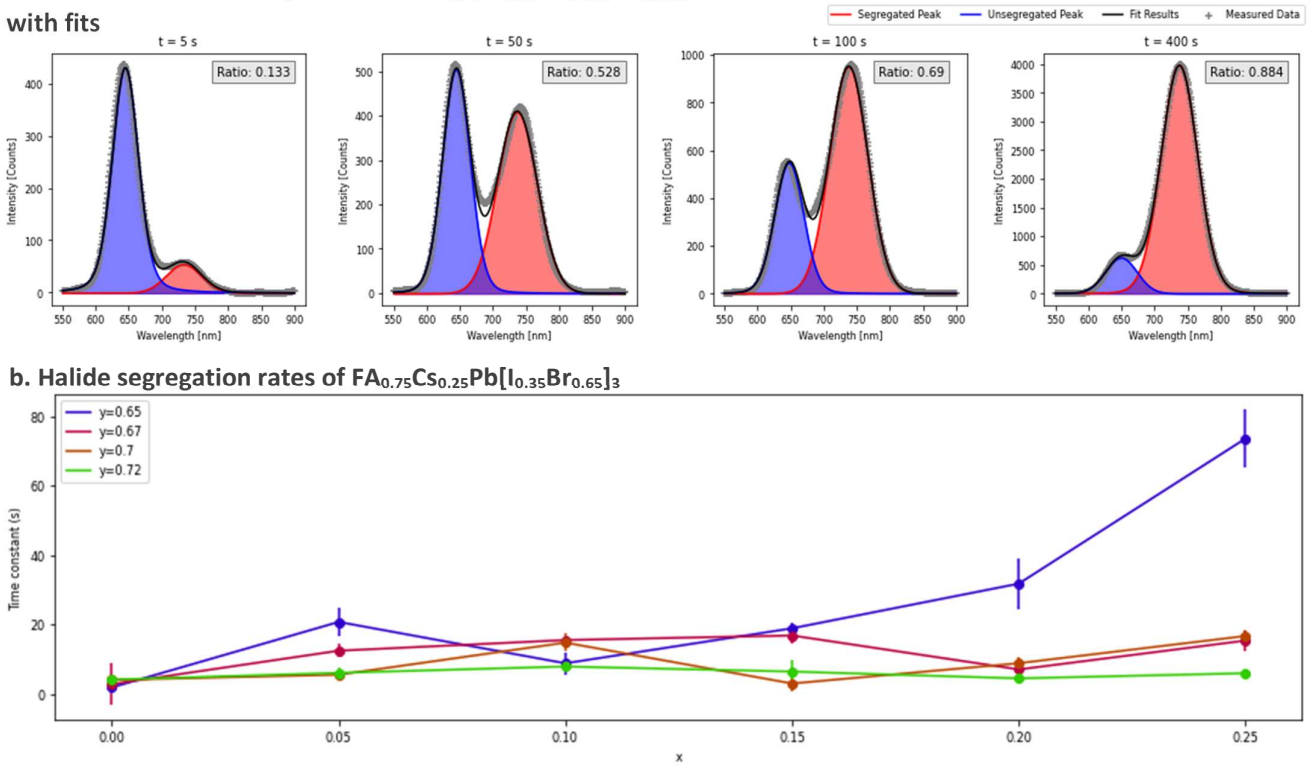


Figure 6: PLQE results. (a) Illustration of peak fitting used to calculate the time evolution of the ratio of segregated to unsegregated phase peaks. **(b)** Calculated segregation rates from fitting stretched exponentials

indicating that the fabrication process requires further optimisation to improve consistency. The champion devices had short-circuit current densities of J_{sc}~12 mA cm^{-2}, which match the optimal $10 \leq J_{sc} \leq 12$ mA cm^{-2} required by the current-matching condition for a 2T tandem cell with 1.55 eV and 2 eV bandgap absorbers [31]. They also attained high open-circuit voltages of V_{oc}~1.2V. Therefore, with further optimisation of the fabrication process, these materials are promising candidates for achieving highly efficient tandem solar cells.

3.4 Morphology

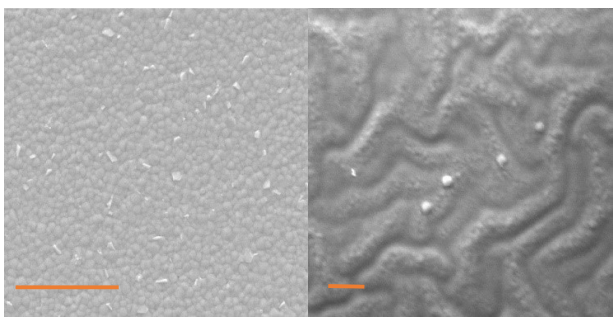


Figure 7: SEM images of morphology. Orange line indicates a length of 5 μm to scale for each image.

SEM measurements were performed on compositions with Br contents of 65%, as those compositions were observed to undergo halide segregation at the slowest rate and were also used to fabricate devices. SEM measurements were also performed on compositions with Br contents of 30%, to examine how halide substitution affected morphology. The typical grain sizes were observed to be ~300nm (FIG 7a), and film quality was inconsistent, with wrinkling observed for some compositions (FIG 7b). These are smaller than the grain sizes of ~1µm for $MAPbBr_xI_{3-x}$ achieved by Hu et al. [32] which yielded films that were stable to the Hoke effect. Therefore, further optimisation of the film fabrication process to increase the typical grain sizes of $FA_{(1-x)}Cs_xPb[I_{(1-y)}Br_y]_3$ may yield better stability to the Hoke effect. The use of MACl as an additive [33] and PTAA as a charge transport layer [32] have both been shown to enhance crystallinity for the mixed halide perovskite $MAPbBr_xI_{3-x}$. The effects of their usage in the fabrication of $FA_{(1-x)}Cs_xPb[I_{(1-y)}Br_y]_3$ are avenues for further research to enhance crystallinity and mitigate the Hoke effect.

4. CONCLUSIONS

The mixed-halide lead perovskite $FA_{(1-x)}Cs_xPb[I_{(1-y)}Br_y]_3$ has been investigated for use as the wide-bandgap absorber in tandem solar cells. The bandgap energies (E_g) of $FA_{(1-x)}Cs_xPb[I_{(1-y)}Br_y]_3$ were determined for a range of compositions in the compositional space of $0.3 \leq y \leq 0.8$,

$0 \leq x \leq 0.25$, using UV-Visible spectroscopy. The variation in E_g with composition was observed to be highly linear. Tuning the composition of $FA_{(1-x)}Cs_xPb[I_{(1-y)}Br_y]_3$ to have higher Cs content was found to be less effective as a method to attain wider bandgap energies, for higher Br content compositions with $y \sim 0.7$. Linear interpolation of the observed compositions indicated that the compositional region of $0.64 \lesssim y \lesssim 0.75$, $0 \lesssim x \lesssim 0.25$ has a bandgap energy of $E_g = 2.0 \pm 0.04$ with a 95% certainty. Observations of the photoluminescence (PL) spectra of $FA_{(1-x)}Cs_xPb[I_{(1-y)}Br_y]_3$ over an extended period of time under 1 sun intensity illumination showed that all observed compositions were susceptible to photoinduced halide segregation, in which the well-mixed phase of $FA_{(1-x)}Cs_xPb[I_{(1-y)}Br_y]_3$ breaks down into a segregated phase consisting of I-rich and Br-rich regions. The rate of halide segregation was observed to be higher for compositions with higher Br content and lower Cs content. The segregated phase was observed to contribute over 90% of the PL spectral radiance within 20s of illumination to 1 sun intensity light for compositions with $y = 0.7, 0.72$, whereas it took over 100s for compositions with $y = 0.65$. Observations of the surface morphology of the observed perovskite using a scanning-electron microscope indicated a small typical grain size of ~300 nm and poor film uniformity, highlighting the need for further optimisation of the deposition process used. Devices were fabricated for compositions in the 2 eV region that were observed to undergo halide segregation most slowly, with a champion device achieving a high 9.53% power-conversion efficiency, a short-circuit current density of 11.6 mA cm^{-2} and an open-circuit voltage of 1.25 V. These results show that $FA_{(1-x)}Cs_xPb[I_{(1-y)}Br_y]_3$ is a highly promising candidate for use in tandem solar cells, and encourage further research into the optimal fabrication process of $FA_{(1-x)}Cs_xPb[I_{(1-y)}Br_y]_3$ to realise stable and highly efficient wide bandgap absorbers.

5. REFERENCES

1. Ballif, C. *et al., Nat. Rev. Mater.* **2022**, https://doi.org/10.1038/s41578-022-00423-2
2. Eperon, G. E.; Horántner, M. T.; Snaith, H. J., *Nat. Rev. Chem.* **2017**, *1* (12), 0095
3. National Renewable Energy Laboratory (NREL), Best Research-Cell Efficiency Chart. https://www.nrel.gov/pv/cell-efficiency.html (accessed April **2022**).
4. Shockley, W.; Queisser, H. J., *J. Appl. Phys.* **1961,** *32,* 510
5. Richter, A.; Hermle, M.; Glunz S. W., *IEEE J. Photovolt.* **2013**, *3*, 1184
6. Rühle, S., *J. Sol. Ener.* **2016,** *130*, 139
7. de Vos, A., *J. Phys. D: Appl. Phys.***1980,** *13*, 839
8. Eperon, G. E.; Leijtens, T.; Bush, A. K. *et al.*, *Science* **2016** *354* (6314), 861-865
9. Stranks, S. D. et. al., *Science* **2013**, *342*, 341– 344
10. Johnston, M. B.; Herz, L. M., *Acc. Chem. Res.* **2016,** *49* (1), 146-154.
11. Steirer, K. X.; Schulz, P.; Teeter, G.; Stevanovic, V. *et al., ACS Energy Lett*. **2016**, *1*, 360−366.
12. Kojima, A; Teshima, K.; Shirai, Y.; Miyasaka, T., *J. Am. Chem. Soc.* **2009**, *131* (17), 6050–6051
13. Green, M.A.; Dunlop, E.D.; Hohl-Ebinger, J.; Yoshita, M.; Kopidakis, N.; Hao, X., *Prog Photovolt Res Appl*. **2021**, *29*, 657– 667.
14. Noh, J.H.; Im, S.H.; Heo, J.H.; Mandal, T.N.; Seok, S.I., *Nano Lett.* **2013**, *13* (4) 1764–1769
15. Bush, K. A.; Frohna, K.; Prasanna, R.; Beal, R. E. *et al.*, *ACS Energy Lett.* **2018**, *3* (2), 428–435
16. Eperon, G. E.; Stranks, S. D.; Menealou, C.; Johnston, M. B.; Herz, L. M.; Snaith, H. J., *Energy Environ. Sci.*, **2014**,*7*, 982-988
17. McMeekin, D. P.; Sadoughi, G.; Rehman, W. *et al.*, *Science* **2016,** *351* (6269), 151-155
18. Bush, K.; Palmstrom, A.; Yu, Z. *et al.*, *Nat Energy* **2017**, *2* (17009)
19. Heo, J. H.; Im, S. H.; *Adv. Mater.* **2016**, *28*, 5121–5125
20. Lin, R.; Xu, J. *et al., Nature* **2022** *603***,** 73–78
21. Hoke E. T.; Slotcavage D. J.; Dohner E. R. *et al.*, *Chem. Sci.* **2015,** *6*, 613–617
22. Krishnamurthy Grandhi, G.; Vishwanath N. S. M. *et al.*, *Phys. Chem. Lett.* **2020**, *11* (9), 3699–3704
23. Sutter-Fella, C. M. et al,, *Nano Lett.* **2016**, *16* (1), 800–806
24. Slotcavage, D. J.; Karunadasa H. I.; McGehee M. D., *ACS Energy Lett.* **2016**, *1* (6), 1199–1205
25. Chittaranjan, D.; Kot, M.; Hellmann, T. *et al.*, *Cell Rep. Phys. Sci*. **2020**, *1* (7), 100112
26. Guo, Y. *et al., Nat Commun* **2019**, *10* **(**1175)
27. de Mello, J.C.; Wittmann, H.F.; Friend, R.H.; *Adv. Mater.* **1997***, 9*, 230-232
28. Tauc, J.; Grigorovici, R.; Vancu, A., *Phys. Stat. Sol. (b)* **1966**, *15* 627-637.
29. Davis, E.; Mott, N. *Philos. Mag.* **1970**, *22*, 0903-0922
30. Makuła, P.; Pacia, M.; Macyk, W., *J. Phys. Chem. Lett.* **2018**, *9* (23), 6814–6817
31. Forgács, D. *et al.*, *J. Mater. Chem. A* **2017**, *5*, 3203
32. Hu, M. *et al*., (2016). *Adv. Sci.* **2016**, *3*, 1500301
33. Kim, M. *et al.*, *Joule* **2019**, *3* (9), 2179-2192
34. A. Mishra; N. Bhatt; A. K. Bajpai; *Nanomaterials-Based Coatings: Fundamentals and Applications*, **2019**, 397–424

APPENDIX

A.1 Shockley-Quiesser Limit

The original derivation of the detailed balance limit by Shockley and Queisser [3] is briefly reproduced here.
There are three factors limiting the efficiency of such a solar cell: spectrum loss; recombination loss; and loss due to a non-rectangular I-V characteristic.
Spectrum loss was modelled by Shockley and Queisser as the "ultimate efficiency" u of a general photoelectric device with a single cutoff frequency ν_g. Two competing processes were considered in the derivation:

i. Only above bandgap photons can be absorbed by the semiconductor in the solar cell, so there is a minimum frequency of $\nu \geq \nu_g = E_g/h$ where h is the Planck constant and E_g is the minimum energy difference between the conduction and valence bands of the semiconductor in the solar cell, known as the "bandgap energy".
ii. Charge carriers generated by photons with $\nu \geq \nu_g$ rapidly relax to the band edge through collisions and losing any energy more than E_g; this is known as thermalisation.

To calculate the ultimate efficiency, Shockley and Queisser assumed the "ultimate efficiency hypothesis", which states that each photon with energy greater than $h\nu_g$ produces one electronic charge q at a voltage of $V_g = h\nu_g/q$, with quantum efficiency of 100%. The solar spectrum and the thermal emission of the solar cell were both modelled as black bodies, whose frequency dependence was described by the Planck function. The ultimate efficiency is then found to be:

$$u(x_g) = \frac{\text{Output power}}{\text{Input power}} = \frac{h\nu_g A Q_s}{A P_s} \qquad [A.1]$$

where A is the area of the surface subject to radiation,

$$Q_s = (2\pi/c^2)\int_{\nu_g}^{\infty} [\exp(h\nu/k_B T_s) - 1]^{-1}\, \nu^2 d\nu = [2\pi(k_B T_s)^3/h^3 c^2]\int_{x_g}^{\infty} x^2\, dx/(e^x - 1) \qquad [A.2]$$

is the number of quanta incident per unit area per unit time for black body radiation of surface temperature T_s, or the "irradiance", with $\nu \geq \nu_g$, using $x = h\nu/k_B T_s$.

$$P_s = (2\pi/c^2)\int_{0}^{\infty} [\exp(h\nu/k_B T_s) - 1]^{-1}\, \nu^3 d\nu = [2\pi(k_B T_s)^4/h^3 c^2]\int_{0}^{\infty} x^3\, dx/(e^x - 1) \qquad [A.3]$$

is the total energy density per unit area per
unit time for blackbody radiation at temperature T_s.
This gives an expression for the ultimate efficiency that is only a function of $x_g = h\nu_g/k_B T_s$:

$$u(x_g) = \left[\int_{x_g}^{\infty} x^2\, dx/(e^x - 1)\right] \Big/ \int_{0}^{\infty} x^3\, dx/(e^x - 1) \qquad [A.4]$$

The second limiting factor in the Shockley-Queisser model is loss of current due to recombination of photogenerated electron-hole pairs, with resultant emission of photons. Shockley and Queisser assumed the dominant recombination pathway to be direct radiative recombination of free holes and electrons. At zero voltage, this rate F_{c0} was assumed proportional to the rate of blackbody emission for a surface temperature equal to the cell temperature T_c:

$$F_{c0} = 2A_p t_c Q_c = 2A_p t_c Q(\nu_g, T_c) \qquad [A.5]$$

Here, A_p is the projected area of the cell normal to the solid angle of the Sun, with the factor of 2 accounting for the fact that the solar cell may radiate thermally from both sides. t_c is the probability that an incident photon of energy greater than E_g will enter the body and produce a hole-electron pair. Q_c is given by:

$$Q_C = (2\pi/c^2)\int_{\nu_g}^{\infty} [\exp(h\nu/k_B T_c) - 1]^{-1}\, \nu^2 d\nu = [2\pi(k_B T_c)^3/h^3 c^2]\int_{x_g/x_c}^{\infty} x^2\, dx/(e^x - 1) \qquad [A.6]$$

where $x_c = T_c/T_S$. The integral of Q_c over frequency has a lower bound of ν_g, as Shockley and Queisser assumed that the rate of emission of photons due to radiative recombination will be exactly equal to the rate of absorption of photons which produce recombination through photogeneration of a free electron-hole pair; these photons must have a frequency $\nu \geq \nu_g$ to overcome the bandgap. Shockley and Queisser argued that the rate of radiative recombination is proportional to the product of electron and hole densities np, and that when this is equal to the thermal equilibrium

value ${n_i}^2$, which occurs at zero applied voltage, the rate of recombination will be F_{c0}. Therefore, the rate of radiative recombination through the cell may be written as:

$$F_c(V) = F_{c0}\, np/{n_i}^2 \qquad \text{[A.7]}$$

The solar cell was modelled as an ideal diode, which obeyed the Shockley ideal diode equation [6]:

$$I = I_S[e^{\frac{V}{V_c}} - 1] \qquad \text{[A.8]}$$

Here I is the drop in hole current, I_S is the reverse bias saturation current, and $V_c = k_B T_c/q$ is the thermal voltage for a diode at temperature T_c. Assuming the solar cell acts as a black body and an ideal diode, the saturation current and rate of recombination are given by:

$$I_S = qF_{c0} \qquad \text{[A.9]}$$

$$F_c(V) = F_{c0} e^{\frac{V}{V_c}} \qquad \text{[A.10]}$$

The total rate of generation of hole-electron pairs by solar radiation incident on the cell area is:

$$F_S = A_p Q_S f_\omega t_S$$

A_p and Q_S are as defined before. t_S is the probability of an incident solar photon producing a hole-electron pair, which may differ from t_c as the two species of photons obey different spectral distributions. f_ω is a geometrical factor accounting for the limited angle from which the solar energy falls on the cell. It is equal to the ratio of the solid angle subtended by the sun, ω_s, to the solid angle from which the cell can capture sunlight.

Balancing the gain of electron-hole pairs due to incident solar radiation with the loss of electron-hole pairs due to recombination and current flow, and assuming radiative recombination is the only recombination pathway, the steady-state I-V relationship for the cell is:

$$I = q(F_S - F_{c0}) + qF_{c0}[1 - \exp(V/V_c)] = I_1 + I_0[1 - \exp(V/V_c)] \qquad \text{[A.12]}$$

$I_1 \equiv q(F_S - F_{c0})$ is the short circuit current, corresponding to $V = 0$. In most practical conditions, the rate of photogeneration of electron-hole pairs is much larger than the rate of blackbody radiation at the cell's temperature, so the latter term may be neglected, and we may assume

$$I_1 \cong qF_S = qA_p Q_S f_\omega t_S \qquad \text{[A.13]}$$

Equation [A.12] may be solved to give V_{OC}, the open circuit voltage corresponding to $I = 0$:

$$V_{OC} = V_c \ln[(I_1/I_0) + 1] = V_c \ln(fQ_S/Q_c) \qquad \text{[A.14]}$$

where $f \equiv f_\omega t_S/2t_c$ combines the transmission and geometrical factors. A more detailed derivation, accounting for possible non-radiative recombination with rate $R(0)$, and non-radiative generation with rate $R(V)$ obeying the ideal rectifier equation[3]

$$R(V) = R(0) \exp\left(\frac{V}{V_c}\right) \qquad \text{[A.15]}$$

leads to f having another factor $f_c = F_{c0}/[F_{c0} + R(0)]$:

$$f \equiv f_c f_\omega t_S/2t_c \qquad \text{[A.16]}$$

The maximum open-circuit voltage thus occurs when the temperature of the cell tends to zero, so that there is no radiative recombination. This follows from Shockley and Queisser's assumption that the rate of radiative recombination is proportional to the rate of blackbody radiation of photons with $\nu \geq \nu_g$; at $T = 0$, there is no blackbody radiation.

In this limit $T \to 0$, the radiance Q_c tends to the value:

$$-\ln Q_c = h\nu_g/k_B T_c + \mathcal{O}(\ln T_c) = V_g/V_c + \mathcal{O}(\ln T_c) \qquad \text{[A.17]}$$

Therefore, the maximum open-circuit voltage which may be obtained from the cell is the bandgap energy V_g.

For $T > 0$, the open-circuit voltage is only a fraction of V_g:

$$v(x_g, x_c, f) = V_{OC}/V_g = V_C/V_g \ln(fQ_s/Q_c) = x_c/x_g \ln(fQ_s/Q_c), \quad x_c = T_c/T_s \qquad \text{[A.18]}$$

Accounting for spectrum and recombination losses, one may calculate a nominal efficiency in terms of the incident power and the product of the open-circuit voltage and short circuit current. Using [A.1], [A.7] and [A.17]:

$$V_{OC}I_1/P_{in} = V_{OC}A_p Q_S f_\omega t_S/[A_p f_\omega h\nu_g Q_s/u(x_g)] = v(x_g, x_c, f)u(x_g)t_s \qquad \text{[A.19]}$$

The I-V characteristic introduces further loss. Since the I-V curve [A.12] is not perfectly rectangular, the actual efficiency is smaller than the ratio [A.19], as there will be an optimal voltage at which maximum output power is developed, which is not necessarily equal to V_{OC}.
The maximum power output from the solar cell is developed at a voltage V_{max} such that:

$$\left.\frac{d(IV)}{dV}\right|_{V=V_{max}} = 0 \qquad [A.20]$$

The I-V characteristic [A.12] may be rewritten using [A.14]:

$$I(V) = I_0[\exp(V_{OC}/V_c) - \exp(V/V_c)] \qquad [A.21]$$

Substituing [A.21] into [A.20] gives an expression for V_{max}:

$$I_0\{\exp(V_{OC}/V_c) - [(V_{max} + V_c)/V_c]\exp(V_{max}/V_c)\} = 0 \qquad [A.21]$$

Equation [A.22] may be recast in a simpler form using the following substitutions:

$$z_{OC} = V_{OC}/V_c = vx_g/x_c\,, \qquad z_m = V_{max}/V_c \qquad [A.22]$$

$$\Longrightarrow z_{OC} = z_m + \ln(1 + z_m) \qquad [A.23]$$

z_m is thus a function of vx_g/x_c. The ratio of maximum power to nominal power $V_{OC}I_1$ is denoted by the impedance matching factor m, which is a function of z_m and thus of x_g, x_c, f:

$$m(x_g, x_c, f) = \frac{I(V_{max})V_{max}}{I_1 V_{OC}} = \frac{{z_m}^2}{(1 + z_m - e^{-z_m})[z_m + \ln(1 + z_m)]} \qquad [A.24]$$

Using [A.24] and [A.18], the efficiency η is given by:

$$\eta(x_g, x_c, t_s, f) = I(V_{max})V_{max}/P_{inc} = m(vx_g/x_c)v(x_g, x_c, f)u(x_g)t_s \qquad [A.25]$$

A.2 Detailed Balance Limit of Efficiency of Tandem Solar Cells by de Vos

The original derivation of the detailed balance limit for a tandem stack of solar cells by de Vos [8] is briefly reproduced here. De Vos assumed all n cells to have the same temperature T_c, so that the I-V characteristic for the ith cell, in accordance with [A.12], is:

$$I = I_{1i} + I_{0i}[1 - \exp(V_i/V_c)]\,, \qquad [A.26]$$

where the short circuit current I_{1i} and saturation current I_{0i} are given by:

$$\begin{gathered} I_{0i} = qF_{c0i} = A_p f_\omega t_S Q_{Si}, \\ I_{1i} \equiv q(F_{Si} - F_{c0i}) \end{gathered} \qquad [A.27]$$

where Q_{Si} is the integral [A.2] evaluated with lower limit ν_{gi}, with $E_{gi} = h\nu_{gi}$ being the bandgap energy of cell i. The cells $i = 2,3,\ldots,n-1$ will have incident flux:

$$F_{Si} = A\exp\left(\frac{V_{i-1}}{V_c}\right)Q_{c(i-1)} + A\exp\left(\frac{V_{i+1}}{V_c}\right)Q_{c(i+1)} + Af_\omega\frac{2\pi}{c^2}\int_{\nu_{gi}}^{\nu_{g(i-1)}}[\exp(h\nu/k_BT_s) - 1]^{-1}\,\nu^2 d\nu \qquad [A.28]$$

where Q_{ci} is the integral [A.6] evaluated with lower limit ν_{gi}. The above terms respectively correspond to light emitted by the cells above and below cell i, and illumination by the part of the solar spectrum that has not been absorbed by the cells above it. The top cell $i = 0$ will be illuminated by the sun and by the cell below it, so will have incident photon flux:

$$F_{S1} = Af_\omega Q_{Si} + A\exp\left(\frac{V_2}{V_c}\right)Q_{c2} \qquad [A.29]$$

The bottom cell does not have a cell below it, so has flux:

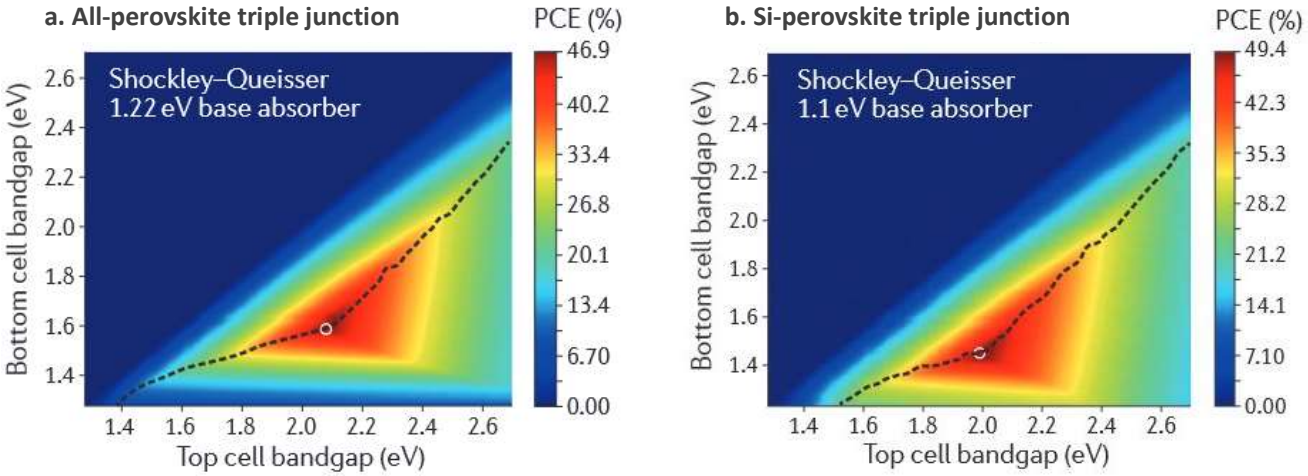
$$F_{S1} = A\exp\left(\frac{V_{n-1}}{V_c}\right)Q_{c(n-1)} + Af_\omega \frac{2\pi}{c^2}\int_{\nu_{gn}}^{\nu_{g(n-1)}} [\exp(h\nu/k_B T_s) - 1]^{-1}\,\nu^2 d\nu \qquad [A.30]$$

The total electrical power of the stack is given by:

$$P = -\sum_{i=1}^{n} V_i I_i \qquad [A.31]$$

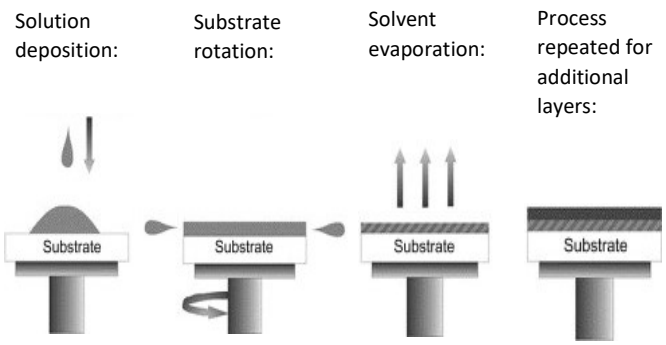
Maximising [A.31] by setting $\partial P/\partial V_i = 0$, one obtains a set of equations whose solutions determine the working points (V_i, I_i) which deliver the maximum power from the stack. From these, one may calculate the maximum efficiency as a function of the cell bandgap energies.

A.3 Calculated Shockley-Queisser Limits for Triple Junction Solar Cells

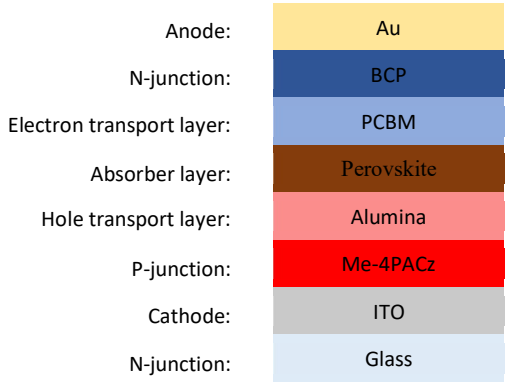


Maximum efficiency limits for tandem structures. Theoretical maximum PCE as a function of top and bottom cell bandgap energy for: (a) 1.22 eV base absorber triple junction and (b) 1.1 eV base absorber triple junction architectures. The dashed line traces peak efficiency for the displayed range of top and bottom bandgap energies. The white circles indicate maximum PCE. Both figures are reproduced from ref [2]

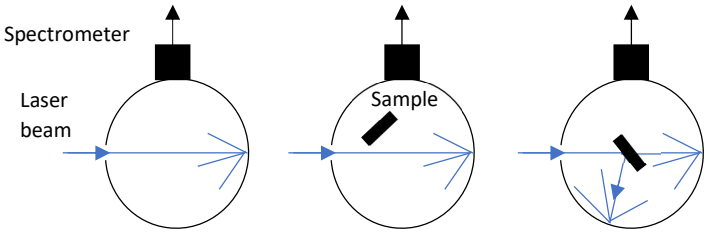
(i) Spin coating of thin films



(ii) Device architecture

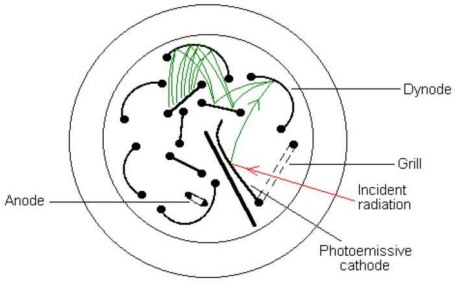


(iii) PLQE integrating sphere set-up



(i) Empty configuration **(ii) Sample out measurement** **(iii) Sample in measurement**

(iv) Cross-section of photomultiplier tube



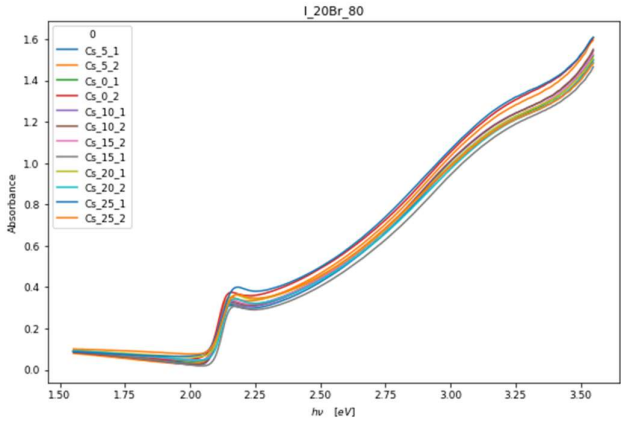
Experimental methods. (i): The solution may be deposited statically, where the substrate is still, or dynamically, where the substrate is spinning while the solution is applied. The centrifugal force due to the rotation of the chuck spreads the solution uniformly across the substrate. A vacuum below the chuck is used to fix the substrate to the chuck. Figure reproduced from ref [34]. **(ii):** Device architecture **(iii):** PLQE measurements were taken in each of the three illustrated configurations. A reading was also taken with the laser beam turned off, to determine the background signal. **(iv):** Diagram illustrating the photomultiplier tube used for optical spectroscopy to detect light in the UV and visible spectral ranges.

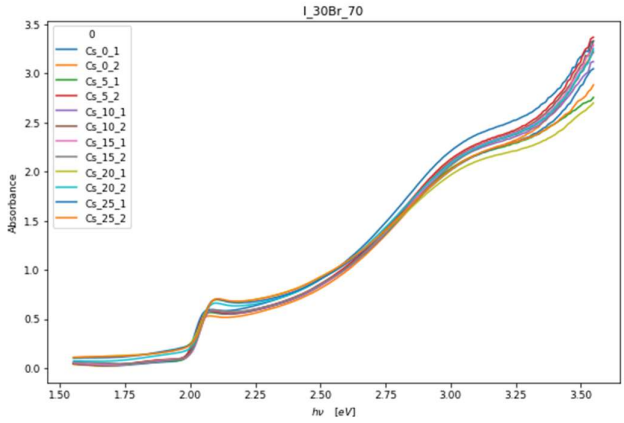
The photomultiplier consists of a photo-emissive cathode, a series of dynodes, and an anode, as illustrated in APPENDIX B.1(iv). The cathode emits electrons when struck by photons. These electrons strike a series of dynodes, which emit multiple electrons for each electron that strike them. The resulting current is thus amplified and eventually collected at the anode. The PbS detector works by utilizing the photoconductive effect, where exposure to infrared radiation causes the decrease of the resistance of the active area of the PbS semiconductor as a function of the incident radiation intensity.

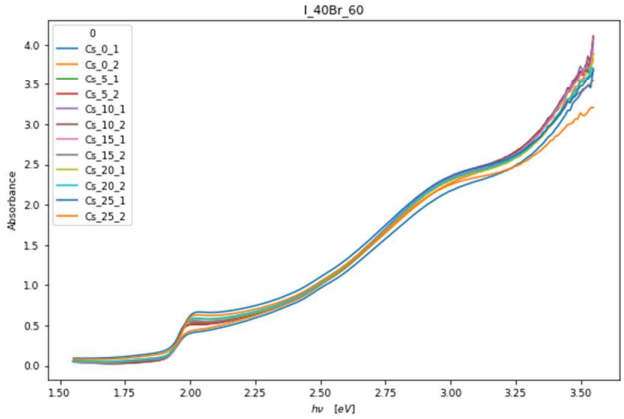
C.1 Optical absorption properties

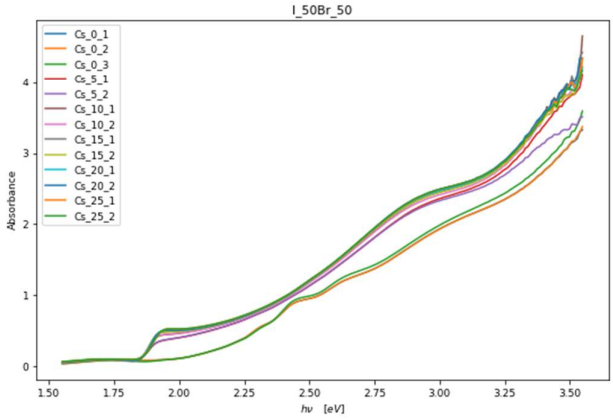
Naming convention: I_30Br_70_2 is set 2 of samples with compositions that have a Br content of 70%, Cs_5_1 is sample 1 of compositions with 5% Cs for a given Br content.

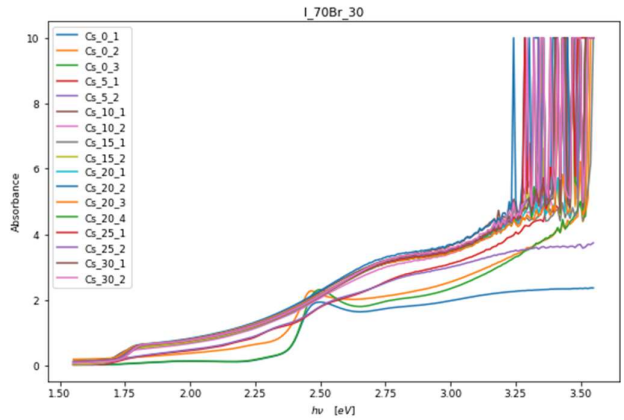
C.1(i): Absorbance Plots

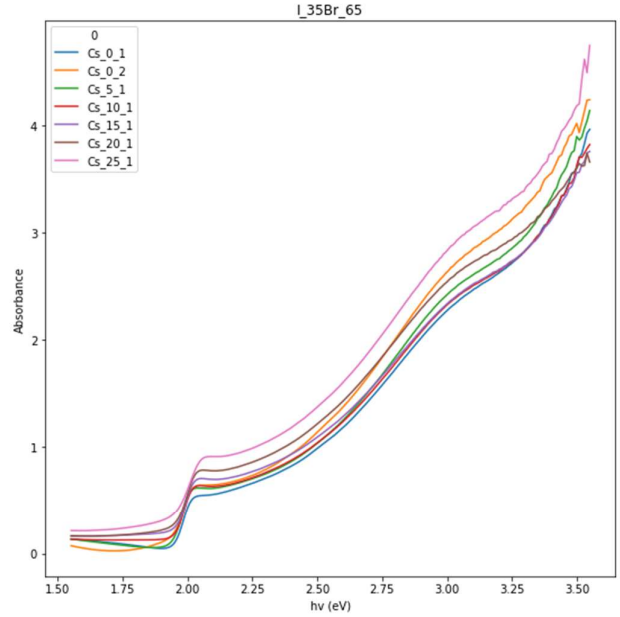


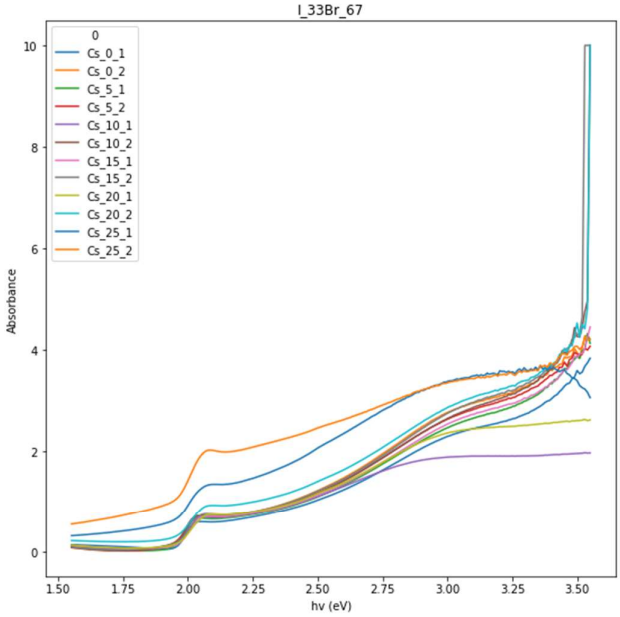


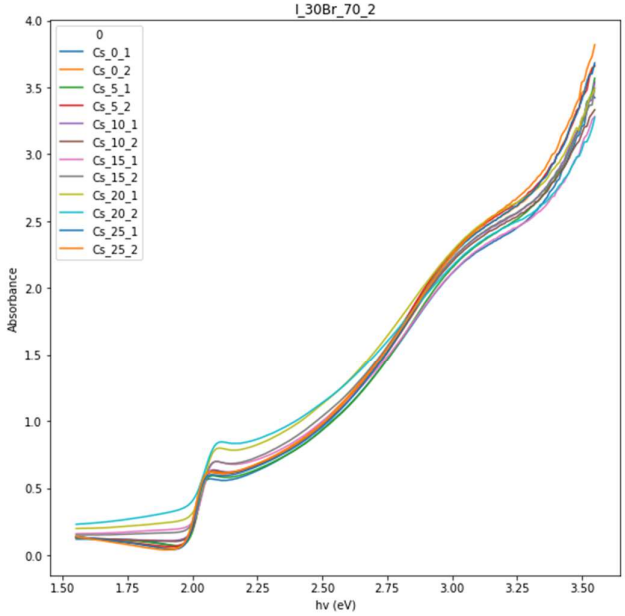


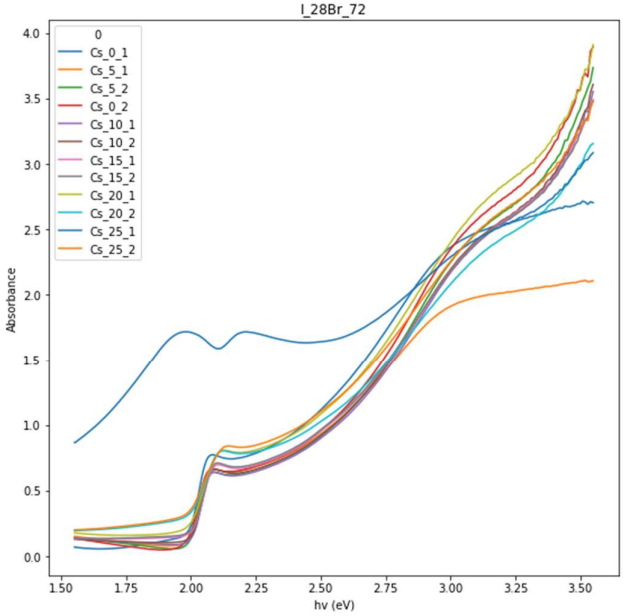




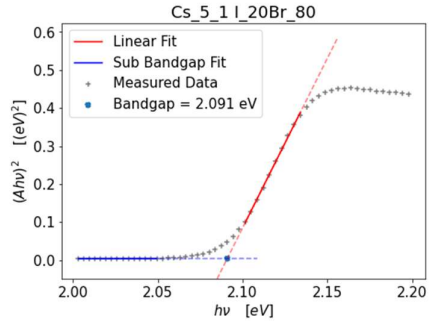

I_35Br_65
0
Cs_0_1
Cs_0_2
Cs_5_1
Cs_10_1
Cs_15_1
Cs_20_1
Cs_25_1
Absorbance
hv (eV)

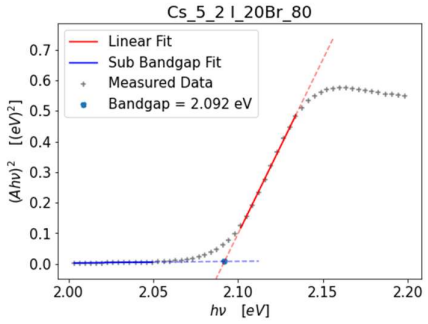

I_33Br_67
0
Cs_0_1
Cs_0_2
Cs_5_1
Cs_5_2
Cs_10_1
Cs_10_2
Cs_15_1
Cs_15_2
Cs_20_1
Cs_20_2
Cs_25_1
Cs_25_2
Absorbance
hv (eV)

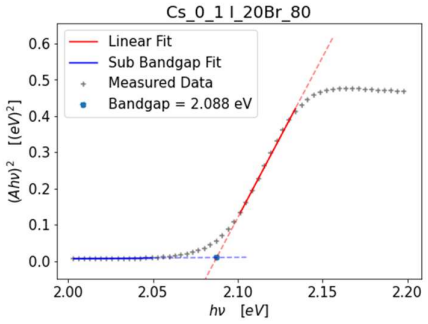

I_30Br_70_2
0
Cs_0_1
Cs_0_2
Cs_5_1
Cs_5_2
Cs_10_1
Cs_10_2
Cs_15_1
Cs_15_2
Cs_20_1
Cs_20_2
Cs_25_1
Cs_25_2
Absorbance
hv (eV)

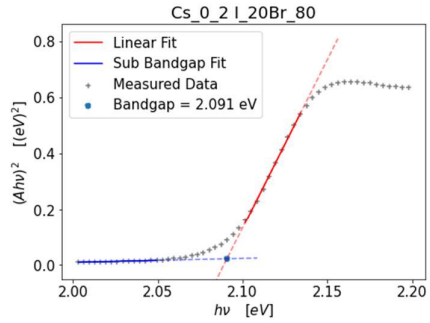

I_28Br_72
0
Cs_0_1
Cs_5_1
Cs_5_2
Cs_0_2
Cs_10_1
Cs_10_2
Cs_15_1
Cs_15_2
Cs_20_1
Cs_20_2
Cs_25_1
Cs_25_2
Absorbance
hv (eV)

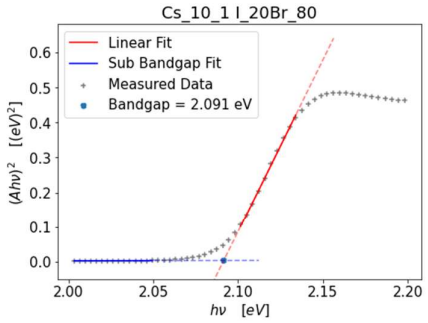
C.1(ii) Tauc Plots with Linear Fit:

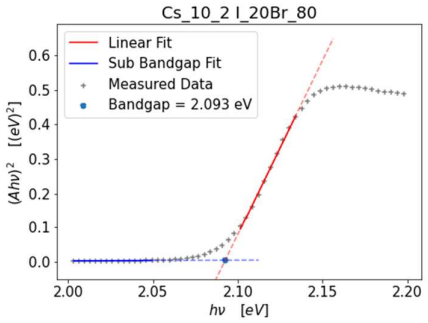


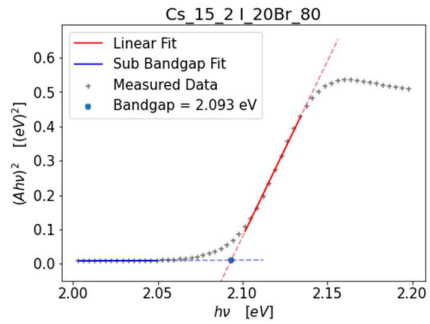


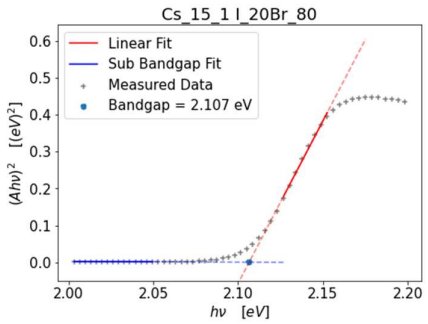


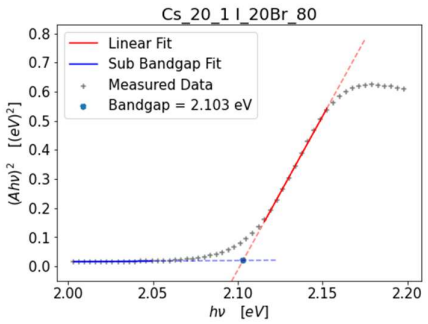


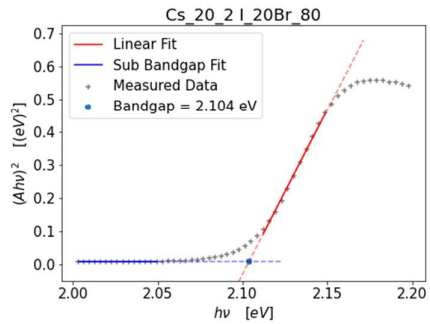


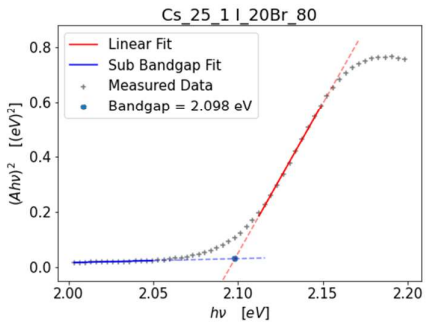


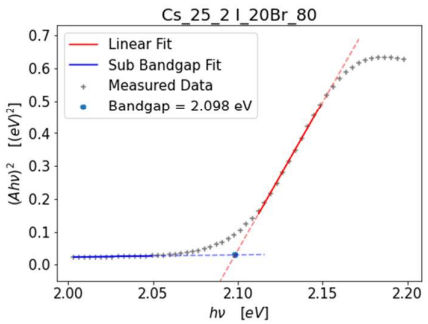


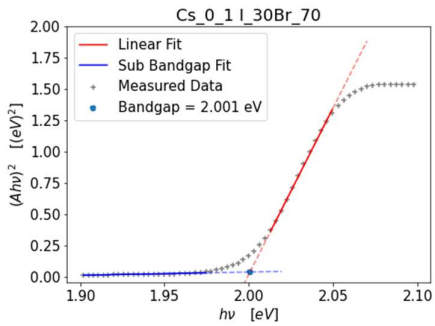


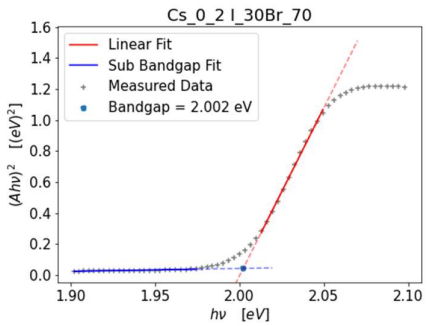


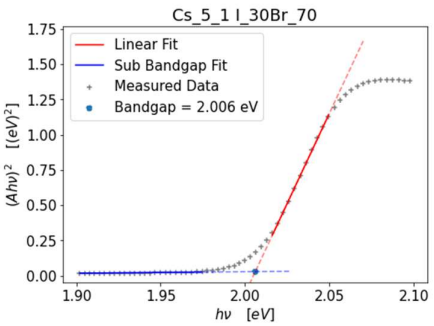


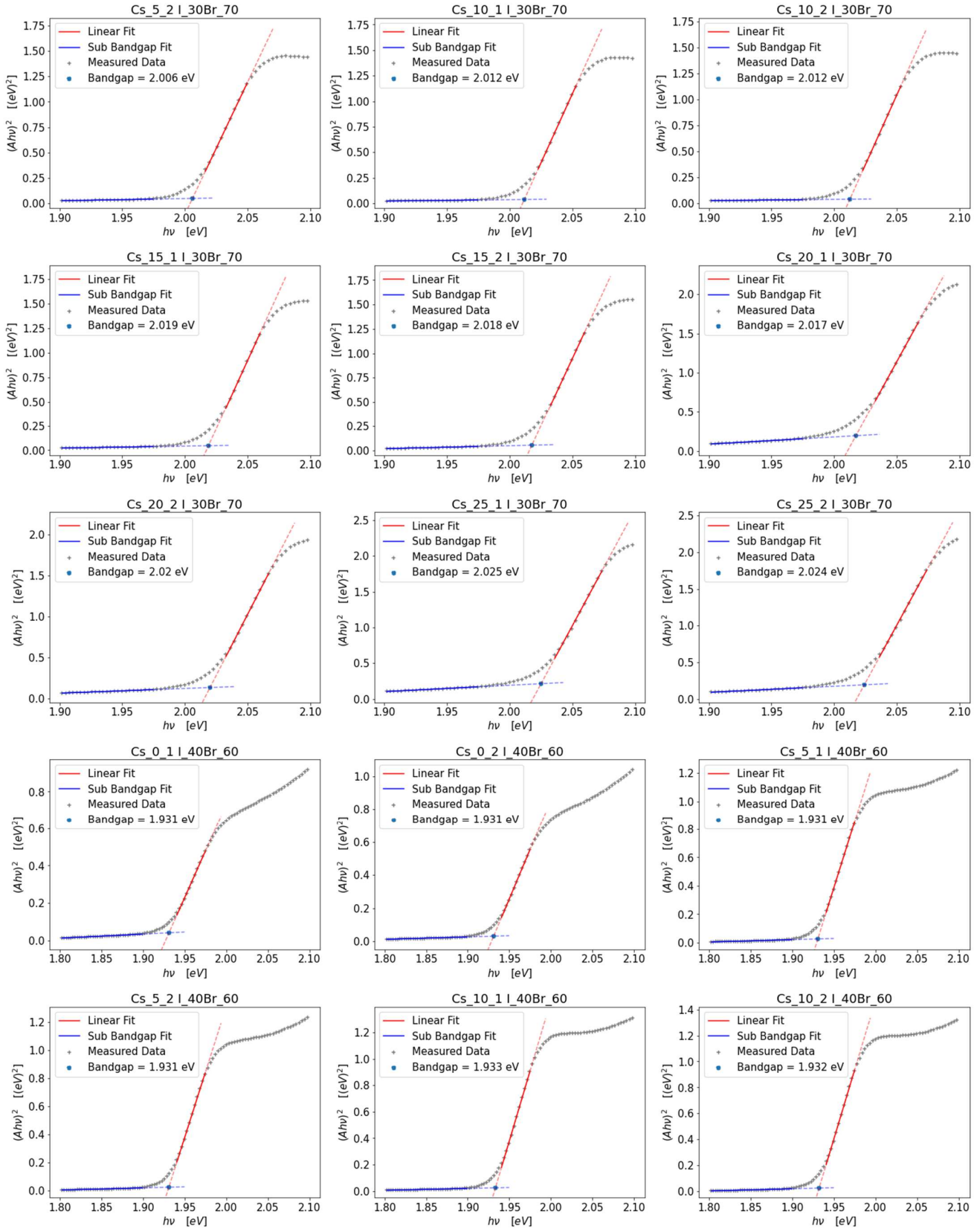


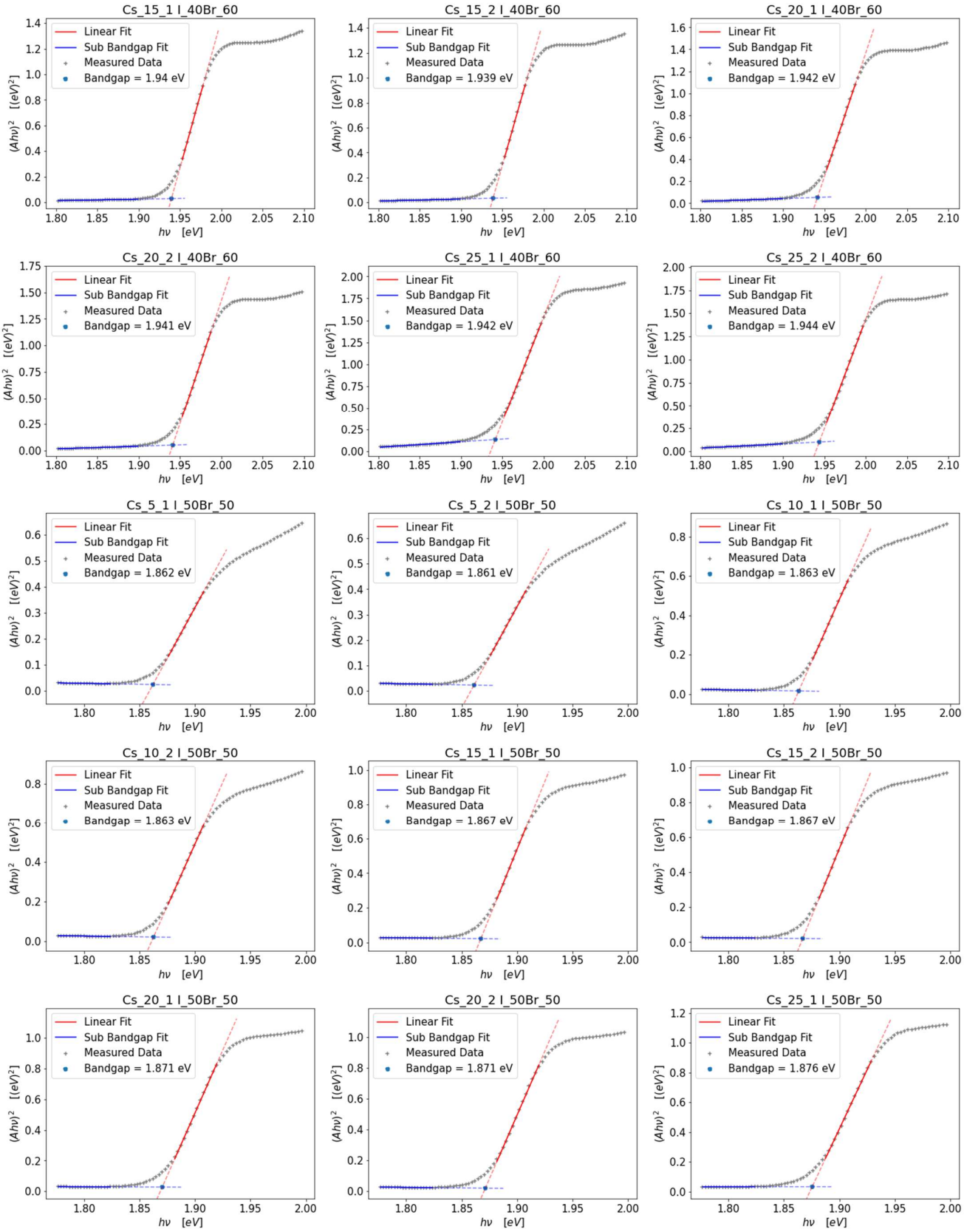


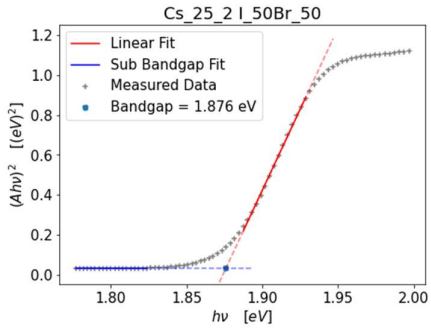


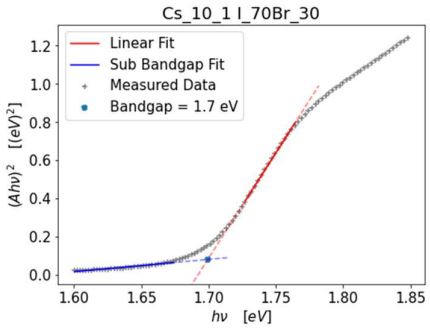


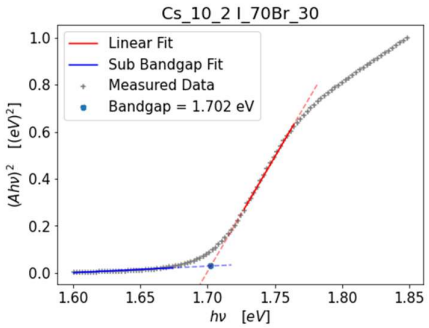


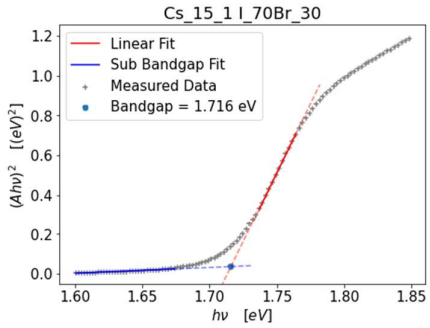

Cs_5_2 I_30Br_70
Linear Fit
Sub Bandgap Fit
Measured Data
Bandgap = 2.006 eV
Cs_10_1 I_30Br_70
Bandgap = 2.012 eV
Cs_10_2 I_30Br_70
Bandgap = 2.012 eV
Cs_15_1 I_30Br_70
Bandgap = 2.019 eV
Cs_15_2 I_30Br_70
Bandgap = 2.018 eV
Cs_20_1 I_30Br_70
Bandgap = 2.017 eV
Cs_20_2 I_30Br_70
Bandgap = 2.02 eV
Cs_25_1 I_30Br_70
Bandgap = 2.025 eV
Cs_25_2 I_30Br_70
Bandgap = 2.024 eV
Cs_0_1 I_40Br_60
Bandgap = 1.931 eV
Cs_0_2 I_40Br_60
Bandgap = 1.931 eV
Cs_5_1 I_40Br_60
Bandgap = 1.931 eV
Cs_5_2 I_40Br_60
Bandgap = 1.931 eV
Cs_10_1 I_40Br_60
Bandgap = 1.933 eV
Cs_10_2 I_40Br_60
Bandgap = 1.932 eV
(Ahν)² [(eV)²]
hν [eV]

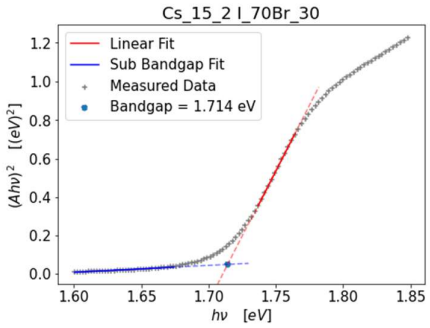

Cs_15_1 I_40Br_60
Linear Fit
Sub Bandgap Fit
Measured Data
Bandgap = 1.94 eV
Cs_15_2 I_40Br_60
Bandgap = 1.939 eV
Cs_20_1 I_40Br_60
Bandgap = 1.942 eV
Cs_20_2 I_40Br_60
Bandgap = 1.941 eV
Cs_25_1 I_40Br_60
Bandgap = 1.942 eV
Cs_25_2 I_40Br_60
Bandgap = 1.944 eV
Cs_5_1 I_50Br_50
Bandgap = 1.862 eV
Cs_5_2 I_50Br_50
Bandgap = 1.861 eV
Cs_10_1 I_50Br_50
Bandgap = 1.863 eV
Cs_10_2 I_50Br_50
Bandgap = 1.863 eV
Cs_15_1 I_50Br_50
Bandgap = 1.867 eV
Cs_15_2 I_50Br_50
Bandgap = 1.867 eV
Cs_20_1 I_50Br_50
Bandgap = 1.871 eV
Cs_20_2 I_50Br_50
Bandgap = 1.871 eV
Cs_25_1 I_50Br_50
Bandgap = 1.876 eV
(Ahν)² [(eV)²]
hν [eV]

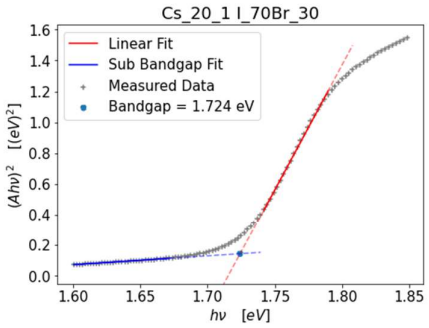

Cs_25_2 I_50Br_50
Linear Fit
Sub Bandgap Fit
Measured Data
Bandgap = 1.876 eV
$(Ahν)^2$ [(eV)^2]
hν [eV]

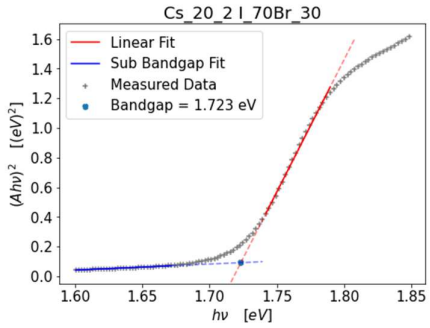

Cs_10_1 I_70Br_30
Linear Fit
Sub Bandgap Fit
Measured Data
Bandgap = 1.7 eV
$(Ahν)^2$ [(eV)^2]
hν [eV]

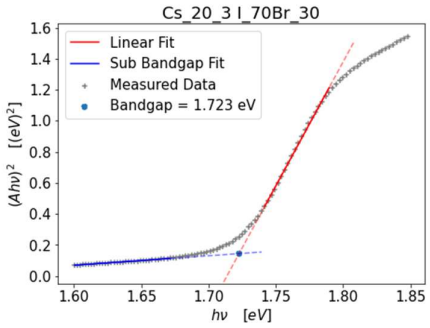

Cs_10_2 I_70Br_30
Linear Fit
Sub Bandgap Fit
Measured Data
Bandgap = 1.702 eV
$(Ahν)^2$ [(eV)^2]
hν [eV]

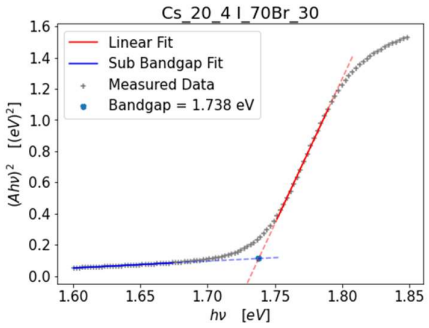

Cs_15_1 I_70Br_30
Linear Fit
Sub Bandgap Fit
Measured Data
Bandgap = 1.716 eV
$(Ahν)^2$ [(eV)^2]
hν [eV]

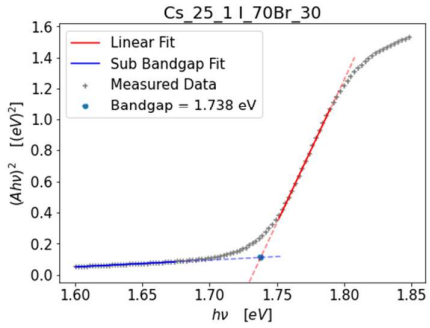

Cs_15_2 I_70Br_30
Linear Fit
Sub Bandgap Fit
Measured Data
Bandgap = 1.714 eV
$(Ahν)^2$ [(eV)^2]
hν [eV]

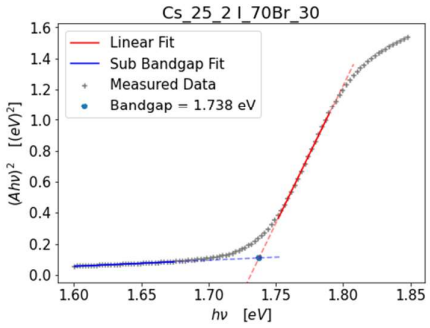

Cs_20_1 I_70Br_30
Linear Fit
Sub Bandgap Fit
Measured Data
Bandgap = 1.724 eV
$(Ahν)^2$ [(eV)^2]
hν [eV]

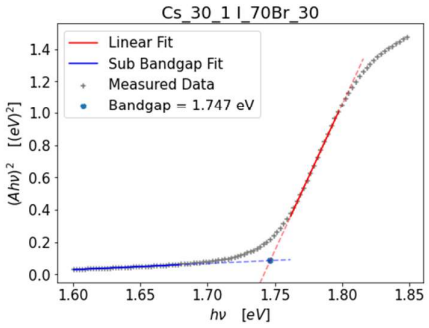

Cs_20_2 I_70Br_30
Linear Fit
Sub Bandgap Fit
Measured Data
Bandgap = 1.723 eV
$(Ahν)^2$ [(eV)^2]
hν [eV]

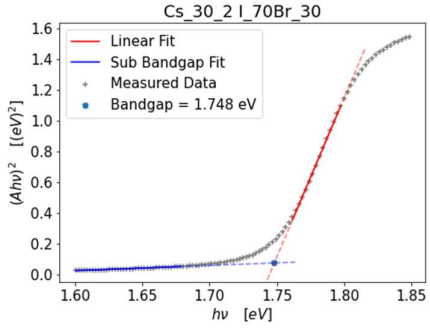

Cs_20_3 I_70Br_30
Linear Fit
Sub Bandgap Fit
Measured Data
Bandgap = 1.723 eV
$(Ahν)^2$ [(eV)^2]
hν [eV]

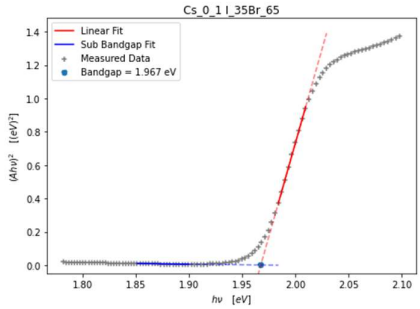

Cs_20_4 I_70Br_30
Linear Fit
Sub Bandgap Fit
Measured Data
Bandgap = 1.738 eV
$(Ahν)^2$ [(eV)^2]
hν [eV]

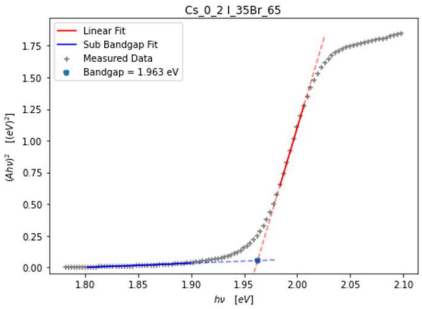

Cs_25_1 I_70Br_30
Linear Fit
Sub Bandgap Fit
Measured Data
Bandgap = 1.738 eV
$(Ahν)^2$ [(eV)^2]
hν [eV]

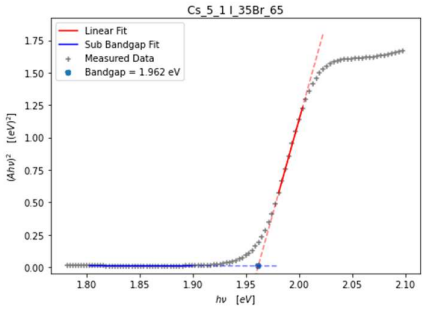

Cs_25_2 I_70Br_30
Linear Fit
Sub Bandgap Fit
Measured Data
Bandgap = 1.738 eV
$(Ahν)^2$ [(eV)^2]
hν [eV]

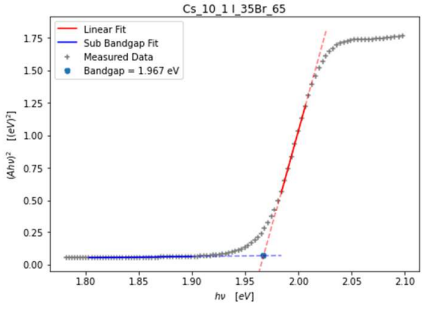

Cs_30_1 I_70Br_30
Linear Fit
Sub Bandgap Fit
Measured Data
Bandgap = 1.747 eV
$(Ahν)^2$ [(eV)^2]
hν [eV]

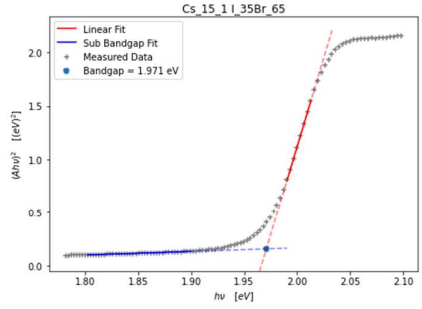

Cs_30_2 I_70Br_30
Linear Fit
Sub Bandgap Fit
Measured Data
Bandgap = 1.748 eV
$(Ahν)^2$ [(eV)^2]
hν [eV]

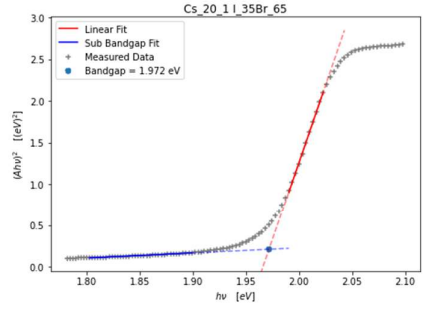

Cs_0_1 I_35Br_65
Linear Fit
Sub Bandgap Fit
Measured Data
Bandgap = 1.967 eV
(Ahν)² [(eV)²]
hν [eV]

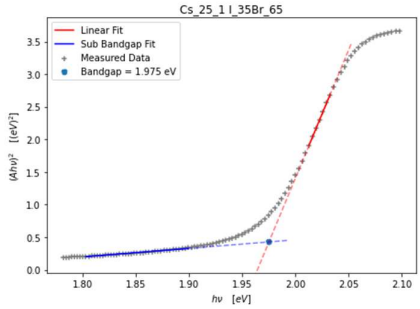

Cs_0_2 I_35Br_65
Linear Fit
Sub Bandgap Fit
Measured Data
Bandgap = 1.963 eV
(Ahν)² [(eV)²]
hν [eV]

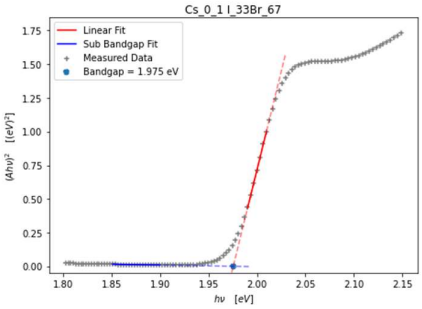

Cs_5_1 I_35Br_65
Linear Fit
Sub Bandgap Fit
Measured Data
Bandgap = 1.962 eV
(Ahν)² [(eV)²]
hν [eV]

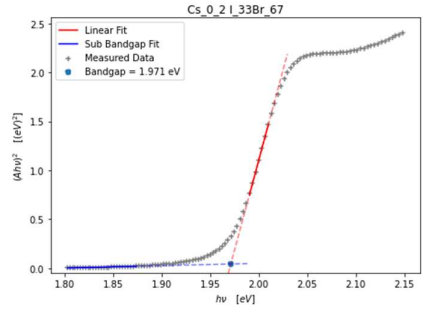

Cs_10_1 I_35Br_65
Linear Fit
Sub Bandgap Fit
Measured Data
Bandgap = 1.967 eV
(Ahν)² [(eV)²]
hν [eV]

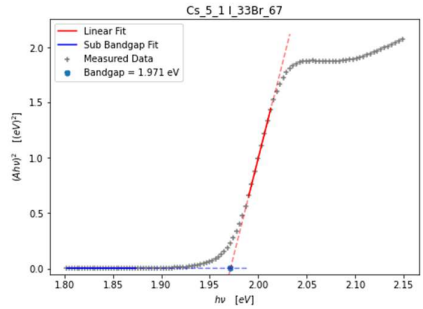

Cs_15_1 I_35Br_65
Linear Fit
Sub Bandgap Fit
Measured Data
Bandgap = 1.971 eV
(Ahν)² [(eV)²]
hν [eV]

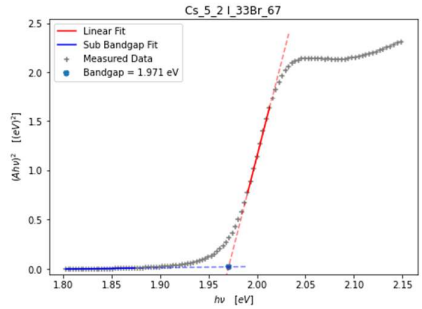

Cs_20_1 I_35Br_65
Linear Fit
Sub Bandgap Fit
Measured Data
Bandgap = 1.972 eV
(Ahν)² [(eV)²]
hν [eV]

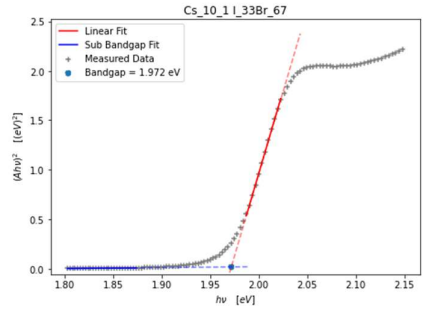

Cs_25_1 I_35Br_65
Linear Fit
Sub Bandgap Fit
Measured Data
Bandgap = 1.975 eV
(Ahν)² [(eV)²]
hν [eV]

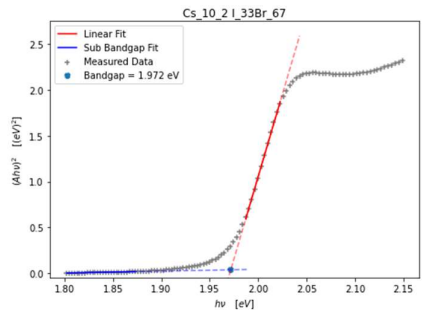

Cs_0_1 I_33Br_67
Linear Fit
Sub Bandgap Fit
Measured Data
Bandgap = 1.975 eV
(Ahν)² [(eV)²]
hν [eV]

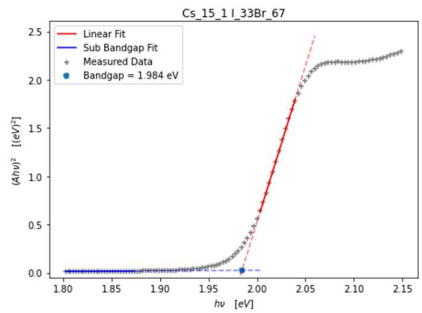

Cs_0_2 I_33Br_67
Linear Fit
Sub Bandgap Fit
Measured Data
Bandgap = 1.971 eV
(Ahν)² [(eV)²]
hν [eV]

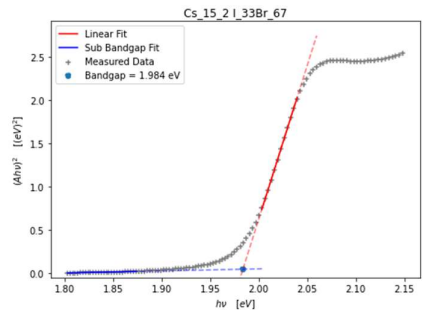

Cs_5_1 I_33Br_67
Linear Fit
Sub Bandgap Fit
Measured Data
Bandgap = 1.971 eV
(Ahν)² [(eV)²]
hν [eV]

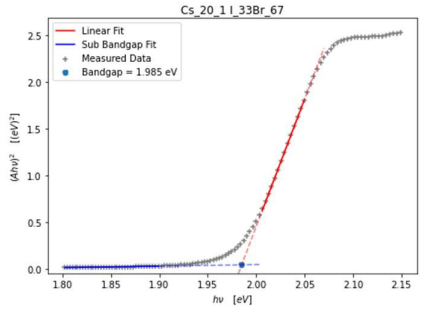

Cs_5_2 I_33Br_67
Linear Fit
Sub Bandgap Fit
Measured Data
Bandgap = 1.971 eV
(Ahν)² [(eV)²]
hν [eV]

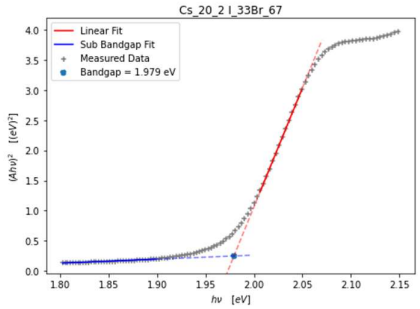

Cs_10_1 I_33Br_67
Linear Fit
Sub Bandgap Fit
Measured Data
Bandgap = 1.972 eV
(Ahν)² [(eV)²]
hν [eV]

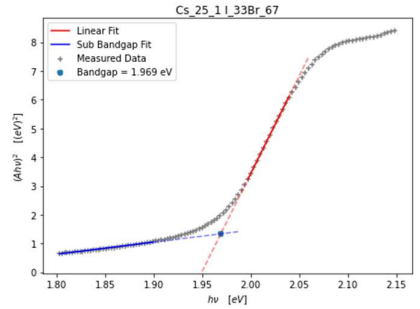

Cs_10_2 I_33Br_67
Linear Fit
Sub Bandgap Fit
Measured Data
Bandgap = 1.972 eV
(Ahν)² [(eV)²]
hν [eV]

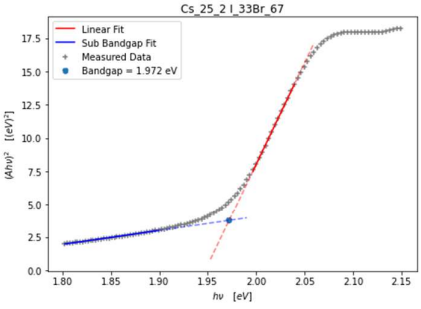

Cs_15_1 I_33Br_67
Linear Fit
Sub Bandgap Fit
Measured Data
Bandgap = 1.984 eV
(Ahν)² [(eV)²]
hν [eV]

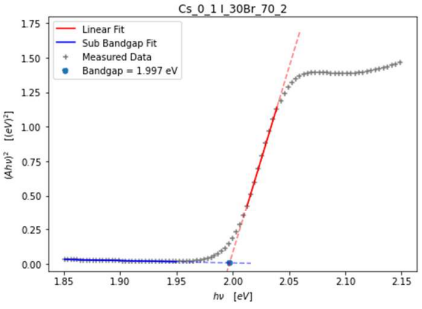

Cs_15_2 I_33Br_67
Linear Fit
Sub Bandgap Fit
Measured Data
Bandgap = 1.984 eV
(Ahν)² [(eV)²]
hν [eV]

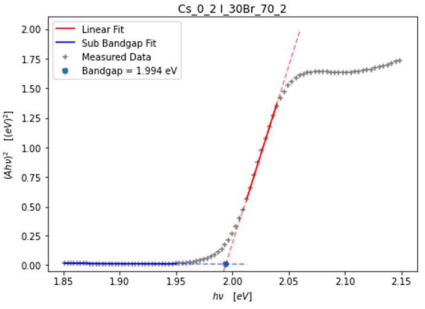

Cs_20_1 I_33Br_67
Linear Fit
Sub Bandgap Fit
Measured Data
Bandgap = 1.985 eV
(Ahν)² [(eV)²]
hν [eV]

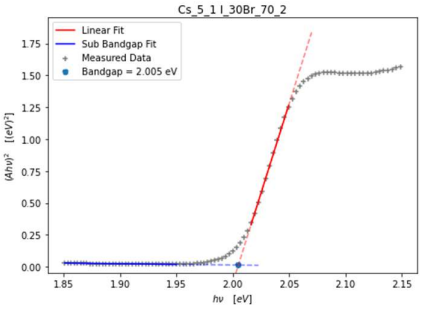

Cs_20_2 I_33Br_67
Linear Fit
Sub Bandgap Fit
Measured Data
Bandgap = 1.979 eV
(Ahν)² [(eV)²]
hν [eV]

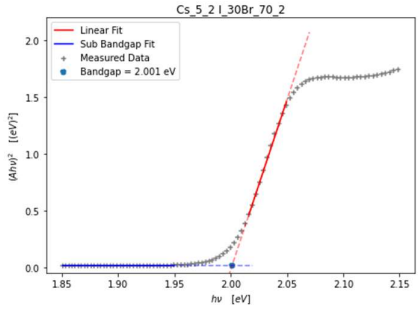

Cs_25_1 I_33Br_67
Linear Fit
Sub Bandgap Fit
Measured Data
Bandgap = 1.969 eV
(Ahν)² [(eV)²]
hν [eV]

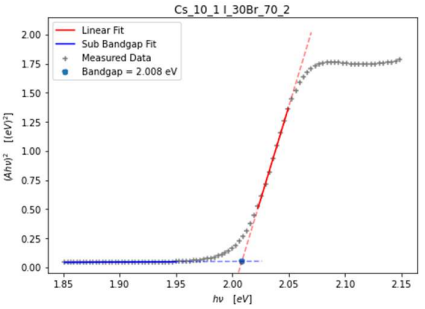

Cs_25_2 I_33Br_67
Linear Fit
Sub Bandgap Fit
Measured Data
Bandgap = 1.972 eV
(Ahν)² [(eV)²]
hν [eV]

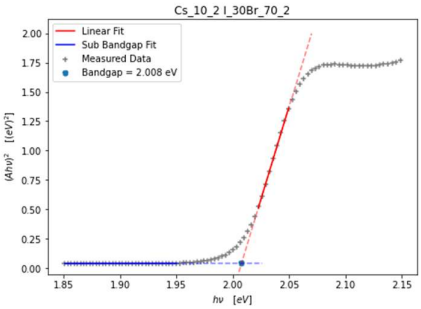

Cs_0_1 I_30Br_70_2
Linear Fit
Sub Bandgap Fit
Measured Data
Bandgap = 1.997 eV
(Ahν)² [(eV)²]
hν [eV]

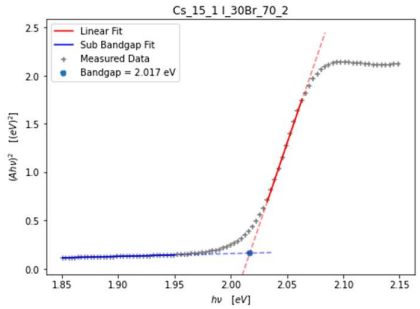

Cs_0_2 I_30Br_70_2
Linear Fit
Sub Bandgap Fit
Measured Data
Bandgap = 1.994 eV
(Ahν)² [(eV)²]
hν [eV]

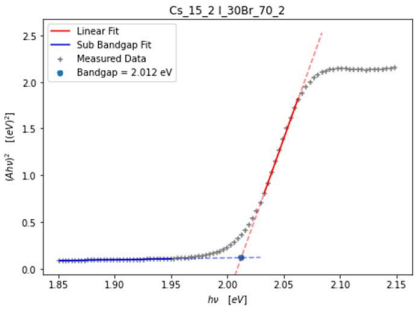

Cs_5_1 I_30Br_70_2
Linear Fit
Sub Bandgap Fit
Measured Data
Bandgap = 2.005 eV
(Ahν)² [(eV)²]
hν [eV]

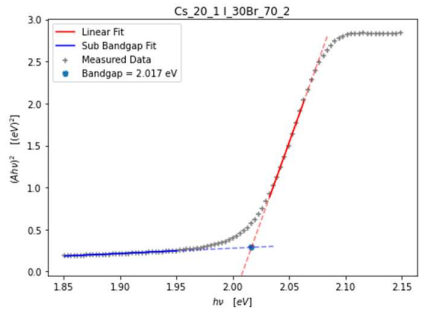

Cs_5_2 I_30Br_70_2
Linear Fit
Sub Bandgap Fit
Measured Data
Bandgap = 2.001 eV
(Ahν)² [(eV)²]
hν [eV]

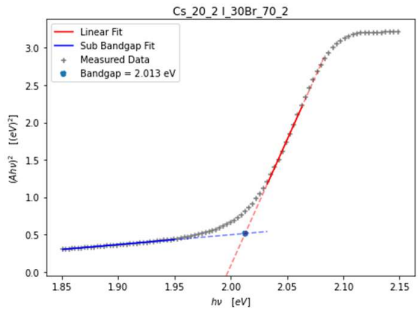

Cs_10_1 I_30Br_70_2
Linear Fit
Sub Bandgap Fit
Measured Data
Bandgap = 2.008 eV
(Ahν)² [(eV)²]
hν [eV]

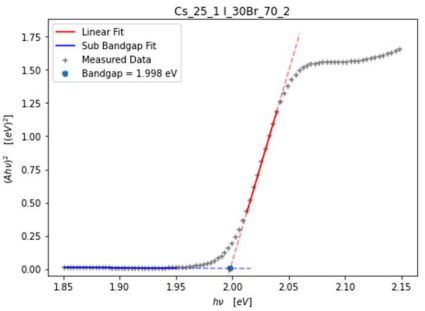

Cs_10_2 I_30Br_70_2
Linear Fit
Sub Bandgap Fit
Measured Data
Bandgap = 2.008 eV
(Ahν)² [(eV)²]
hν [eV]

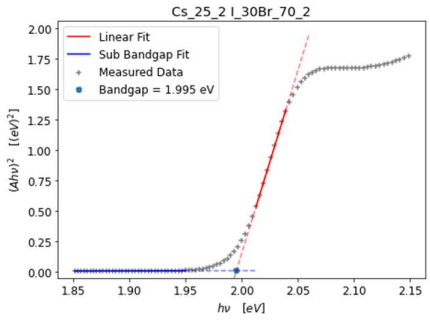

Cs_15_1 I_30Br_70_2
Linear Fit
Sub Bandgap Fit
Measured Data
Bandgap = 2.017 eV
(Ahν)² [(eV)²]
hν [eV]

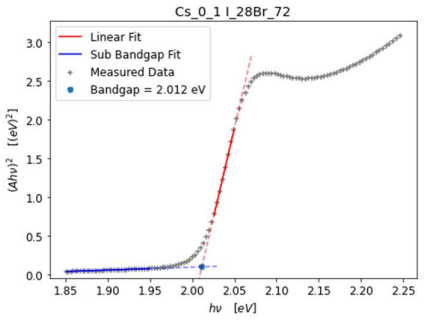

Cs_15_2 I_30Br_70_2
Linear Fit
Sub Bandgap Fit
Measured Data
Bandgap = 2.012 eV
(Ahν)² [(eV)²]
hν [eV]

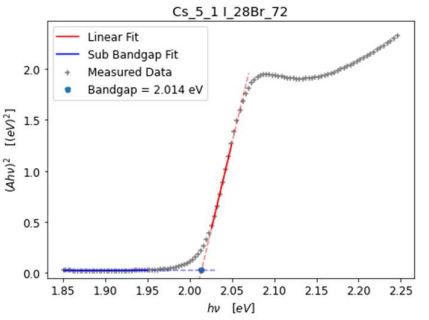

Cs_20_1 I_30Br_70_2
Linear Fit
Sub Bandgap Fit
Measured Data
Bandgap = 2.017 eV
(Ahν)² [(eV)²]
hν [eV]

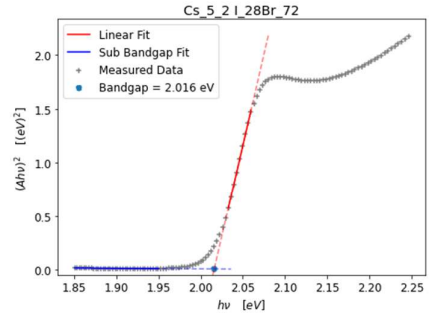

Cs_20_2 I_30Br_70_2
Linear Fit
Sub Bandgap Fit
Measured Data
Bandgap = 2.013 eV
(Ahν)² [(eV)²]
hν [eV]

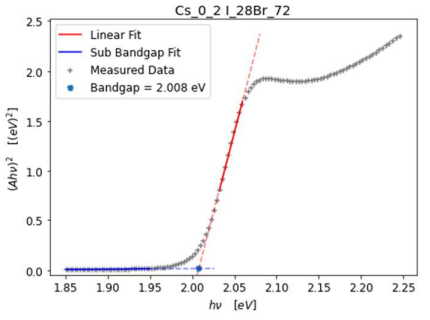

Cs_25_1 I_30Br_70_2
Linear Fit
Sub Bandgap Fit
Measured Data
Bandgap = 1.998 eV
(Ahν)² [(eV)²]
hν [eV]

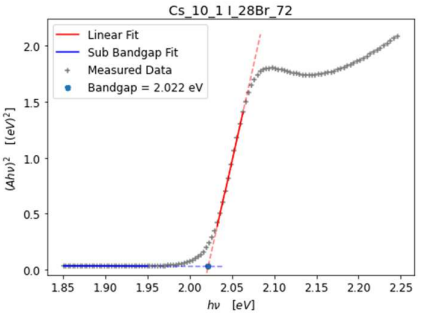

Cs_25_2 I_30Br_70_2
Linear Fit
Sub Bandgap Fit
Measured Data
Bandgap = 1.995 eV
(Ahν)² [(eV)²]
hν [eV]

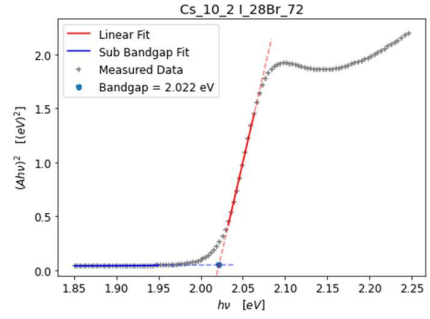

Cs_0_1 I_28Br_72
Linear Fit
Sub Bandgap Fit
Measured Data
Bandgap = 2.012 eV
(Ahν)² [(eV)²]
hν [eV]

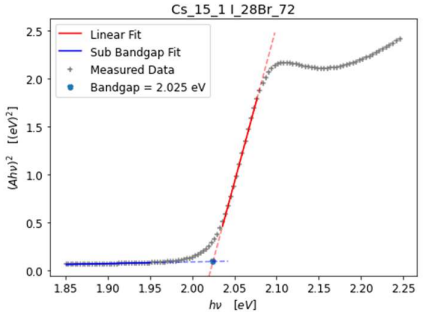

Cs_5_1 I_28Br_72
Linear Fit
Sub Bandgap Fit
Measured Data
Bandgap = 2.014 eV
(Ahν)² [(eV)²]
hν [eV]

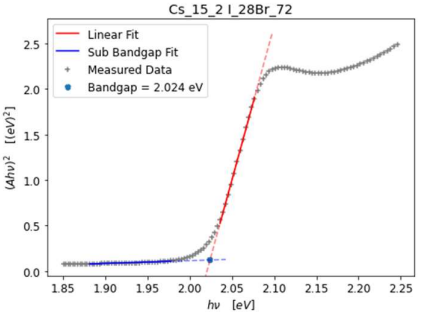

Cs_5_2 I_28Br_72
Linear Fit
Sub Bandgap Fit
Measured Data
Bandgap = 2.016 eV
(Ahν)² [(eV)²]
hν [eV]

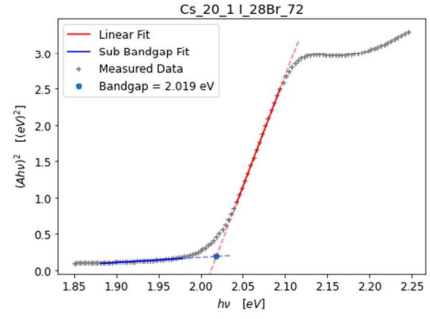

Cs_0_2 I_28Br_72
Linear Fit
Sub Bandgap Fit
Measured Data
Bandgap = 2.008 eV
(Ahν)² [(eV)²]
hν [eV]

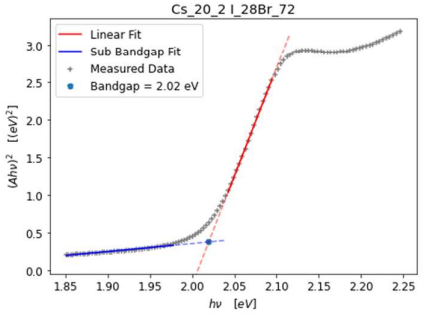

Cs_10_1 I_28Br_72
Linear Fit
Sub Bandgap Fit
Measured Data
Bandgap = 2.022 eV
(Ahν)² [(eV)²]
hν [eV]

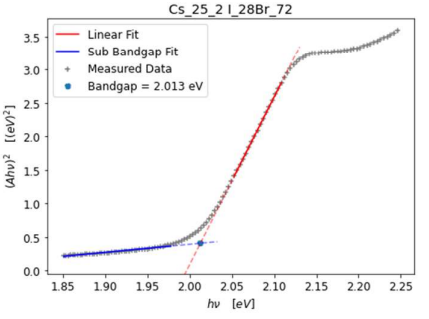

Cs_10_2 I_28Br_72
Linear Fit
Sub Bandgap Fit
Measured Data
Bandgap = 2.022 eV
(Ahν)² [(eV)²]
hν [eV]


Cs_15_1 I_28Br_72
Linear Fit
Sub Bandgap Fit
Measured Data
Bandgap = 2.025 eV
(Ahν)² [(eV)²]
hν [eV]


Cs_15_2 I_28Br_72
Linear Fit
Sub Bandgap Fit
Measured Data
Bandgap = 2.024 eV
(Ahν)² [(eV)²]
hν [eV]

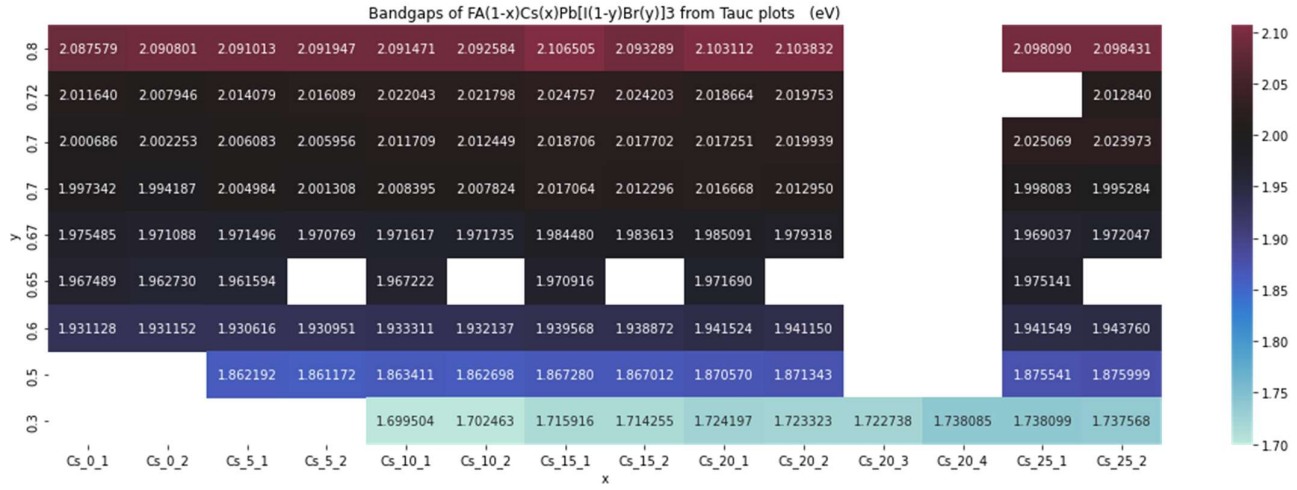

Cs_20_1 I_28Br_72
Linear Fit
Sub Bandgap Fit
Measured Data
Bandgap = 2.019 eV
(Ahν)² [(eV)²]
hν [eV]


Cs_20_2 I_28Br_72
Linear Fit
Sub Bandgap Fit
Measured Data
Bandgap = 2.02 eV
(Ahν)² [(eV)²]
hν [eV]

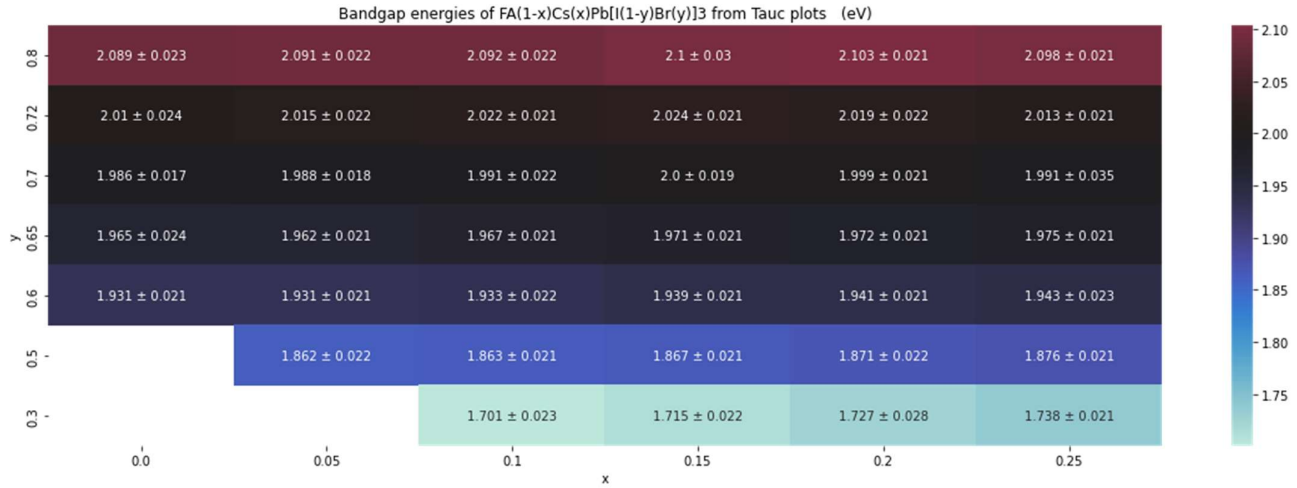

Cs_25_2 I_28Br_72
Linear Fit
Sub Bandgap Fit
Measured Data
Bandgap = 2.013 eV
(Ahν)² [(eV)²]
hν [eV]

C.1(iii) Bandgaps inferred from Tauc plots:

Bandgaps for all samples:

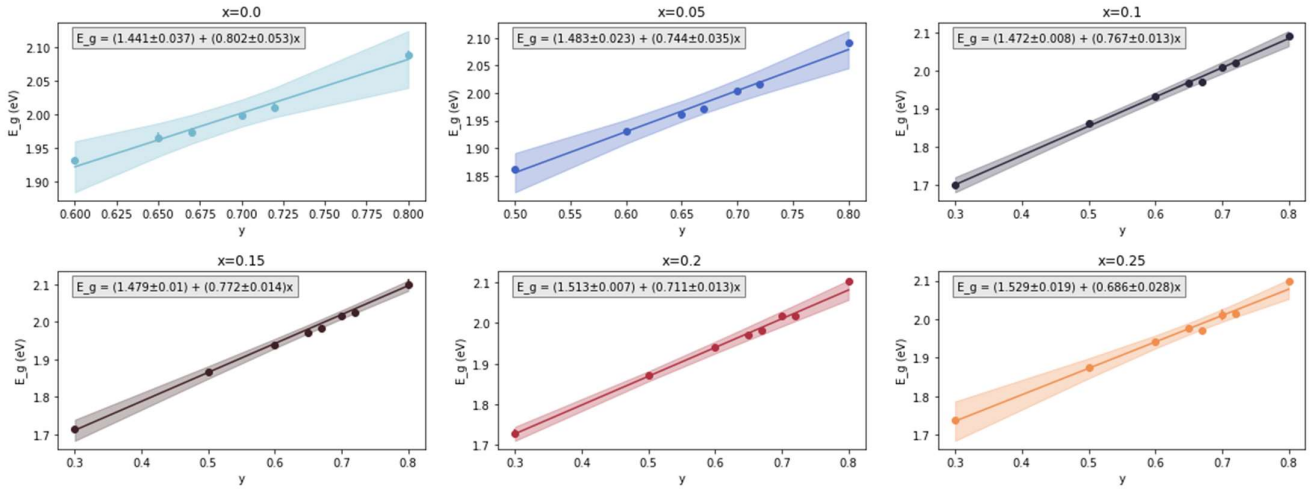


Average bandgaps with estimated uncertainties:

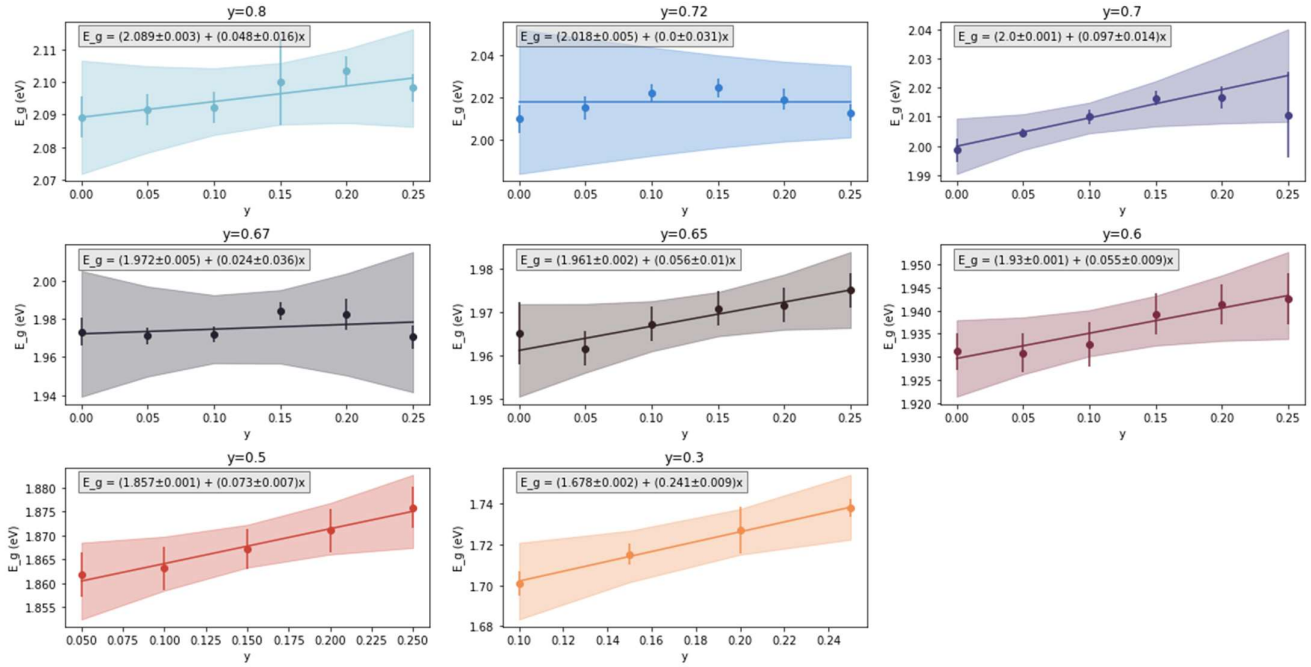


C.1(iv) Bandgap energy variation over compositional space:

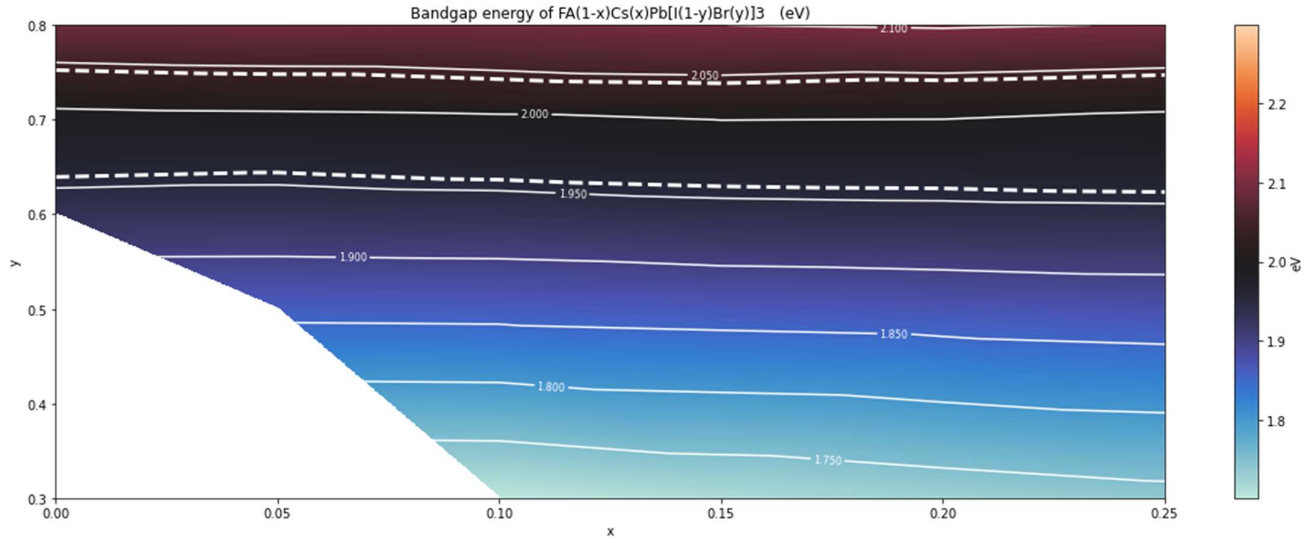
Variation with Br content:



Variation with Cs content:



C.1(v) Linear Interpolation of bandgaps inferred from Tauc plots:



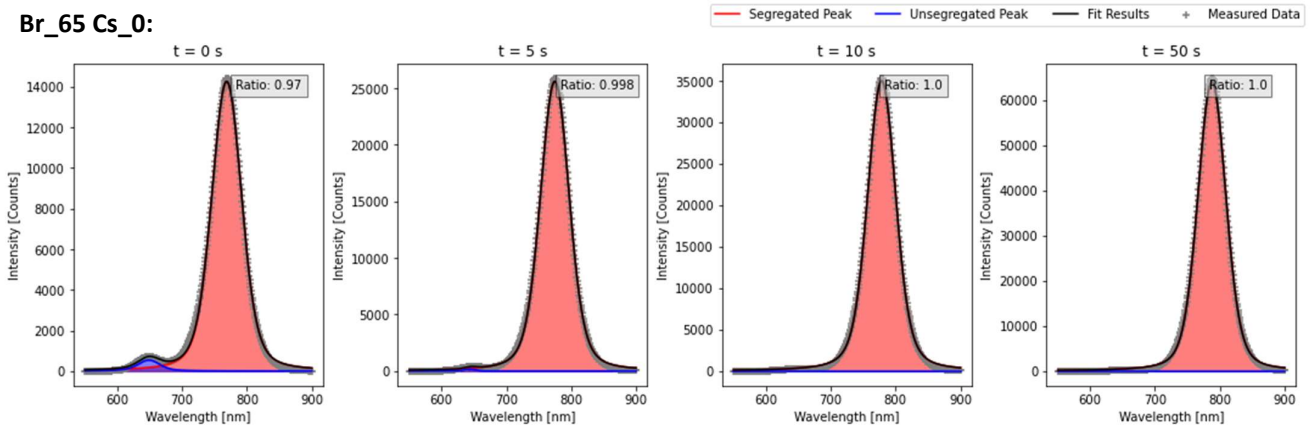
:

C.2 PLQE properties

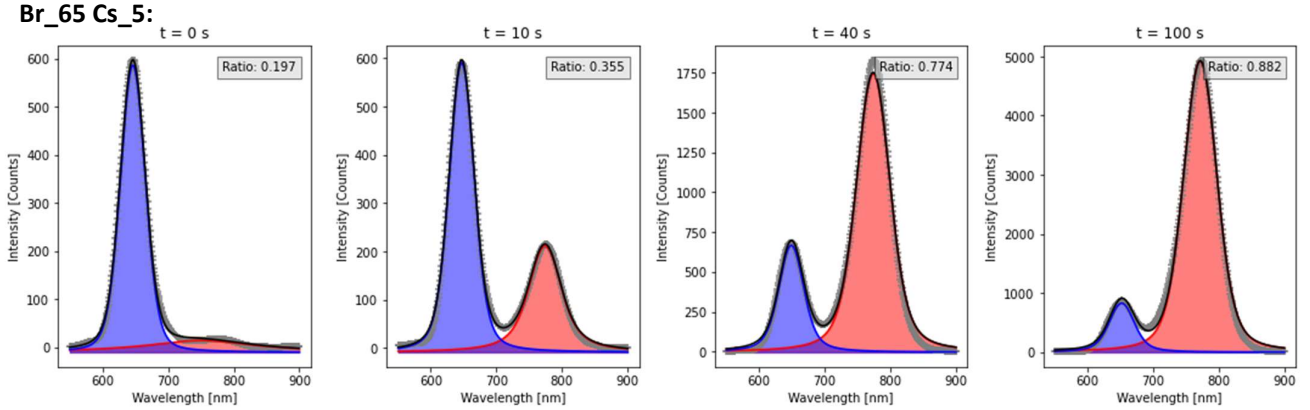
C.2(i) Time evolution of PL spectra:

Data was fitted to a curve of the form: $y = y_0 + A_1 f(x_1, \sigma_1, \lambda_1) + A_2 f(x_2, \sigma_2, \lambda_2)$, where f is the Voigt profile

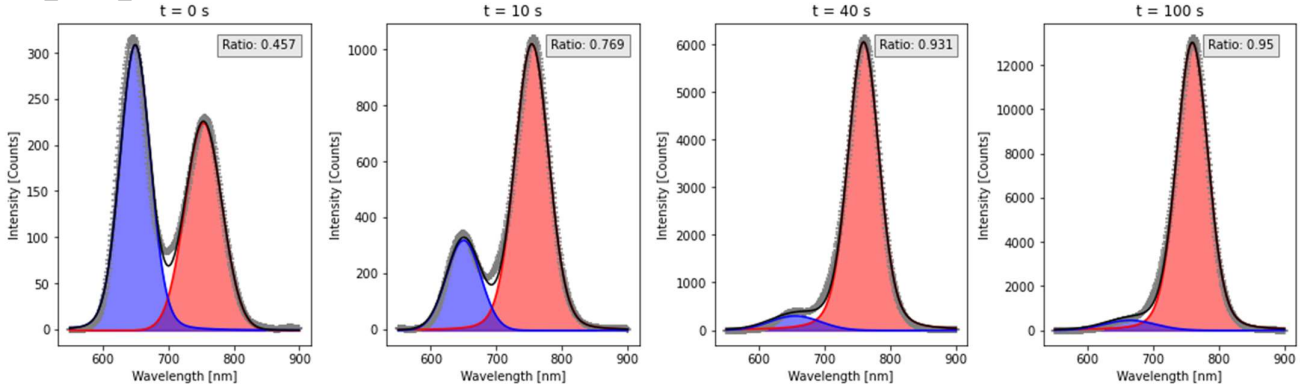
Br_65 Cs_0:



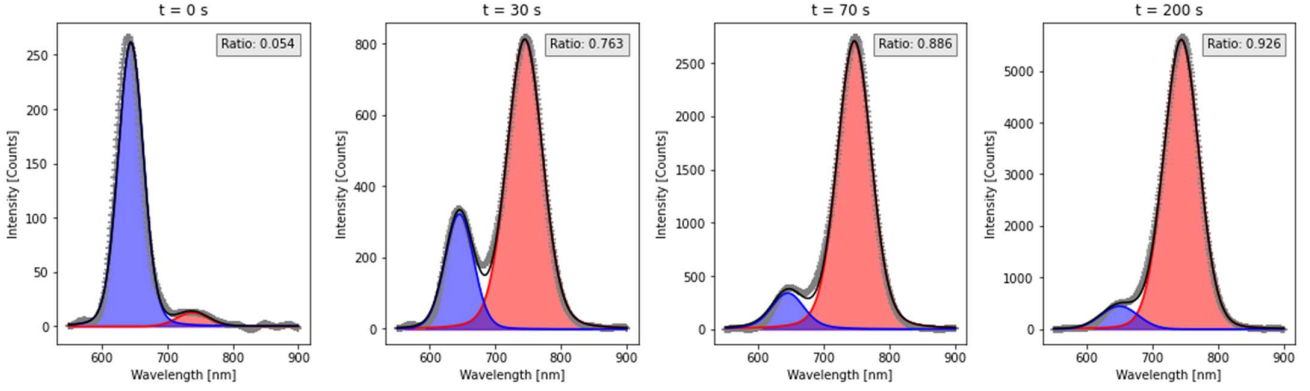
Br_65 Cs_5:



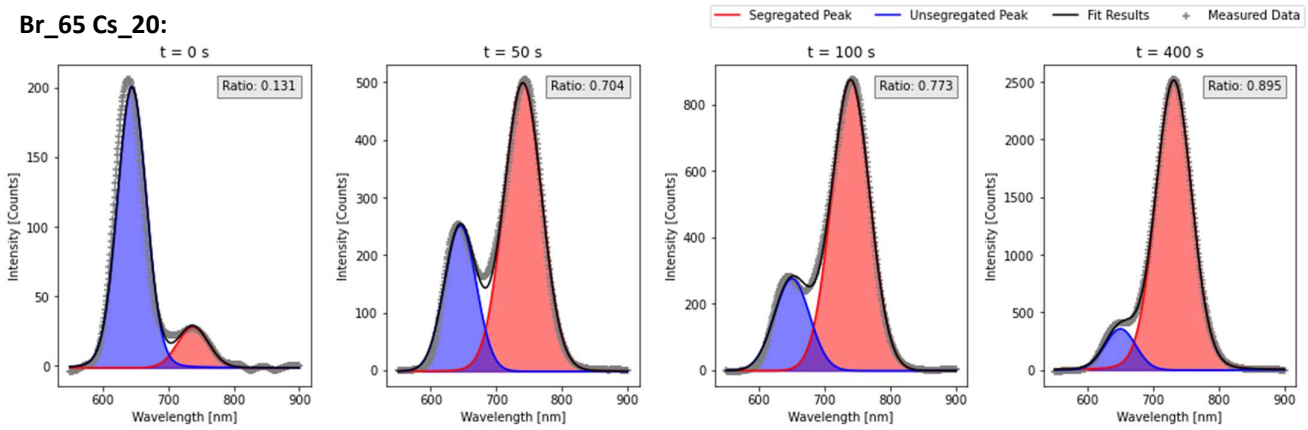
Br_65 Cs_10:



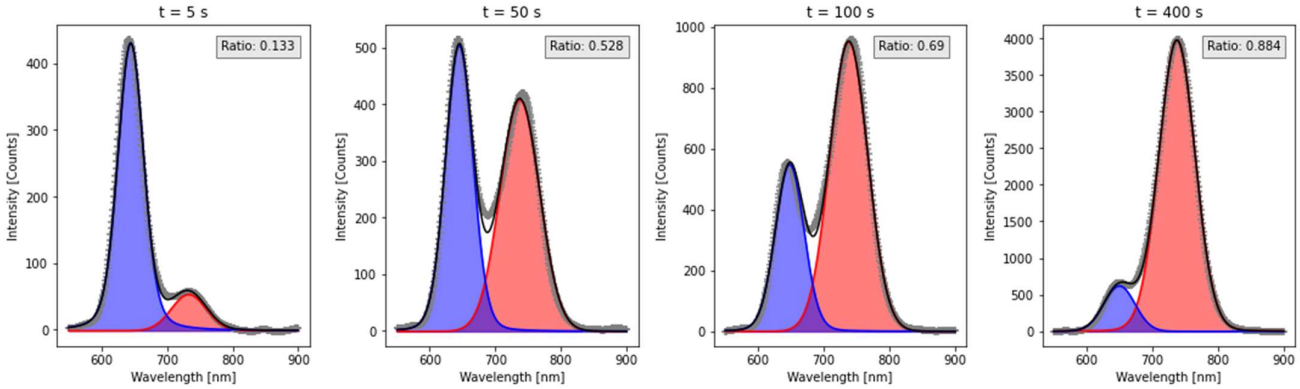
Br_65 Cs_15:



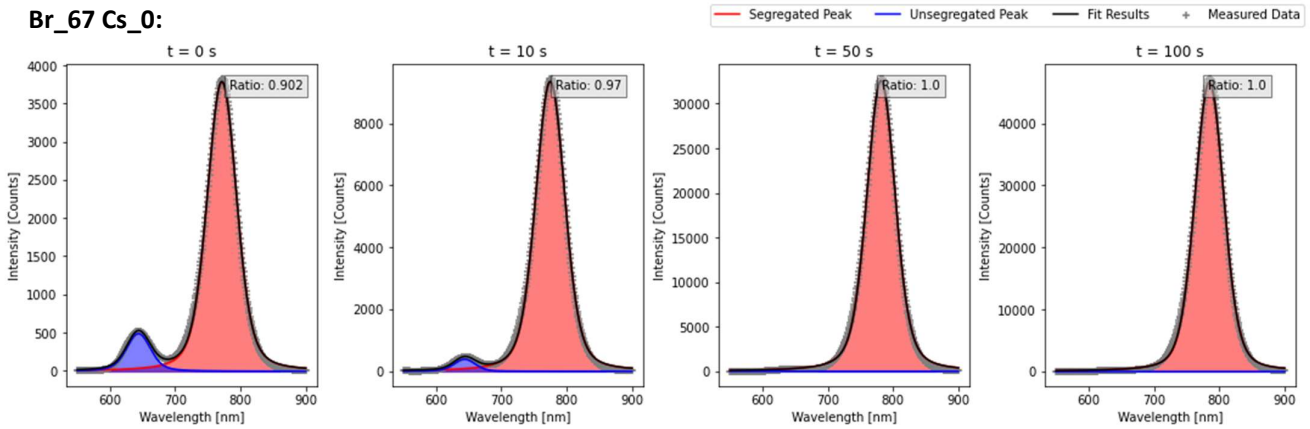
Br_65 Cs_20:



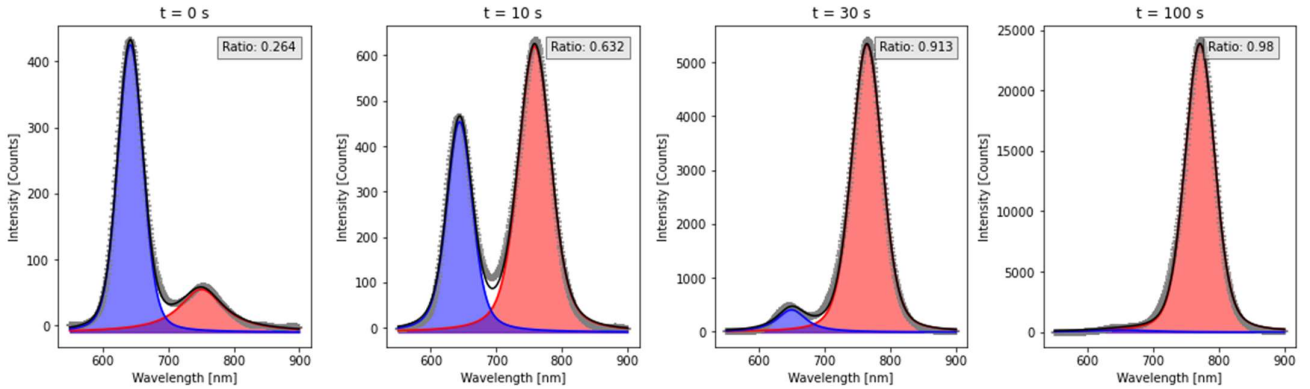
Br_65 Cs_25:



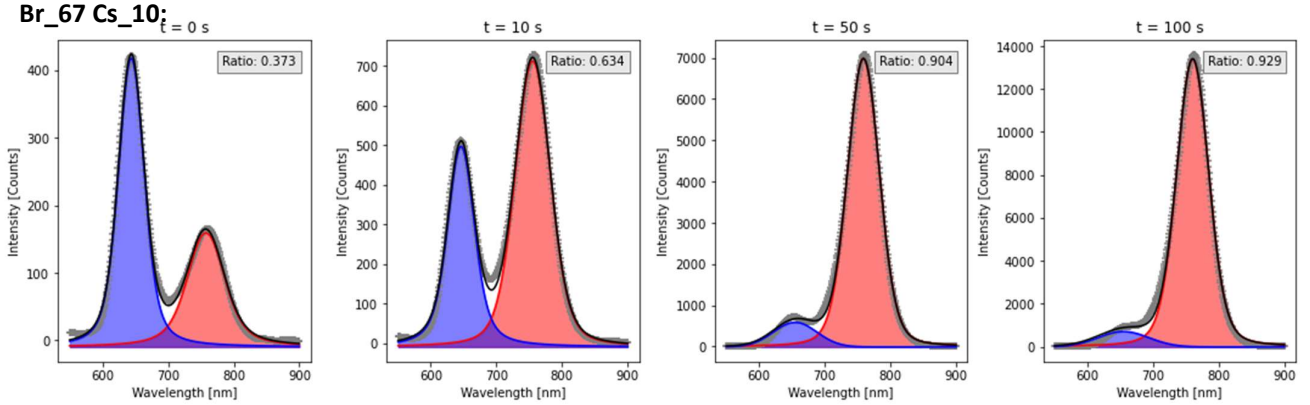
Br_67 Cs_0:



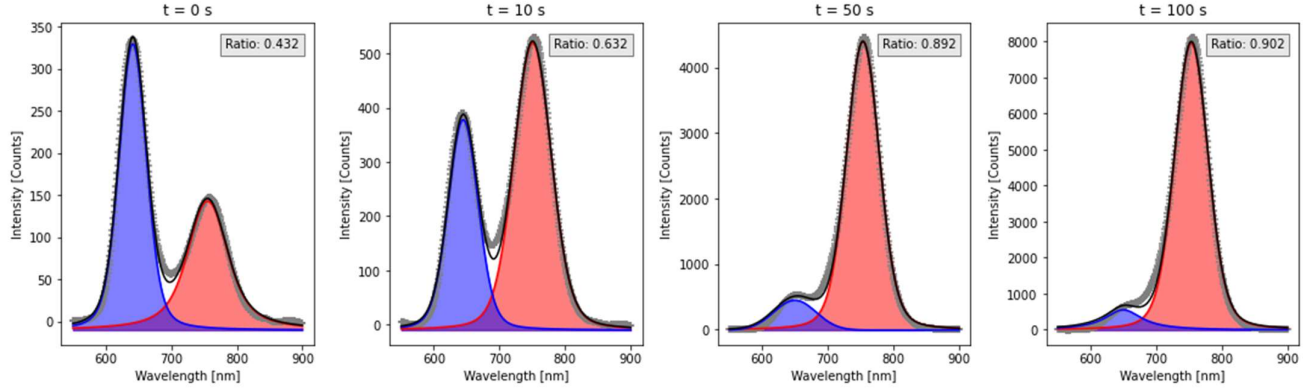
Br_67 Cs_5:



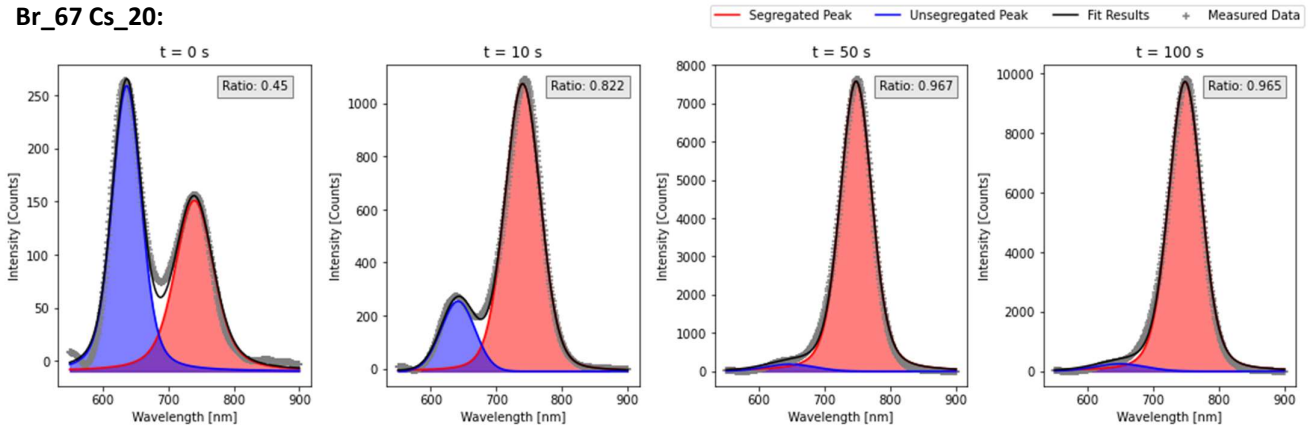
Br_67 Cs_10:



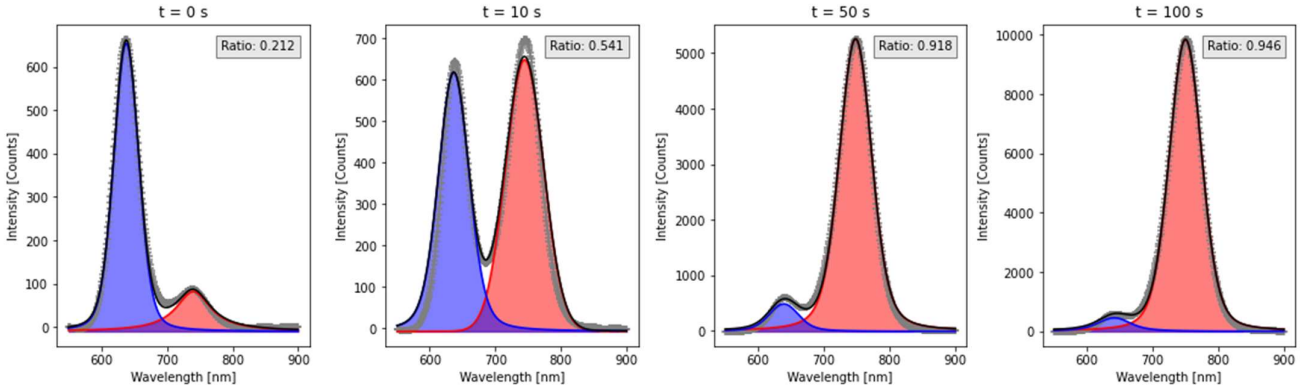
Br_67 Cs_15:



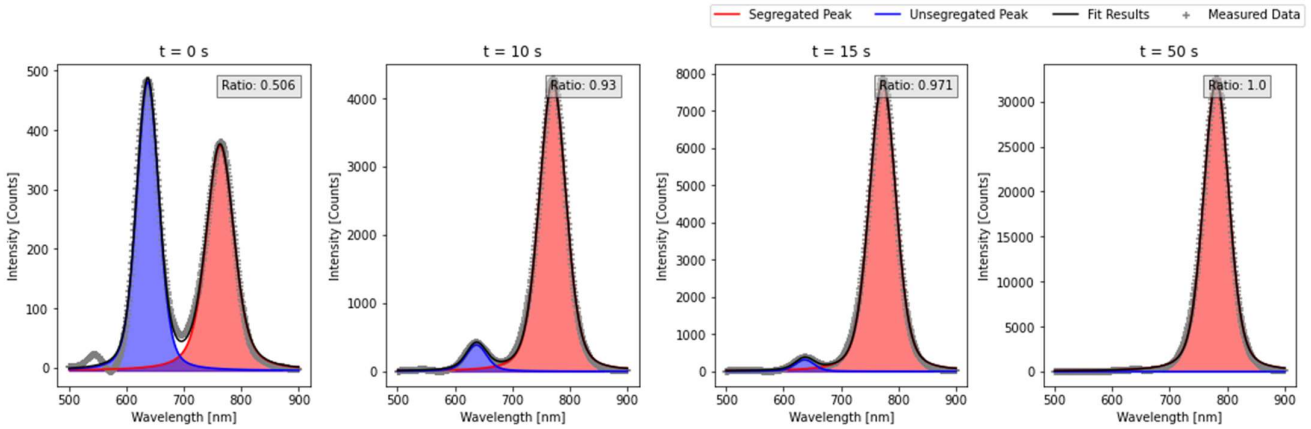
Br_67 Cs_20:



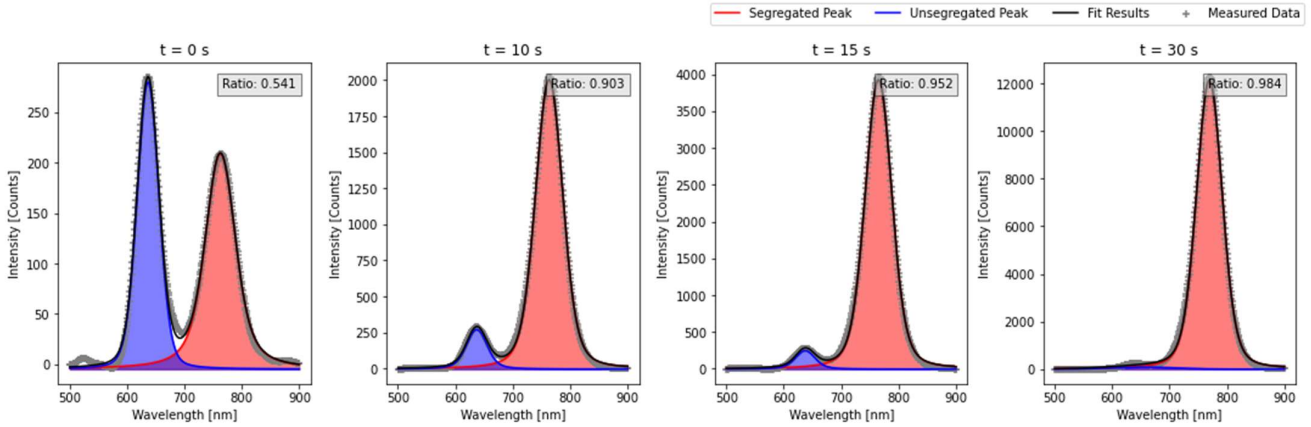
Br_67 Cs_25:



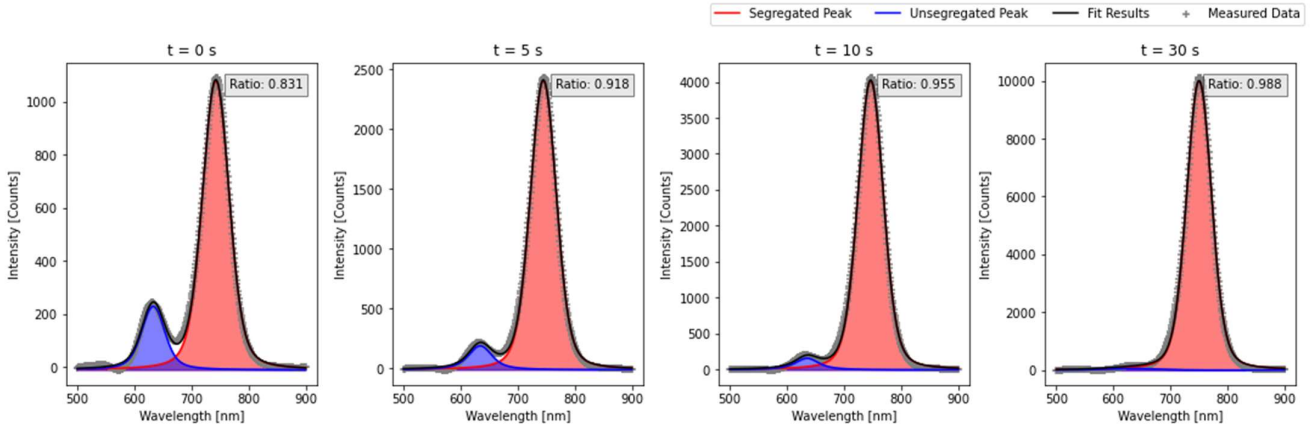
Br_70 Cs_0:



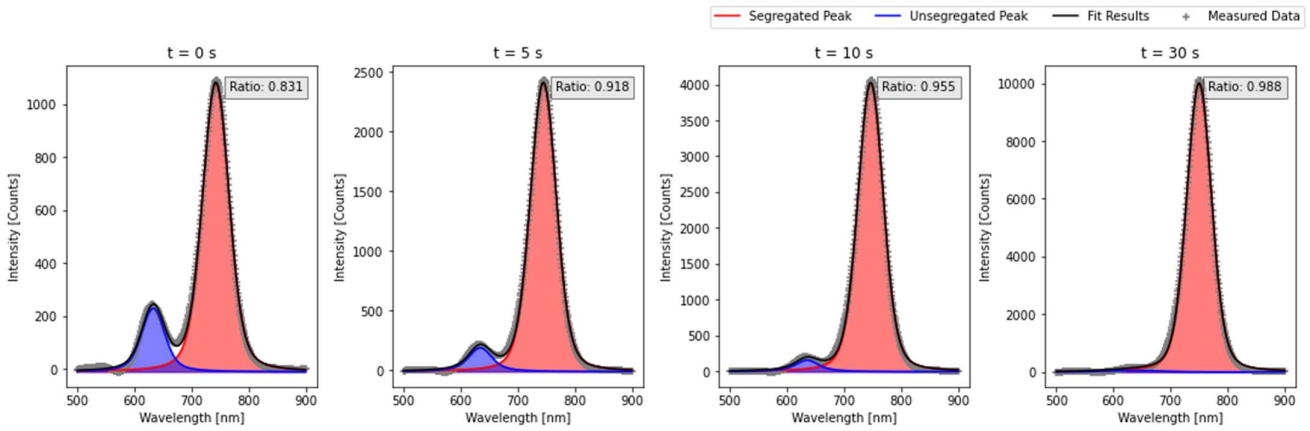
Br_70 Cs_5:



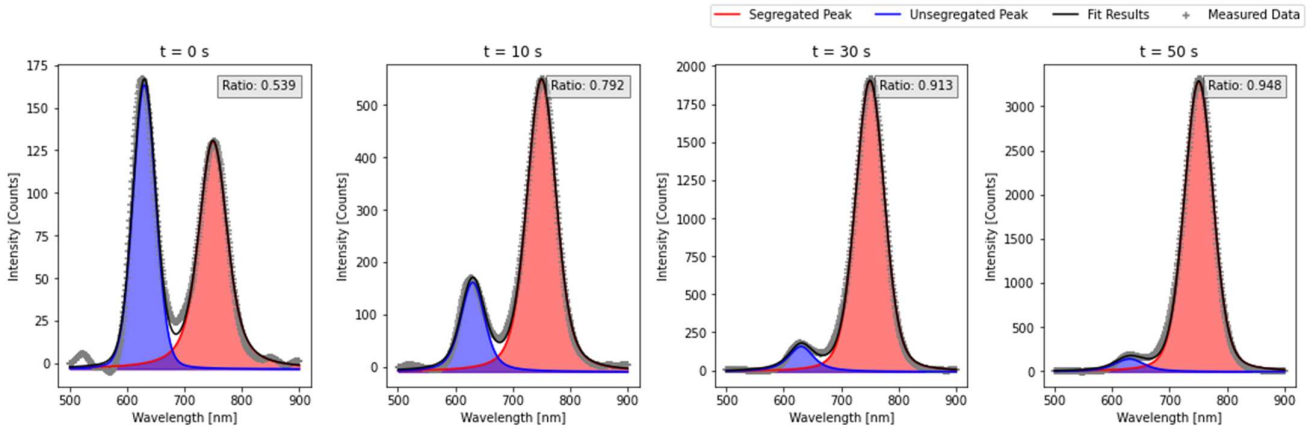
Br_70 Cs_10:



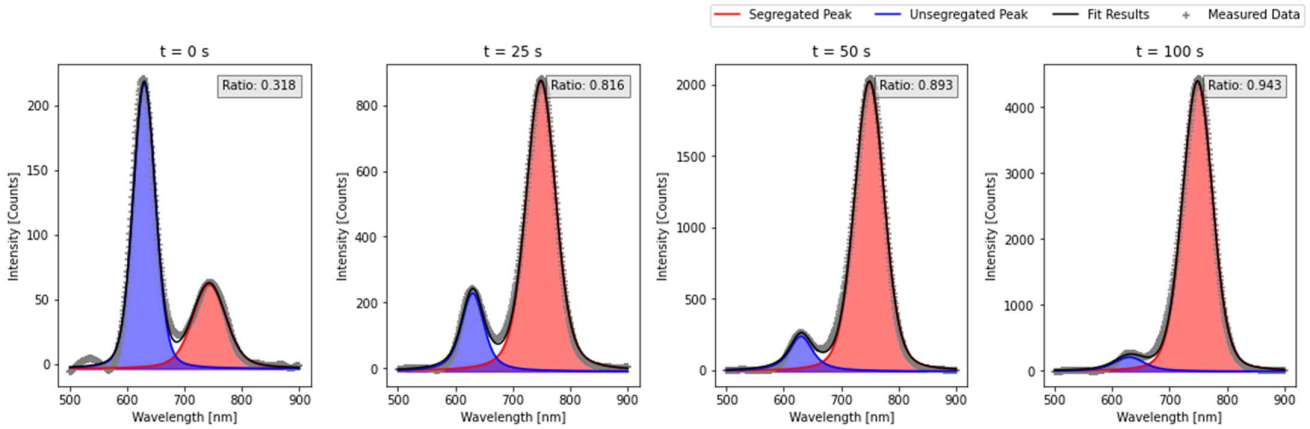
Br_70 Cs_15:



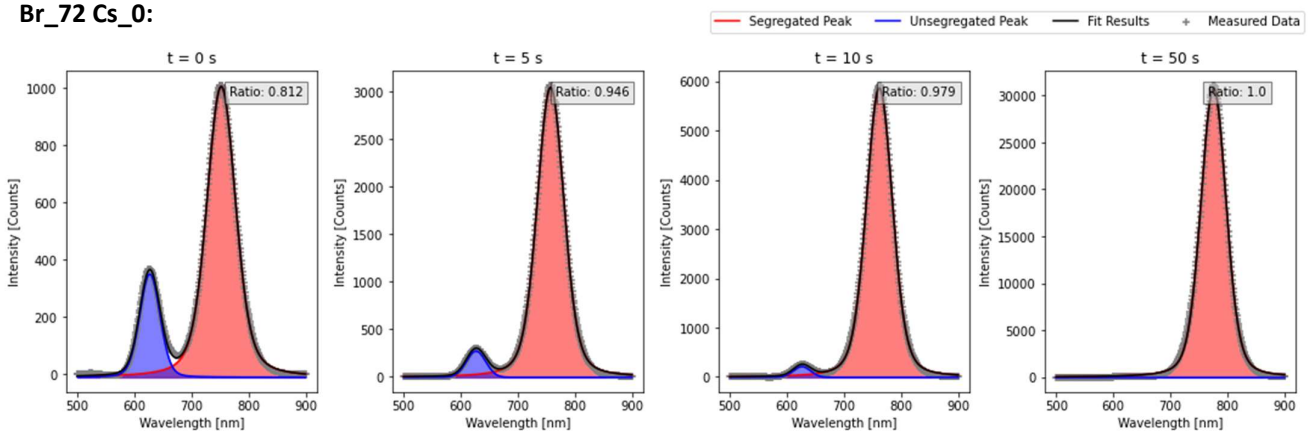
Br_70 Cs_20:



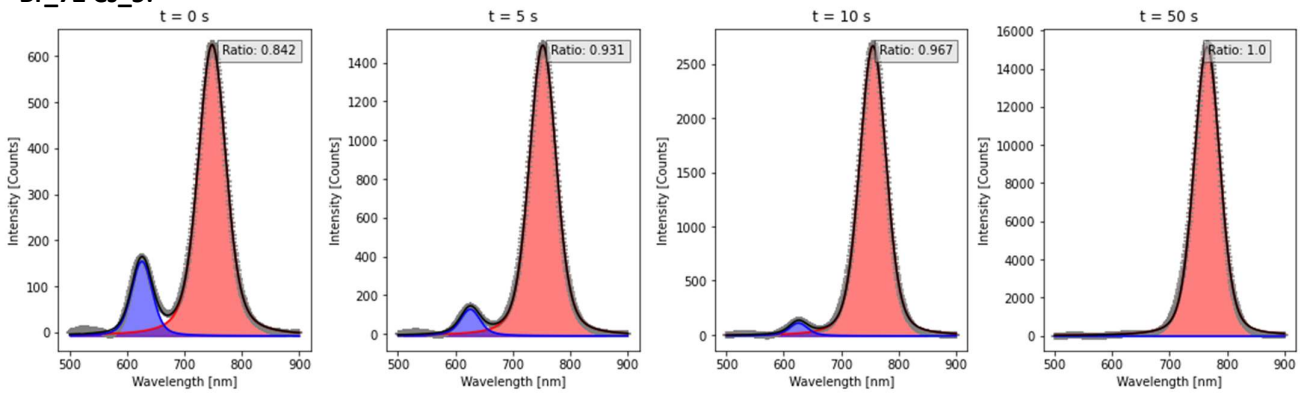
Br_70 Cs_25:



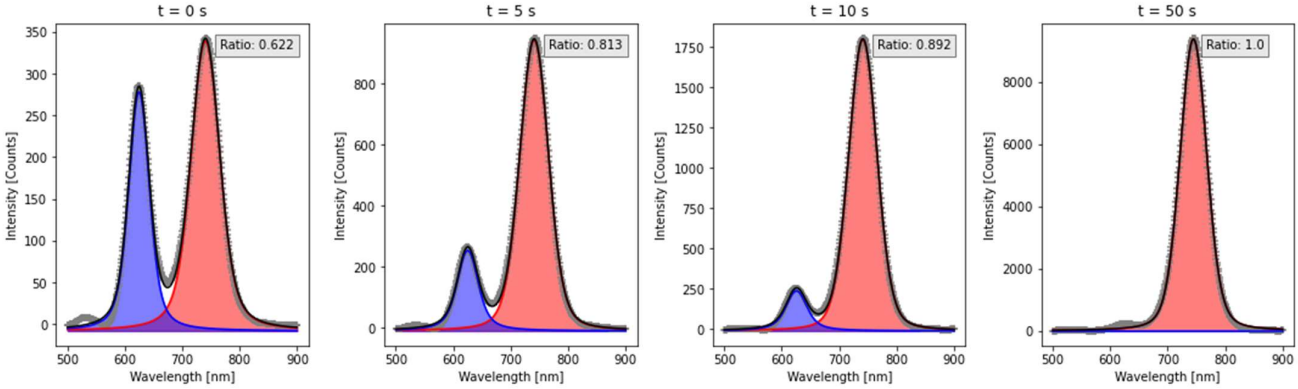
Br_72 Cs_0:



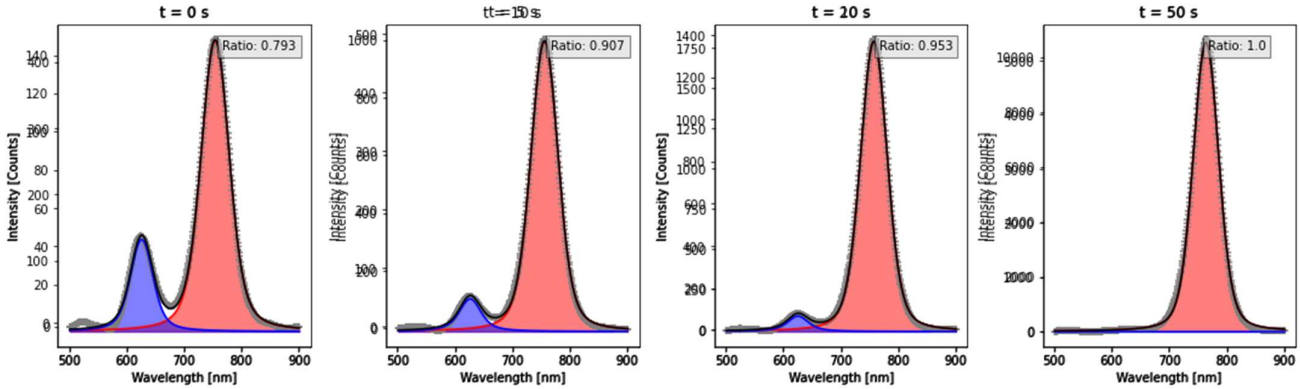
Br_72 Cs_5:



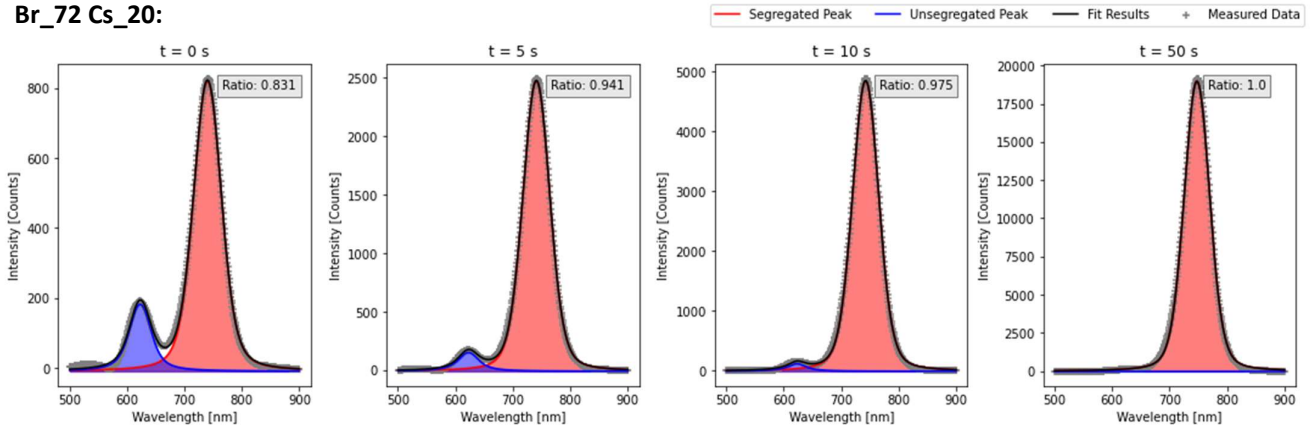
Br_72 Cs_10:



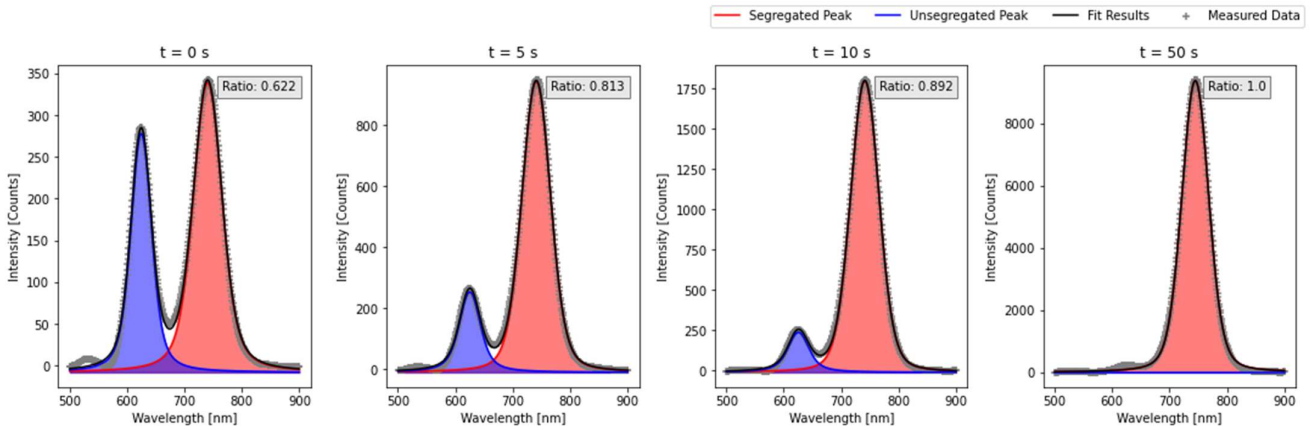
Br_72 Cs_15:



Br_72 Cs_20:



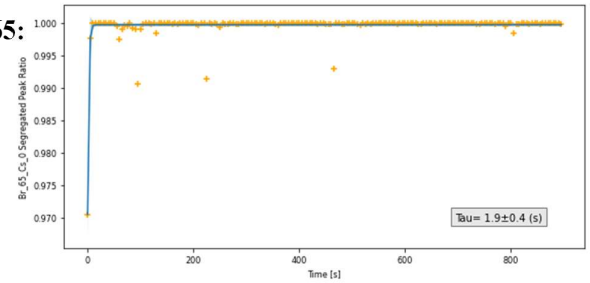
Br_72 Cs_25:

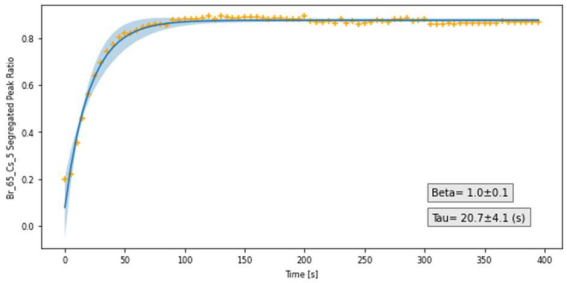


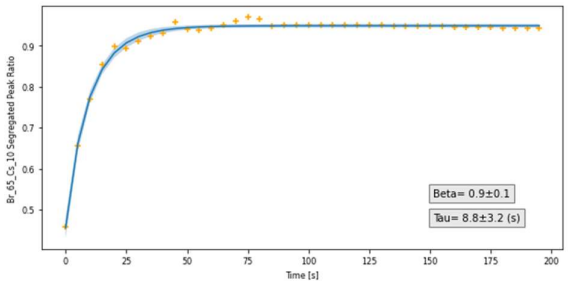
C.2(ii) Time evolution of peak area ratios:

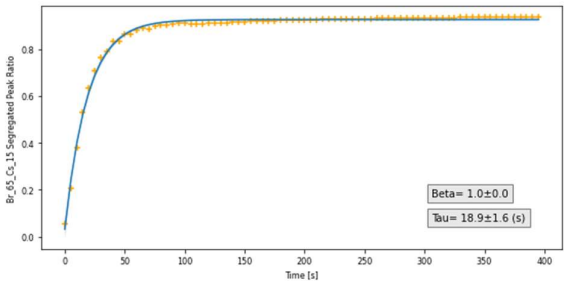
Data fitted to stretched exponential: $y = y_0 - e^{\left(t-t_0/\tau_0\right)^{-\beta}}$, time constant is $\tau = \frac{\tau_0}{\beta}\Gamma\left(\frac{1}{\beta}\right)$, except for Br_65 Cs_0 which was fitted to an exponential $y = y_0 - e^{\left(t-t_0/\tau_0\right)}$. Yellow markers are raw data, blue curve is fit, blue shaded area is 3-sigma uncertainty band.

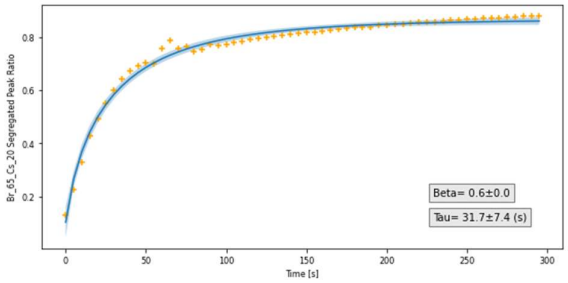
Br_65:

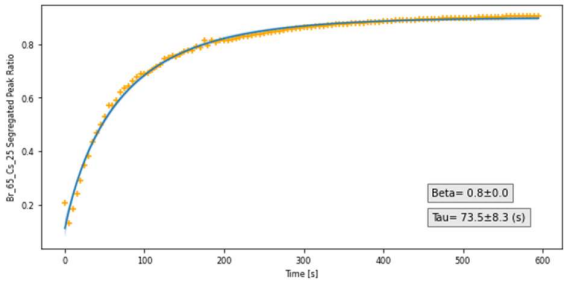




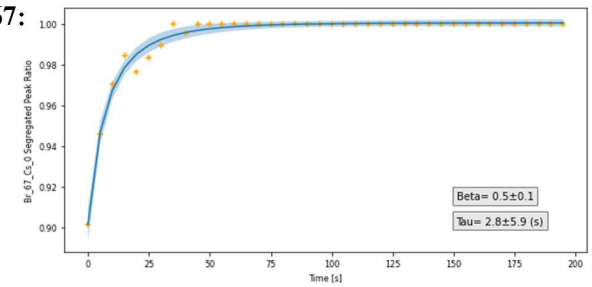


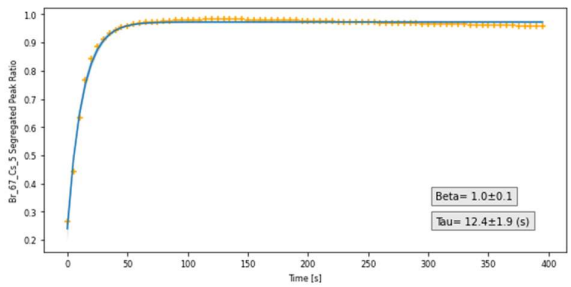


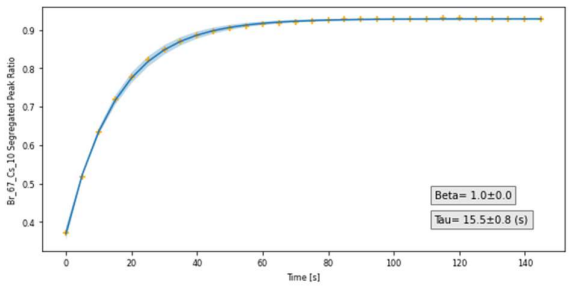


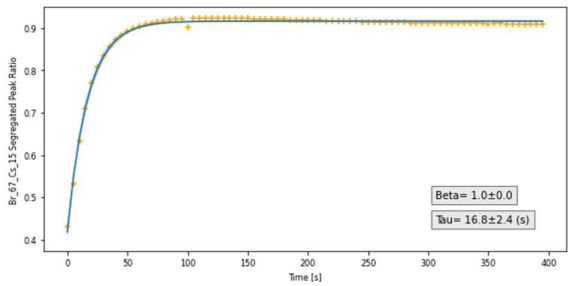


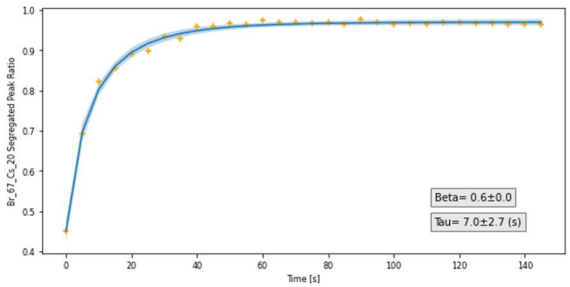
Br_67:

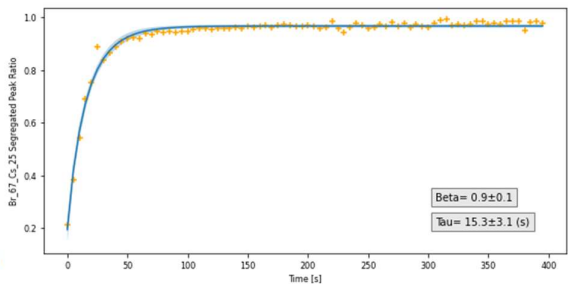




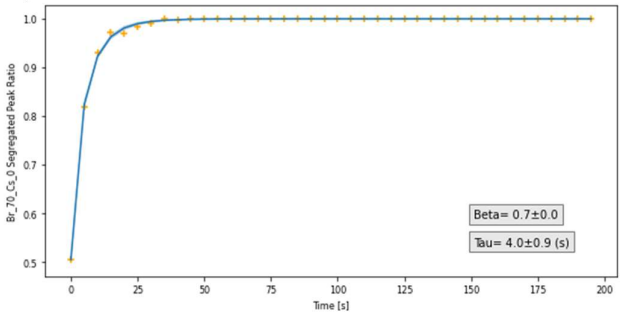


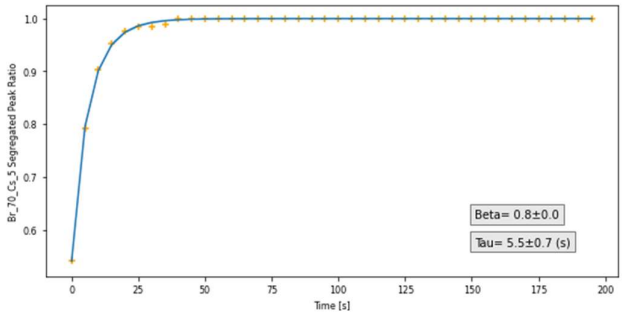


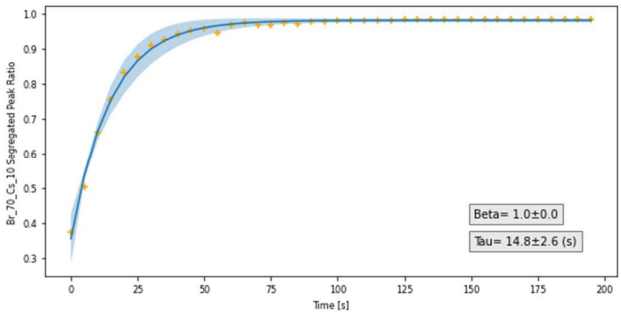


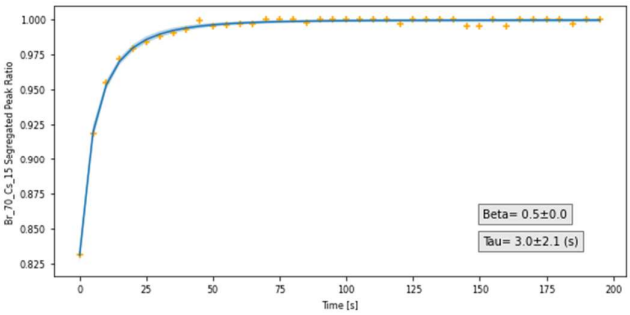


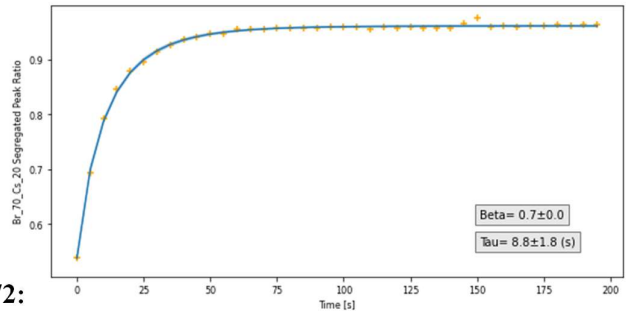
Br_70:

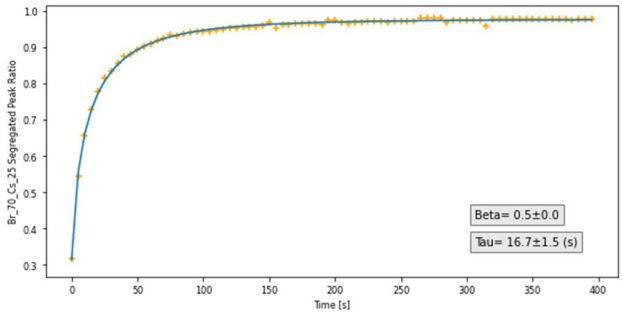

Br_70_Cs_0 Segregated Peak Ratio
Time [s]
Beta= 0.7±0.0
Tau= 4.0±0.9 (s)


Br_70_Cs_5 Segregated Peak Ratio
Time [s]
Beta= 0.8±0.0
Tau= 5.5±0.7 (s)

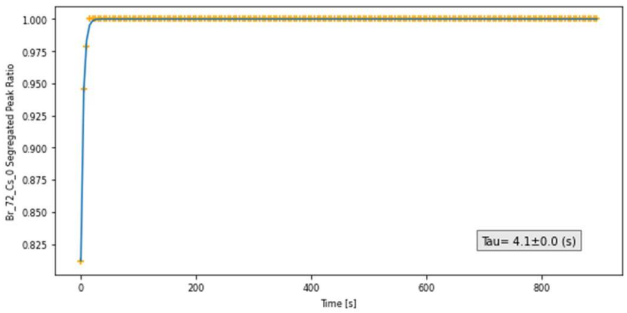

Br_70_Cs_10 Segregated Peak Ratio
Time [s]
Beta= 1.0±0.0
Tau= 14.8±2.6 (s)

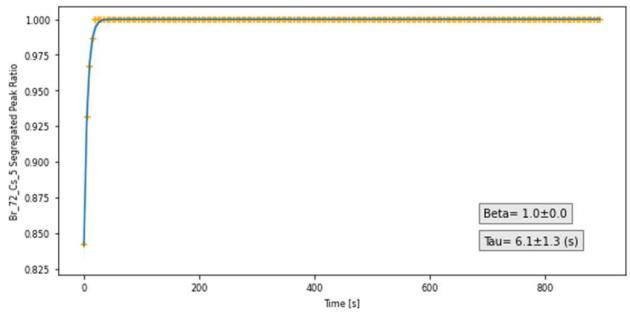

Br_70_Cs_15 Segregated Peak Ratio
Time [s]
Beta= 0.5±0.0
Tau= 3.0±2.1 (s)

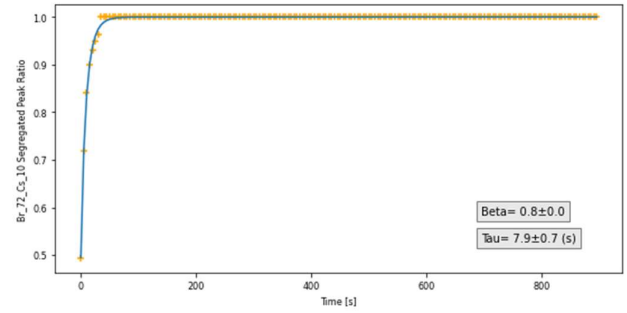

Br_70_Cs_20 Segregated Peak Ratio
Time [s]
Beta= 0.7±0.0
Tau= 8.8±1.8 (s)

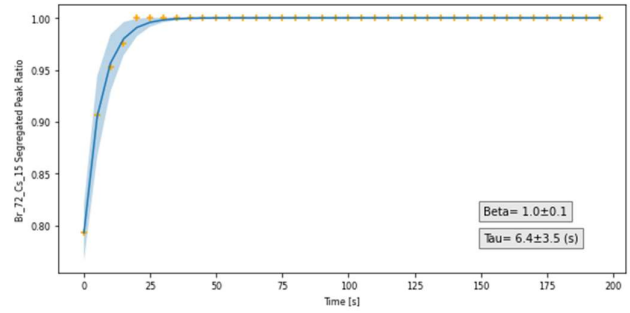

Br_70_Cs_25 Segregated Peak Ratio
Time [s]
Beta= 0.5±0.0
Tau= 16.7±1.5 (s)

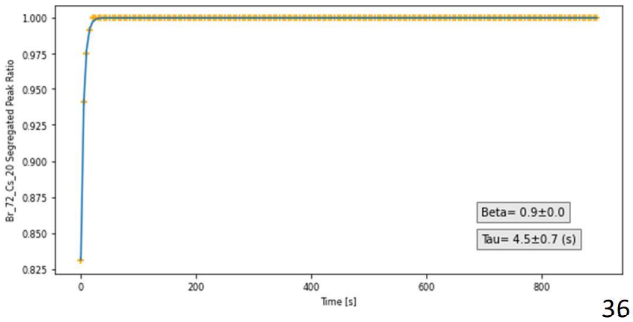
Br_72:

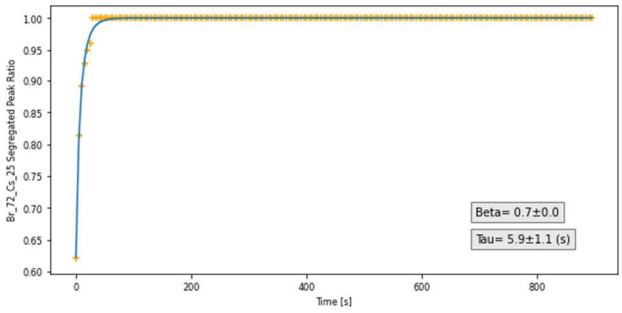

Br_72_Cs_0 Segregated Peak Ratio
Time [s]
Tau= 4.1±0.0 (s)


Br_72_Cs_5 Segregated Peak Ratio
Time [s]
Beta= 1.0±0.0
Tau= 6.1±1.3 (s)

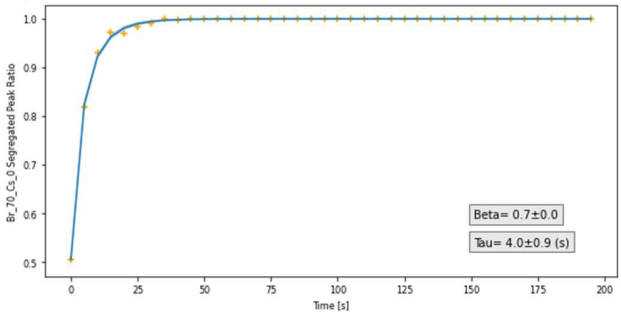

Br_72_Cs_10 Segregated Peak Ratio
Time [s]
Beta= 0.8±0.0
Tau= 7.9±0.7 (s)

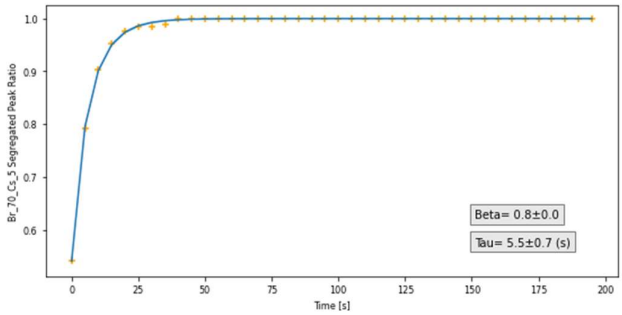

Br_72_Cs_15 Segregated Peak Ratio
Time [s]
Beta= 1.0±0.1
Tau= 6.4±3.5 (s)

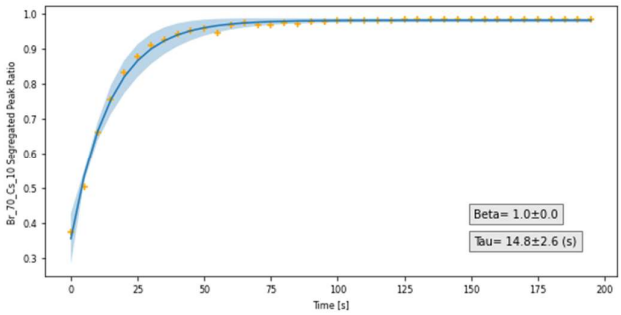

Br_72_Cs_20 Segregated Peak Ratio
Time [s]
Beta= 0.9±0.0
Tau= 4.5±0.7 (s)

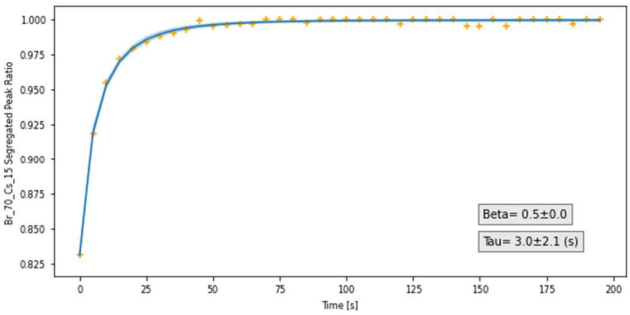

Br_72_Cs_25 Segregated Peak Ratio
Time [s]
Beta= 0.7±0.0
Tau= 5.9±1.1 (s)

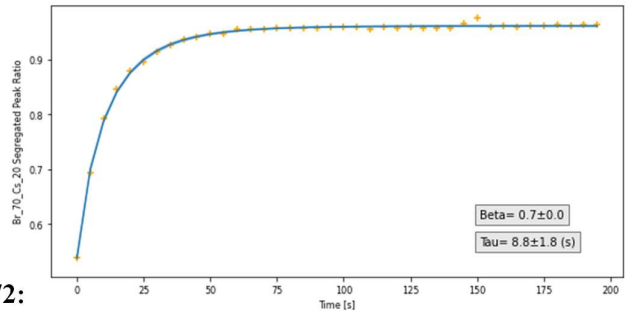
Br_70:

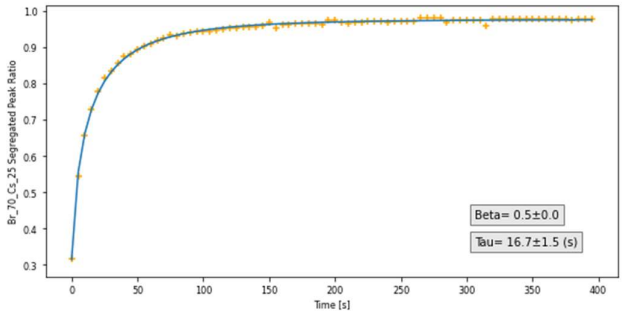

Br_70_Cs_0 Segregated Peak Ratio
Time [s]
Beta= 0.7±0.0
Tau= 4.0±0.9 (s)


Br_70_Cs_5 Segregated Peak Ratio
Time [s]
Beta= 0.8±0.0
Tau= 5.5±0.7 (s)

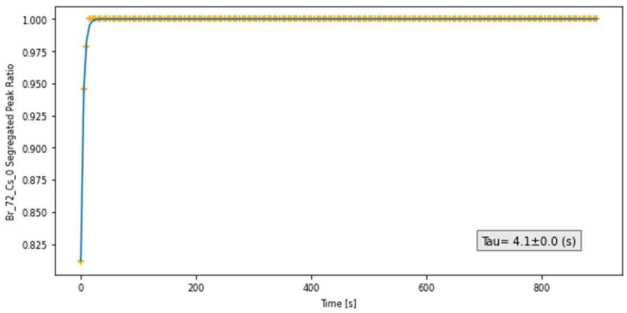

Br_70_Cs_10 Segregated Peak Ratio
Time [s]
Beta= 1.0±0.0
Tau= 14.8±2.6 (s)

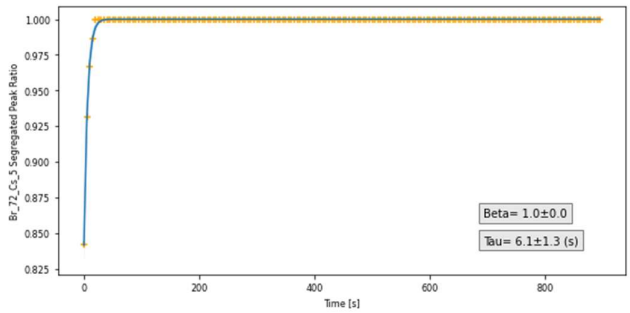

Br_70_Cs_15 Segregated Peak Ratio
Time [s]
Beta= 0.5±0.0
Tau= 3.0±2.1 (s)

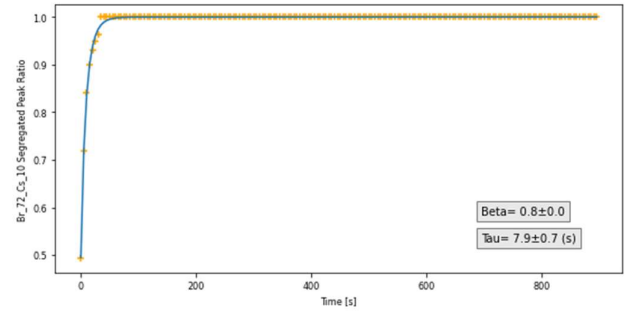

Br_70_Cs_20 Segregated Peak Ratio
Time [s]
Beta= 0.7±0.0
Tau= 8.8±1.8 (s)

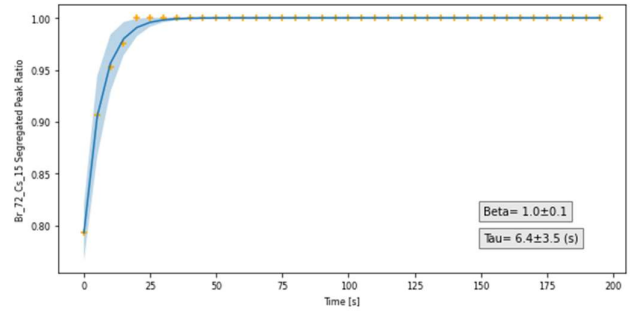

Br_70_Cs_25 Segregated Peak Ratio
Time [s]
Beta= 0.5±0.0
Tau= 16.7±1.5 (s)

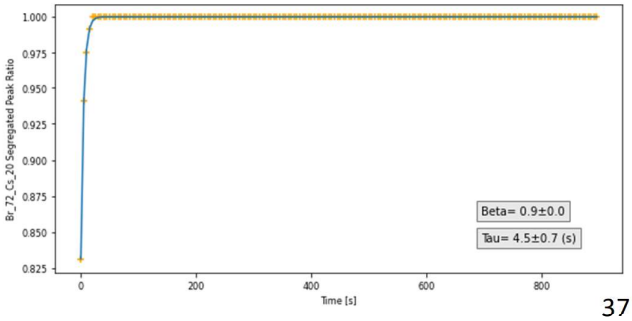
Br_72:

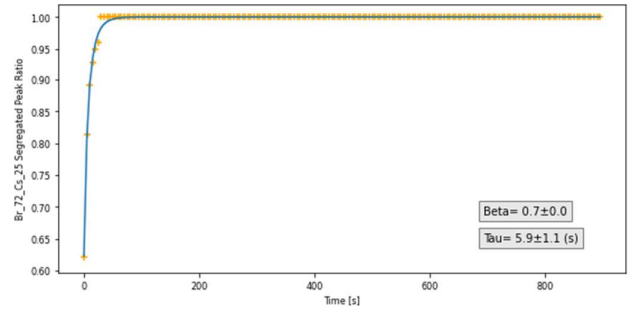

Br_72_Cs_0 Segregated Peak Ratio
Time [s]
Tau= 4.1±0.0 (s)


Br_72_Cs_5 Segregated Peak Ratio
Time [s]
Beta= 1.0±0.0
Tau= 6.1±1.3 (s)


Br_72_Cs_10 Segregated Peak Ratio
Time [s]
Beta= 0.8±0.0
Tau= 7.9±0.7 (s)

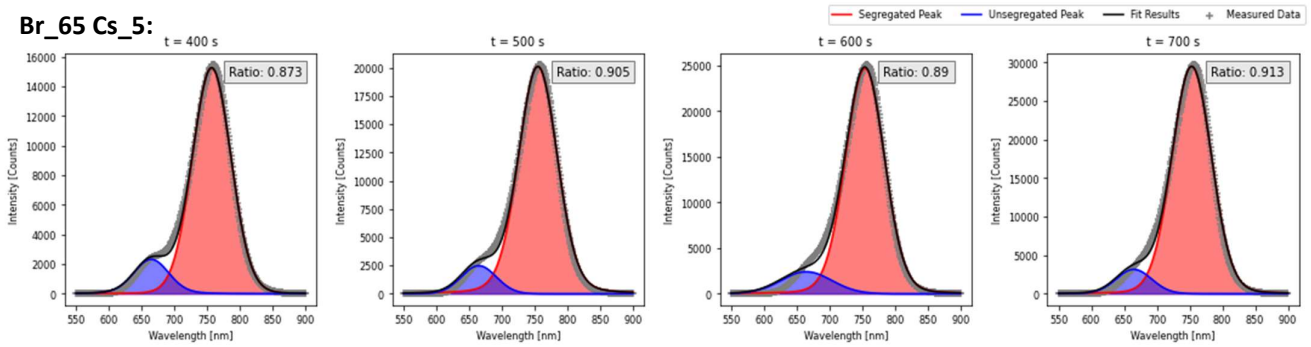

Br_72_Cs_15 Segregated Peak Ratio
Time [s]
Beta= 1.0±0.1
Tau= 6.4±3.5 (s)


Br_72_Cs_20 Segregated Peak Ratio
Time [s]
Beta= 0.9±0.0
Tau= 4.5±0.7 (s)

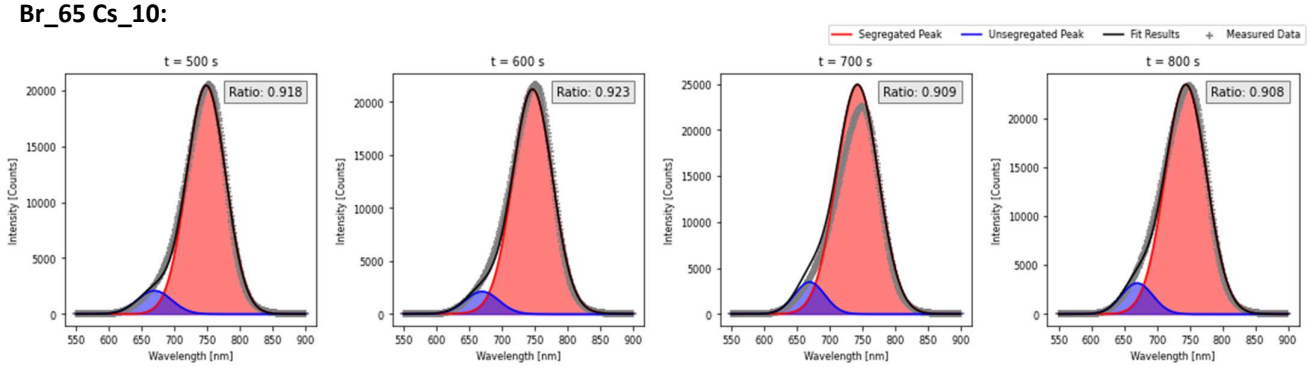

Br_72_Cs_25 Segregated Peak Ratio
Time [s]
Beta= 0.7±0.0
Tau= 5.9±1.1 (s)

C.2(iii) Results of fitting to sum of two Voigts at later times:

Br_65 Cs_5:



Br_65 Cs_10:

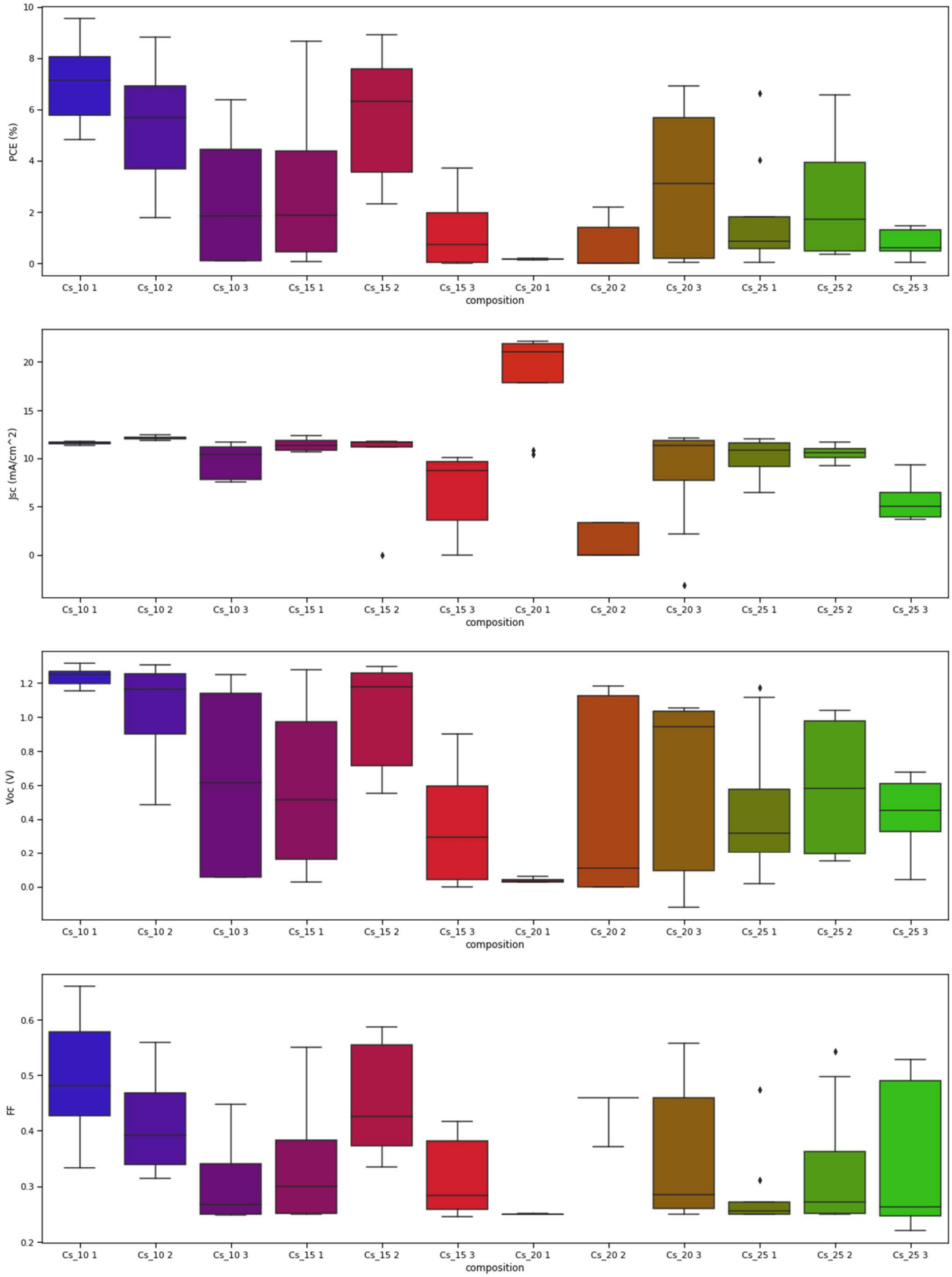


As can be seen in the above plots, the sum of two Voigts fitted poorly due to the asymmetry of the dominant peak, and erroneously attempted to ascribe another peak at ~660nm. For this reason, the stretched exponential was only fitted to the first ~300s of data.

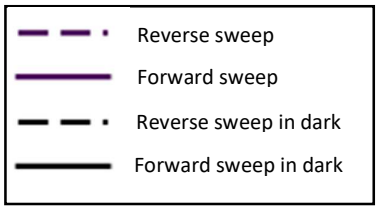
C.3 Device Performance

C.3(i) Steady-state characteristics:

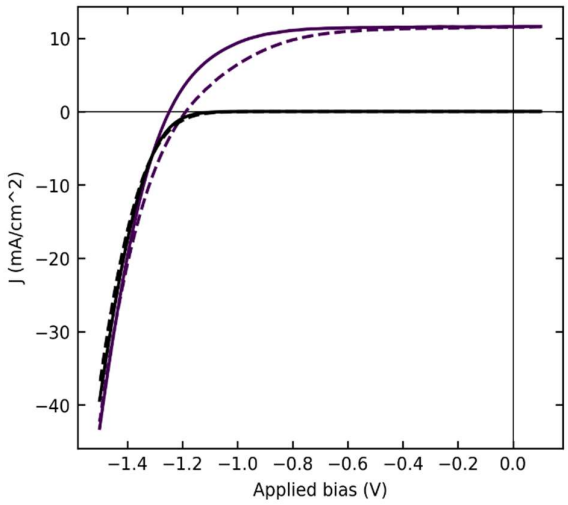
Naming convention: Cs_10_1 means device 1 of the fabricated 10% Cs compositions; three devices were fabricated for each composition. The readings with PCEs greater than 10% are anomalous and likely due to error in the placement of the devices in the solar simulator.



C.3(ii) J-V curves of best devices:

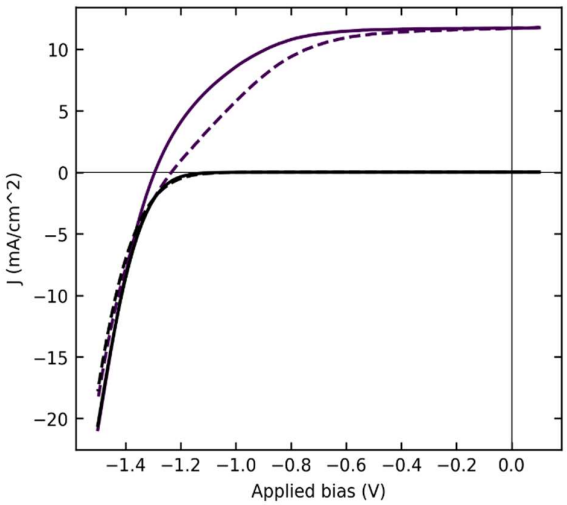


Br_65 Cs_10 device 1



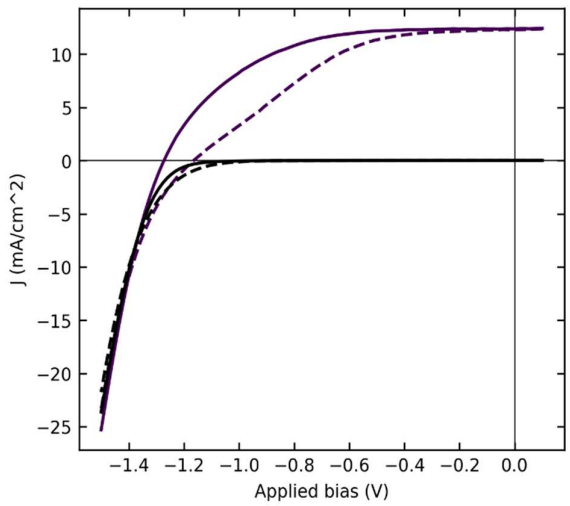
Power Conversion Efficiency (PCE):	9.53%
Open Circuit Voltage (V_{OC}):	1.25 V
Short Circuit Current Density (J_{sc}):	11.6 mA cm^{-2}
Fill Factor (FF):	0.66

Br_65 Cs_15 device 2



Power Conversion Efficiency (PCE):	8.91%
Open Circuit Voltage (V_{OC}):	1.29 V
Short Circuit Current Density (J_{sc}):	11.7 mA cm^{-2}
Fill Factor (FF):	0.59

Br_65 Cs_10 device 2



Power Conversion Efficiency (PCE):	8.81%
Open Circuit Voltage (V_{OC}):	1.27 V
Short Circuit Current Density (J_{sc}):	12.4 mA cm^{-2}
Fill Factor (FF):	0.56